Titre: Title:	On the 3D Vortex-Induced Dynamics of Soft Corals
Auteur: Author:	Alexandre Villié
Date:	2023
Type:	Mémoire ou thèse / Dissertation or Thesis
Référence: Citation:	Villié, A. (2023). On the 3D Vortex-Induced Dynamics of Soft Corals [Mémoire de maîtrise, Polytechnique Montréal]. PolyPublie. https://publications.polymtl.ca/54848/

URL de PolyPublie: PolyPublie URL:	https://publications.polymtl.ca/54848/
Directeurs de recherche: Advisors:	Frederick Gosselin, Stéphane Étienne, & Jérôme Vétel
Programme: Program:	Génie mécanique

POLYTECHNIQUE MONTRÉAL
affiliée à l'Université de Montréal

On the 3D Vortex-Induced Dynamics of Soft Corals

ALEXANDRE VILLIÉ
Département de génie mécanique

Mémoire présenté en vue de l'obtention du diplôme de *Maîtrise ès sciences appliquées*
Génie mécanique

Août 2023

POLYTECHNIQUE MONTRÉAL
affiliée à l'Université de Montréal

Ce mémoire intitulé :

On the 3D Vortex-Induced Dynamics of Soft Corals

présenté par **Alexandre VILLIÉ**
en vue de l'obtention du diplôme de *Maîtrise ès sciences appliquées*
a été dûment accepté par le jury d'examen constitué de :

Bianca VIGGIANO, présidente
Frédérick GOSSELIN, membre et directeur de recherche
Stéphane ETIENNE, membre et codirecteur de recherche
Vétel JÉRÔME, membre et codirecteur de recherche
Yahya MODARRES-SADEGHI, membre

ACKNOWLEDGEMENTS

I would like to express my gratitude to my supervisors for their support throughout the year and their guidance in this work. Prof. Jérome Vétel deserves a special thank you for his expertise on the experimental setup. I am deeply grateful to Prof. Stéphane Étienne for helping me to deepen my understanding of fluid-structure interaction through the prism of computational dynamics. His knowledge and guidance have been invaluable. I would also like to extend my appreciation to Prof. Frédérick Gosselin for selecting me as his Masters student. His insightful interpretations and critical thinking have greatly influenced my scientific mindset. He has been a true inspiration and has fueled my passion to pursue a career in research. I am thankful to Prof. Jorge Pérez Zerpa and PhD candidate Mauricio Vanzulli for their continuous assistance and availability during the course of this project. Their expertise in the ONSAS code has facilitated a quick implementation of the model. I am grateful for their warm welcome in Montevideo, Uruguay. The financial support provided by the Génie Par Simulation (GPS) program has been instrumental in the realization of this work. I am grateful for their support.

I would like to thank Tristan Leclercq for generously sharing his Matlab code, which has been essential in generating reference data. PhD candidate Mouad Boudina deserves a special mention for passing on his work and contributing to the foundation of this project. Acknowledgments also go to the members of LM2 for their collaboration and the fruitful discussions we had. Special thanks to Omar, Clement, and Raphael for their camaraderie and support. I would like to express my gratitude to the members of Polyfab for their valuable assistance with the SLS printing. Lastly, I wouldn't forget my lover for her emotional support and my roommates for providing a fun and uplifting environment throughout this journey.

RÉSUMÉ

Certains coraux mous, comme l'*Antillogorgia bipinnata*, présentent une géométrie ramifiée et sont suffisamment flexibles pour se plier sous l'effet des vagues. Ils se nourrissent passivement en interceptant les particules flottantes. Ces structures génèrent des tourbillons dans leur sillage, ce qui induit des vibrations rapides au niveau de leurs branches. Bien que les Vibrations-Induites par Vortex (VIV) pour des géométries droites aient fait l'objet d'études approfondies, la dynamique tridimensionnelle des structures ramifiées reste un domaine de recherche ouvert. Dans cette étude numérique et expérimentale, nous développons une nouvelle formulation pour l'estimation des VIV en ligne et transverses des structures arborées subissant de grandes déformations. Nous utilisons l'approche des éléments finis couplée à des oscillateurs sillage pour modéliser des géométries complexes de structures ramifiées. La résolution numérique est validée à travers cinq exemples, comprenant des comparaisons avec des solutions analytiques, un oscillateur de sillage et des données expérimentales provenant de la littérature. Nous menons également une étude expérimentale sur des structures ramifiées flexibles et élastiques fixées à l'intérieur d'une veine hydraulique et soumises à un écoulement constant et uniforme. Les amplitudes et les fréquences des déplacements transverses à l'extrémité des structures sont comparées à celles du modèle éléments finis développé.

Le modèle est appliqué à différentes géométries comportant $1, 2, 4$ et 8 paires de branches symétriques. Nous constatons que l'ajout de branches introduit de nouveaux modes dans la dynamique structurelle, qui sont successivement excités par la fréquence du lâché tourbillonnaire. À mesure que le nombre de branches augmente, les écarts de fréquence entre les modes diminuent, impliquant des écarts moins importants dans la réponse fréquentielle qui s'approche de la fréquence du lâché tourbillonnaire, conformément à la loi de Strouhal. En ajoutant des branches, les fréquences des modes ajoutés se répartissent de manière inégale et se regroupent autour de certaines fréquences. Les modes de fréquences proches sont excités simultanément ce qui entraîne des amplitudes de vibration plus faibles en raison du chevauchement des plages d'accrochage, tandis que les régions où la densité des modes est plus faible présentent une résonance plus forte et des amplitudes plus élevées pour des modes de fréquences isolées. Enfin, nous avons trouvé que la meilleure géométrie pour l'amélioration de l'interception des particules par les VIV est celle ayant deux paires de branches. Ainsi, un corail avec deux paires de branches peut intercepter jusqu'à 39% de particules en plus en vibrant par rapport à un corail fixe. L'augmentation du nombre de branches diminue ce gain d'interception.

ABSTRACT

Soft corals like the *Bipinnate* sea plume, have a branched geometry and are soft enough to bend under the waves. They feed passively by intercepting floating particles in the flow. Due to their circular cross section, a vortex street forms in the coral's wake inducing vibrations of its branches. Despite extensive studies on Vortex-Induced Vibrations (VIV) in straight geometries, the three-dimensional (3D) dynamics of flexible branched structures remains uninvestigated. In this numerical and experimental study, we develop a novel formulation for the accurate computation of in-line and cross-flow VIV of frame structures undergoing large deformation. The finite element method coupled with wake oscillators is used to model arbitrarily complex geometries of branched frame structures subjected to VIV. Our formulation allows us to model complex geometries with forks or sharp angles. Furthermore, we implement the numerical resolution procedure in the open-source library ONSAS. The numerical resolution procedure is validated by solving five examples, including comparisons with an analytical solution, a wake-oscillator, and experimental data from the literature. We also conduct experiments of flexible and elastic branched structures clamped inside a water tunnel under a constant uniform flow. The amplitudes and power spectral density of the tip transverse displacements are compared with the model prediction. Finally, the proposed formulation is applied on structures with $1, 2, 4$ and 8 pairs of symmetric branches.

We find that adding branches introduces new modes into the structural response, which are successively excited by the vortex shedding frequency. As the number of branches increases, the frequency gaps between modes decrease, resulting in smaller jumps in the frequency response which approaches the vortex shedding frequency, in accordance with the Strouhal law. As branches are added, the frequencies of the added modes become unevenly distributed and form mode clusters. Modes closer in frequency result in lower vibration amplitudes due to overlapping lock-in regions, while regions with a sparser mode density exhibit stronger resonance and higher amplitudes for isolated modes. Finally, we find that the best geometry for VIV enhancement of particle interception is two pairs of branches. A vibrating coral with two pairs of branches can then intercept up to 39% more particles than a fixed one. Increasing the number of branches would decrease this interception gain.

TABLE OF CONTENTS

LIST OF TABLES

LIST OF FIGURES

LIST OF SYMBOLS AND ACRONYMS

Acronyms

CFD	Computational Fluid Dynamics
DNS	Direct Numerical Simulation
FEM	Finite Element Method
FFT	Fast Fourier Transform
PSD	Power Spectral Density
PVW	Principle of Virtual Work
RMS	Root Mean Square
SLS	Selective Laser Sintering
TPE	Thermoplastic Elastomer
VIV	Vortex-Induced Vibrations
WOM	Wake-Oscillator Model

Symbols

D	The diameter
E	The Young modulus of the coral material
f_i	The ith mode frequency
f_w	The vortex shedding frequency
I	The second moment of inertia
J	The moment of inertia
ℓ	The height
ℓ_0	The element length
ℓ_b	The branches length
m_a	The fluid added mass
m_s	The mass of the structure
r_s	The solid damping coefficient
s	The curvilinear coordinate

t	The time
$\mathbf{u}$	The structure displacements vector
$\mathbf{U}$	The flow velocity vector
$\mathbf{U}_{\mathrm{pr}}$	The relative velocity vector projected on the cross section plane
$\mathbf{U}_{\mathrm{rel}}$	The relative velocity
V_s	The volume of the structure
$\mathbf{w}$	The structure rotations vector
δ_l	The logarithmic decrement
λ	The decay rate
Φ_i	The i^{th} mode shape
ρ_f	The fluid density
ρ_s	The structure density
Θ	The pretension
ζ	The damping ratio
Ω_f	The vortex shedding angular frequency
C_Y	The Cauchy number
Γ	The slenderness ratio
$\mathcal{M}$	The mass number
N	The number of pair of branches
$\mathcal{R}$	The reconfiguration number
R_{e}	The Reynolds number
S_t	The Strouhal number
U_r	The reduced velocity
p	The fluctuating in-line wake variable
q	The fluctuating cross-flow wake variable
A_p	The in-line coupling coefficient
A_q	The cross-flow coupling coefficient
ϵ_p	The in-line fluid damping coefficient
ϵ_q	The cross-flow fluid damping coefficient
C_D^0	The constant drag coefficient

C^0_{Di}	The fluctuating drag coefficient
C^0_L	The fluctuating lift coefficient
C_a	The added mass coefficient
$\delta\mathbf{d}$	The virtual displacement
$(\mathbf{e}_{\mathrm{x}}, \mathbf{e}_{\mathrm{y}}, \mathbf{e}_{\mathrm{z}})$	The global frame
$(\mathbf{r}_1, \mathbf{r}_2, \mathbf{r}_3)$	The rigid frame
$(\mathbf{t}_1, \mathbf{t}_2, \mathbf{t}_3)$	The local frame
A	The cross section area
$\mathbf{B}$	The transformation matrix
$\mathbf{I}$	The geometric inertia tensor
K	The kinematic energy
$\mathbf{L}_2$	The projection operator
$\mathbf{L}_3$	The rotation operator
Π_{23}	The cross section plane
$\mathbf{R}_r$	The rigid rotation matrix
β	The angle of the branches
ϕ	The element angle with the flow
$\mathbf{f}_{\mathrm{d}}$	The drag load
$\mathbf{f}_{\mathrm{l}}$	The lift load
$\mathbf{f}_{\mathrm{am}}$	The added mass load
$\mathbf{f}_{\mathrm{ine}}$	The inertial load
N_e	The number of elements
$\mathbf{r}_u$	The residual on the PVW
r^e_p	The in-line wake residual
r^e_q	The cross-flow wake residual
δ	The gain in interception rate of a cross section
Δ_s	The gain in interception rate of a structure
$\delta_{U_{pr}}$	The gain in relative velocity

LIST OF APPENDICES

CHAPTER 1 INTRODUCTION

Motivations

Corals captivate scientific interest due to their role as the "rainforests of the seas" (Knowlton et al., 2010). Reefs are renowned for their immense biodiversity. These extraordinary ecosystems harbor a staggering variety of marine species, approximately 25% of all marine organisms inhabit coral reefs (Bourne & Webster, 2013). Fig. 1.1 highlights the diversity of sea fans and sea plumes, members of the *Octocorallia* class, gathered in the same reef. However, climate change poses a significant threat to corals life: even a minor temperature fluctuation of 1°C in their habitat can trigger a phenomenon known as coral bleaching (Hoegh-Guldberg et al., 2007). This stress response causes corals to expel their symbiotic algae, which can lead to death if the stress persists. Moynihan et al. (2021) documented a relationship between high sea surface temperature, increased stiffness and density, changing the mechanical properties of *Porites* corals. The vulnerability of corals to such environmental changes highlights the critical need for reefs preservation. Coral farming, through the cultivation of corals in laboratory aquariums, provides a promising avenue for reef restoration projects (Shafir, van Rijn, & Rinkevich, 2016). However, it requires a deep understanding of coral metabolism functions, such as feeding. Corals are sessile passive filter feeders: deprived of any motility control,

FIGURE 1.1 Octocorals colony offshore reefs of the Caribbean Sea. Sea fans and sea plumes Photo credit: Frédérick P. Gosselin, October 2022

they intercept floating nutritive particles dragged to them by the ambient flow. They lack any form of active movement and instead rely on the passive flow-induced motion. Gosselin (2019) first reported high frequencies vibrations of sea plume *Antillogorgia bipinnata* at ~ 7 Hz, which is much higher than the swell frequency. He suggested that this natural vibration may enhance particle interception and optimize their feeding mechanisms. Boudina et al. (2021) demonstrated that these vibrations are Vortex-Induced Vibrations (VIV) and their simulations on a cross section demonstrate indeed an increase in particle interception of up to 40 % more than a fixed one during lock-in, suggesting that vibrating is a feeding strategy and may be an evolutionary advantage for soft corals.

VIV is a well-known and extensively studied phenomenon in the field of Fluid-Structure Interactions (FSI) (Paidoussis, 1998 ; de Langre, 2001 ; Modarres-Sadeghi, 2022). It occurs when the vortex street formed in the wake of a cylinder interacts with the displacements of the structure, leading to a resonance phenomenon known as lock-in. Within this lock-in range, the amplitudes of the structure's vibrations are maximized.

The study of VIV is of significant importance in engineering due to the potential for these vibrations to cause damage through fatigue. Structures such as chimneys in the air or pipelines underwater, are particularly susceptible to the detrimental effects of VIV. As a result, considerable efforts have been devoted to developing vortex suppression designs and strategies to mitigate these vibrations.

Incorporating VIV into plant models is necessary to improve the accuracy and realism of biomechanical simulations. Numerous studies have highlighted the importance of accounting for flexibility when modeling the behavior of plants submitted to hydrodynamic forces (Lei & Nepf, 2019 ; Sukhodolov, Sukhodolova, & Aberle, 2022). Experimental studies (Chaplin, Bearman, Huera Huarte, & Pattenden, 2005 ; Trim, Braaten, Lie, & Tognarelli, 2005) and numerical simulations (Willden & Graham, 2004 ; Leclercq & de Langre, 2018) show that continuous flexible structures encounter multiple lock-in regions due to the multiplicity of their natural frequencies. The intricate interplay between nonlinear wake dynamics and multimodal response presents significant challenges for modeling VIV in flexible structures and requires special numerical tools.

Understanding soft corals feeding mechanisms is a compelling motivation for developing a novel VIV formulation applicable to branched structures. By delving into the complex interaction between a flexible branched structure and its turbulent wake, we aim to unravel the underlying mechanisms of the fascinating vibrations exhibited by the sea plume *Antillogorgia Bipinnata*.

This thesis aims to provide a formulation and its numerical resolution method for predicting the 3D vortex-induced dynamics of branched structures as well as its biological implication. Furthermore, the exploration of living systems out of sheer curiosity holds value in itself and has the potential to unveil a multitude of inventions. The development of bio-inspired systems is driven by the desire to harness nature's wisdom, improve performance, unlock unique capabilities. Nature has evolved over millions of years, resulting in highly efficient and optimized solutions. By incorporating these features into our designs, we can create systems with enhanced functionality. The study of soft corals vibrations might as well inspire innovative systems, all the more as VIV is a passive phenomenon that do not require any energy input except from a flow velocity.

This thesis is structured as follow: In chapter 2, we first delve into the available literature in order to define the key concepts involved and contextualize our research within existing models. Chapter 3 exposes the research obectives. Chapter 4 presents a finite element model able to assess VIV of branched frame structures in large deformation and large rotations. Afterwards, we verify our model in small displacements with an analytical solution, and validate it against numerical and experimental studies from literature in chapter 5. New experimental data are generated and compared to the model. In chapter 6, we extract from numerical results some biological insights about the influence of the 3D vortex-induced dynamics of branches on the feeding efficiency. Finally chapter 7 concludes on the objectives and discuss on the limitations of the work. Furthermore, it presents an outlook on potential avenues for future research.

CHAPTER 2 LITERATURE REVIEW

The literature review begins by examining the biological characteristics of corals. Subsequently, we explore the previous work modeling VIV and discuss how plants and animals cope with this instability. Lastly, we look at the existing formulations to model flexible beam structures experiencing large displacements.

Corals

Corals belong to the class *Anthozoa* and are classified within the phylum *Cnidaria*, encompasses other organisms such as jellyfish and sea anemones. Corals are composed of polyps, tiny organisms acting as a digestive and feeding system (Fabricius & Hopley, 2011). It captures food with a ring of tentacles and releases calcium carbonate, creating the coral skeleton (Boschma, 1925). Living in symbiosis, polyps form coral reefs, among the most prolific and diverse habitats on Earth.

Octocorallia, also known as *Alcyonaria*, is a class of *Anthozoa* comprising around 3 000 species of corals (Daly et al., 2007). It comprises soft corals that have flexible branches that sway with the ocean currents. As passive filter feeders, they rely on the water movement to bring them a constant supply of nutrients. They feed on phytoplankton or organic debris that are passively transported into the polyps' digestive system (Ribes, Coma, & Gili, 1998). The vital functions of corals, such as respiration, photosynthesis, heat exchange, and reproduction, are highly dependent on the surrounding flow. Studies on the branches-flow interaction provide valuable insights into these biological process. Malul, Holzman, et Shavit (2020) showed that an out-of-phase motion of coral branches relative to the swell enhances mass transfer at the tentacle tip by up to 25 % as compared with an in-phase motion. Gosselin (2019) first reported high frequencies vibrations of sea plume *Antillogorgia bipinnata* at $\sim$ 7 Hz, which is much higher than the swell frequency. Boudina et al. (2021) showed that these oscillations are produced by the von Kármán vortex street that forms in the wake of the branches. Their simulations of a vibrating cross section demonstrate an increase in particle capture of up to 40 % more than a fixed branch during lock-in, suggesting that vibrating is a feeding strategy and may be an evolutionary advantage for soft corals. Figure 2.1 shows two soft corals on which VIV have been observed in the offshore reefs of Puerto Morelos in the Caribbean Sea.

(a) Soft coral (possibly Eunicea Flexuosa) in Cozumel, Mexico. Black and white bands are 10 cm long

(b) Antillogorgia Americana in Puerto Morelos, Mexico

FIGURE 2.1 Soft corals in the offshore reefs of Puerto Morelos, Mexico in the Caribbean Sea. Photo credit : Frédérick P. Gosselin, October 2022

Vortex-Induced Vibrations

Vorticity quantifies the angular velocity within a fluid. It arises due to the adherence and shearing of fluid particles along a body surface, resulting in velocity gradients. At low Reynolds numbers (R_e) no vortex formation occurs. However, as the Reynolds number increases, a pair of counter-rotating vortices emerges, creating a recirculation zone at the rear of the body (Etienne & Pelletier, 2012). This region of swirling motion undergoes oscillations starting at $R_e \approx 20$ (Williamson, 1996), and beyond $R_e \approx 45$, periodic shedding of vortices takes place, forming the well-known von Kàrmàn vortex street (Blevins, 1990). Within the range of $R_e \in [45 - 150]$, the shedding of von Kàrmàn vortices exhibits a laminar pattern, as depicted in Figure 2.2. It transitions into a slightly turbulent regime above $R_e \approx 150$ (Blevins, 1990).

VIV are characterized by a coupling between this vortex street and the structure displacements. The shedding of vortices in an alternating manner results in oscillating drag and lift forces, inducing vibrations in the in-line and cross-flow directions (Sarpkaya, 1976 ; Khalak & Williamson, 1999). Vortices are shed periodically at a frequency

$$f_w = \frac{S_t U}{D} \tag{2.1}$$

with U the upstream flow velocity and D the cross section diameter. S_t is a constant called Strouhal number. When the frequency of vortex shedding f_w aligns with the natural frequency of a vibrating body, a phenomenon known as lock-in occurs, resulting in a net work done by the fluid flow on the body (Blevins, 1990 ; Païdoussis, Price, & de Langre, 2010). This lock-in phenomenon is a nonlinear resonant response, with a well-defined velocity range of synchronization where the cylinder exhibits the highest amplitude vibrations.

The lock-in effect leads to significant oscillatory motion with large amplitudes of order of one diameter, damaging slender structures with fatigue accumulation (Mukundan, Modarres-

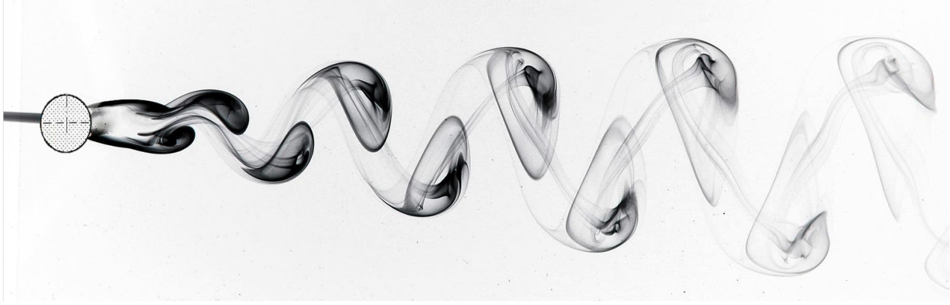

Figure 2.2 Visualisation of the von Kàrmàn vortex sheet in the wake of a circular cylinder, taken from Wagner (2014)

Sadeghi, Dahl, Hover, & Triantafyllou, 2009 ; J. Wang, Fu, Baarholm, Wu, & Larsen, 2015). Consequently, this flow instability presents an ongoing challenge for engineers (Blevins, 1977 ; Paidoussis, 1998 ; Evangelinos & Karniadakis, 1999a ; Naudascher, 2017). Mitigating VIV on slender structures, such as riser pipes, underwater cables, chimneys, and others, lies at the core of VIV research. Various methods, including the addition of helical strakes or ribbons (R. D. Blevins & Coughran, 2009 ; Gao, Fu, Ren, Xiong, & Song, 2015), are being explored to address this issue and enhance the structural integrity of these systems. VIV mitigation also allows for drag reduction (Law & Jaiman, 2017 ; Chizfahm & Jaiman, 2021). More recently, VIV raises interest as a potential source of clean energy (Bernitsas, Raghavan, Ben-Simon, & Garcia, 2008 ; Xia, Michelin, & Doaré, 2015 ; Francis, Umesh, & Shivakumar, 2021).

Marine life has developed mechanisms through evolution to cope with VIV. These adaptations are observed across various organisms and serve different purposes. For example, some plants benefit from flow-induced vibrations, which enhance the dispersion rate of underwater plant canopies (Sehat, Abdolahpour, Jamali, & Ghisalberti, 2023) or facilitate pollination (McCombe & Ackerman, 2018). Some animals have developed their own structural design to mitigate flow-induced vibrations, like seal's whiskers to better chase preys in the dark (Hanke et al., 2010 ; Beem & Triantafyllou, 2015 ; Lyons, Murphy, & Franck, 2020), or helical strake-like ridges on glass sponges (Fernandes et al., 2021). On the other hand, some animals use VIV to increase pheromone capture for moth males (Spencer et al., 2019) or heat exchange for coral tentacles (Malul et al., 2020). In the context of soft corals, Gosselin (2019) first reported VIV on the flexible branches of *Antillogorgia bipinnata.* Two-dimensional (2D) simulations of a vibrating cross section conducted in Boudina et al. (2021) demonstrate an increase in particle capture of up to 40 % more than a fixed branch during lock-in, suggesting that sea plumes may use VIV as a feeding strategy.

One approach to study VIV numerically is to solve a fully coupled system with the Navier-Stokes equations for the fluid and the elastodynamics equations for the structure. Numerous numerical methods in Computational Fluid Dynamics (CFD) have been used to predict VIV, such as quasi-three-dimensional methods (Willden & Graham, 2001), coupled 3D finite element methods (FEM) (Holmes, Oakley Jr, & Constantinides, 2006) or finite volume methods (Menter, Sharkey, Yakubov, & Kuntz, 2006). However, simulating all of the surrounding fluid flow is extremely computationally demanding due in part to the range of length and time scales and to large amplitudes of motion.

Wake-oscillator model

One alternative method is to empirically model the forcing of the wake on the structure. Bishop et Hassan (1964) first proposed the wake-oscillator model (WOM) to simulate the hydrodynamic forcing of the wake on a rigid cylinder. This phenomenological model of VIV allows us to explore the fundamental physics of this instability at low computational costs. It uses the drag and lift forces per unit length acting on a circular cross section :

$$\mathbf{f}_{\text{drag}} = \frac{1}{2} C_D \rho_{\text{f}} D U^2 \mathbf{t}_d, \tag{2.2}$$

$$\mathbf{f}_{\text{lift}} = \frac{1}{2} C_L \rho_{\text{f}} D U^2 \mathbf{t}_l, \tag{2.3}$$

with C_D, C_L the drag and lift coefficients, ρ_{f} the fluid density and $\mathbf{t}_d, \mathbf{t}_l$ the drag and lift directions, respectively. The WOM produces oscillating cross-flow displacements by coupling C_L to a scalar wake variable q :

$$C_L = \frac{1}{2} C_L^0 q, \tag{2.4}$$

with C_L^0 the lift coefficients of a stationary cylinder experiencing vortex shedding. The wake variable can be seen as the normalized lift coefficient. Facchinetti, de Langre, et Biolley (2004a) sets a phenomenological coupling between q and the cross-flow acceleration of the cross section $\ddot{u}_q$ using a Van der Pol oscillator :

$$\ddot{q} + \epsilon_q \Omega_f \left(q^2 - 1 \right) \dot{q} + \Omega_f^2 q = \frac{A_q}{D} \ddot{u}_q, \tag{2.5}$$

with Ω_f the wake angular frequency. The coupling coefficients A_q and the fluid damping parameters ϵ_q are both determined empirically. Such an oscillator is known to provide quasi-harmonic oscillations of normalized amplitude $P^0 = 2$, $Q^0 = 2$ for $\Omega_f = 1$, with self-excited cycles. Indeed, when q is small, the damping of the oscillator is negative ($q^2 - 1 < 0$). The cycles are also self-limited : when q becomes large, the damping of the oscillator turns positive ($q^2 - 1 > 0$). The oscillations of the wake stabilize after the transient regime and reaches a limit-cycle, which does not depend on the initial conditions on q (Gao, Zou, Zong, Takagi, & Kang, 2019). Violette, de Langre, et Szydlowski (2007) showed that coupling the dynamics of a flexible cylinder with the Van der Pol oscillator exhibits good agreements with DNS results. The vibrations propagate in a straight geometry either as travelling waves when the structure has a free boundary (Newman & Karniadakis, 1997 ; Facchinetti et al., 2004a), standing waves when ends are pinned (Evangelinos & Karniadakis, 1999b), or a mix of both when the flow is non-uniform (Lucor, Mukundan, & Triantafyllou, 2006 ; Violette et al., 2007).

Continuous flexible structures encounter multiple lock-in regions when the different structural modes are excited (Chaplin et al., 2005 ; Trim et al., 2005 ; Willden & Graham, 2004). When multiple modes are simultaneously excited, the resulting response is characterized by multiple frequencies, which in turn leads to lower amplitudes of oscillations (Leclercq & de Langre, 2018).

When its amplitude exceeds 0.2–0.3 diameters, the in-line excitation force cannot be neglected (Sumer et al., 2006). Thus, Faccinetti phenomenological model has been enriched to include in-line VIV. Ge, Long, Wang, et Hong (2009) model, splits the drag force into a constant mean force and a fluctuating force and is now commonly used to estimate in-line VIV (L. Wang, Jiang, Dai, & Ni, 2018 ; Li, Wei, & Bai, 2020 ; Gao et al., 2021 ; Feng, Chen, Li, Xiao, & Li, 2022). The drag coefficient is coupled with a second wake variable p, following a similar Van der Pol oscillator :

$$C_D = C_D^0 + \frac{1}{2} C_{Di}^0 p, \tag{2.6}$$

$$\ddot{p} + 2\epsilon_p \Omega_f \left(p^2 - 1\right) \dot{p} + 4\Omega_f^2 p = \frac{A_p}{D} \ddot{u}_p, \tag{2.7}$$

with A_p, ϵ_p the in-line coupling coefficient and fluid damping. In this model, the in-line oscillator is designed with a vortex shedding frequency $2\Omega_f$ that is twice the one of the cross-flow oscillator. This allows us to observe the 8-shape trajectory characteristic from VIV with two degrees of freedom, observed experimentally in (Kang & Jia, 2013). While Facchinetti et al. (2004a) studied cross-flow VIV on a rigid cylinder and recommended $A_q = 12, \epsilon_q = 0.3$ from experiments, so that $A_q/\epsilon_q \approx 40$, calibrations from (Srinil & Zanganeh, 2012) showed that this ratio for coupled in-line/cross-flow VIV strongly depends on the structural damping and the mass ratio and can reach up to 2727. For two degrees of freedom VIV, typical values of the empirical parameters are $A_p = 96$, $A_q = 12$, $\epsilon_p = 0.02$, and $\epsilon_q = 0.04$. These parameter values have been widely utilized for in-line/cross-flow WOM and have been validated for slender pipes in previous studies (L. Wang et al., 2018 ; Li et al., 2020).

Aquatic plants and soft corals are flexible and interact with the flow developing large static deflections (De Langre, 2008, 2012). Strong vibration amplitudes can be expected and thus appropriate tools are required to simulate the highly non-linear dynamics of these structures. Jain et Modarres-Sadeghi (2013) experimentally observed a vortex shedding parallel to the cylinder's axis for inclination angles up to 65°. They validate the independence principle, stating that the inclined cylinders can be treated as the normal-incidence ones by considering only the component of the free stream velocity normal to the cylinder axis. With a finite element approach, the independence principle allows a straightforward extension of the WOM to inclined structures. Prior works implementing a finite element formulation of the WOM (Leclercq & de Langre, 2018 ; L. Wang et al., 2018 ; Li et al., 2020) as well as commercial codes (Ltd., 2007) have consistently defined the wake variables as additional degrees of freedom assigned to each node. However, these studies primarily focused on analyzing structures with straight geometries, neglecting the presence of forks, angles, or other complex geometric features. Consequently, the issue of having discontinuous tangent vectors at specific nodes, which can result in ill-defined cross-flow directions, has not been addressed in these prior investigations. Some studies focused on branch pipe junctions behavior under VIV (Chapuliot, Moulin, & Plancq, 2002 ; Rukavishnikov, Ryabokon, & Tkachenko, 2023) using DNS. Vedeld, Sollund, et Fyrileiv (2011) first proposed an empirical design guideline to estimate fatigue due to VIV on non-straight piping configurations. The fatigue is computed using an amplitude response model. This empirical model provides the maximum VIV amplitude response as a function of some basic hydrodynamic and structural parameters. Numerous wind-tree numerical models have been developed (Shinya & Fournier, 1992 ; Hu, Tao, & Guo, 2008 ; Rodriguez, Ploquin, Moulia, & de Langre, 2012) and various simulations of tree dynamics have been performed (Akagi & Kitajima, 2006 ; Habel, Kusternig, & Wimmer, 2009 ; Quigley, Yu, Huang, Lin, & Fedkiw, 2017). However, these studies often overlook flow instabilities and none of them uses the WOM. The modal analysis of real plants (Rodriguez et al., 2012 ; Der Loughian et al., 2014) and tree models (Rodriguez, Langre, & Moulia, 2008) has introduced techniques to simplify the complex dynamics of branching structures by identifying a small number of structural modes. The assessment of VIV on 3D branched structures like corals or trees undergoing large displacements remains an open problem.

Corotational model

Structures undergoing VIV are typically slender and can exhibit large amplitude beam-like deformations. The kinematics of a flexible frame element can be described by the total Lagrangian or the updated Lagrangian formulations, however they require a high number of elements or a small time step in order to provide proper results for nonlinear problems (Elkaranshawy, Elerian, & Hussien, 2018 ; Le, Battini, & Hjiaj, 2014). The oldest and most widely spread formulation is the total Lagrangian formulation (used in finite element commercial codes like ANSYS or ABAQUS). This formulation defines the system of equations with respect to a fixed global coordinate system that remains unchanged throughout the analysis. Handling large displacements and strains in a fixed system can make the equations very complicated. In the updated Lagrangian formulation, the geometry is updated with the last accepted solution. However, the accuracy of the computations is severely reduced with large deformations and can lead to numerical instabilities (Augarde, Lee, & Loukidis, 2021).

Crisfield, Galvanetto, et Jelenić (1997) presented a 3D corotational formulation in which the movement is separated into two parts using an element-independent framework. The first part involves rigid body motion, which includes translation and rotation from the global to the rigid system. The second part involves a small deformation motion, which goes from the rigid to the deformed configuration.

The 3D corotational framework uses three coordinate systems. The global reference system is defined by the triad $(\mathbf{e}_\mathrm{x}, \mathbf{e}_\mathrm{y}, \mathbf{e}_\mathrm{z})$. The local system attached to the element after a rigid rotation without deformation is $(\mathbf{r}_1, \mathbf{r}_2, \mathbf{r}_3)$. The triad that is rigidly attached to each node is $(\mathbf{t}_1, \mathbf{t}_2, \mathbf{t}_3)$. These coordinates systems are illustrated on Figure 4.1. Let us consider a two-node frame element, where the nodal displacements are represented by the column vector $\mathbf{d} = \left[(\mathbf{u}^1)^T, (\mathbf{w}^1)^T, (\mathbf{u}^2)^T, (\mathbf{w}^2)^T\right]^T$. Here, $\mathbf{u}^i$ and $\mathbf{w}^i$ denote the column vectors of linear displacements and rotations, respectively, at node i. These displacements can be expressed in both the global coordinate system as $\mathbf{d}_g$ and the local coordinate system as $\mathbf{d}_l$. Similarly, a vector of nodal forces $\mathbf{f}$ can also be represented in the corresponding coordinate systems. The Principle of Virtual Work (PVW) can then be stated as:

$$\delta\mathbf{d}_g^T\mathbf{f}_g = \delta\mathbf{d}_l^T\mathbf{f}_l, \tag{2.8}$$

with $\delta\mathbf{d}_g, \delta\mathbf{d}_l$ being the virtual displacements in global and local coordinates, respectively.

The internal force $\mathbf{f}_{int}$ is derived based on the work of (Battini & Pacoste, 2002). This force vector is expressed in the local coordinate system where the Bernoulli hypothesis is considered. Translations and rotations at the cross section centroid are interpolated from the local nodal values, using linear shape functions for the axial displacement and rotation, and cubic shape functions for transverse displacements.

The PVW gives:

$$\delta\mathbf{d}_g^T\mathbf{f}_{int,g} = \delta\mathbf{d}_l^T\mathbf{f}_{int,l}. \tag{2.9}$$

The virtual displacements in local coordinates is expressed by

$$\delta\mathbf{d}_l = \mathbf{B}\delta\mathbf{d}_g, \tag{2.10}$$

where $\mathbf{B}$ is a transformation matrix expressing the axial displacements and rotations from the local to the global coordinate system. It follows

$$\delta\mathbf{d}_g^T\mathbf{f}_{int,g} = \delta\mathbf{d}_g^T\mathbf{B}^T\mathbf{f}_{int,l}. \tag{2.11}$$

This is valid for any virtual displacement $\delta\mathbf{d}_g$, so:

$$\mathbf{f}_{int,g} = \mathbf{B}^T\mathbf{f}_{int,l}, \tag{2.12}$$

where $\mathbf{f}_{int,l} = \begin{bmatrix} f_{al} & (\mathbf{m}_l^1)^T & (\mathbf{m}_l^2)^T \end{bmatrix}$ is the known vector of internal forces in local coordinates. It considers the axial force f_{al} along $\mathbf{t}_1$, bending moments and torsional moment $\mathbf{m}_l^i$ at node i along $\mathbf{t}_1$ and $\mathbf{t}_2, \mathbf{t}_3$, respectively. They are given by a linear constitutive behavior. Crisfield et al. (1997) model has been extended to include dynamic problems in (Le, Battini, & Hjiaj, 2011). The inertial force is computed through the kinetic energy variations. The kinematic energy K of an element of length ℓ_0 is:

$$K = \frac{1}{2}\int_{\ell_0} \rho\dot{\mathbf{u}}^T A\dot{\mathbf{u}} + \rho\dot{\mathbf{w}}^T\mathbf{I}\dot{\mathbf{w}}dl, \tag{2.13}$$

with $\mathbf{u}, \mathbf{w}$ the displacements and rotations vectors of the center of the cross section, ρ the material density, A the cross section area and $\mathbf{I}$ the geometric inertia tensor. The dot notation stands for time differentiation. Using the derivative chain rule, the variations of Eq. (2.13) writes:

$$\delta K = -\int_{\ell_0} \delta\mathbf{u}^T\rho A\ddot{\mathbf{u}} + \delta\mathbf{w}^T[\rho\mathbf{I}\ddot{\mathbf{w}} + \tilde{\dot{\mathbf{w}}}\rho\mathbf{I}\dot{\mathbf{w}}]dl, \tag{2.14}$$

with $\tilde{\dot{\mathbf{w}}}$ the skew operator associated with the vector $\dot{\mathbf{w}}$. The inertial force vector of the element in global coordinates is:

$$\delta K = (\mathbf{f}_{\text{ine}})^T\delta\mathbf{d}_g, \tag{2.15}$$

where

$$\mathbf{f}_{\text{ine}} = \int_{\ell_0} \left\{\mathbf{H}_1^T\mathbf{R}_r^T\rho A\ddot{\mathbf{u}} + \mathbf{H}_2^T\mathbf{R}_r^T[\rho\mathbf{I}\ddot{\mathbf{w}} + \tilde{\dot{\mathbf{w}}}\rho\mathbf{I}\dot{\mathbf{w}}]\right\} dl. \tag{2.16}$$

The rigid rotation matrix $\mathbf{R}_r$ expresses $(\mathbf{r}_1, \mathbf{r}_2, \mathbf{r}_3)$ in the global coordinate system. Matrices $\mathbf{H}_1, \mathbf{H}_2$ depend on the interpolation functions which are linear for axial displacements and hermitian for bending. Their exact expression can be found in (Le et al., 2014).

Corotational frame elements have been used in fluid-structure interaction simulations to model living organisms subjected to fluid loads, such as vibrating vocal folds (Tian, Dai, Luo, Doyle, & Rousseau, 2014), or insect wings during flapping (Cho, Gong, Lee, Shin, & Lee, 2019). These studies compute the hydrodynamic forces by integrating the pressure field obtained from CFD analysis. A general and consistent corotational formulation of the drag and lift forces was recently provided in (Vanzulli & Zerpa, 2022):

$$\mathbf{f}_d = \frac{1}{2}\rho_\mathrm{f} D \mathbf{E} \int_{\ell_0} \left\{ \mathbf{H}_1^T \overline{\mathbf{R}} \| \mathbf{L}_2 \left(\mathbf{R}_r \overline{\mathbf{R}} \right)^T \mathbf{U} \| C_D \mathbf{L}_2 \left(\mathbf{R}_r \overline{\mathbf{R}} \right)^T \mathbf{U} \right\} dl, \tag{2.17}$$

$$\mathbf{f}_l = \frac{1}{2}\rho_\mathrm{f} D \mathbf{E} \int_{\ell_0} \left\{ \mathbf{H}_1^T \overline{\mathbf{R}} \| \mathbf{L}_2 \left(\mathbf{R}_r \overline{\mathbf{R}} \right)^T \mathbf{U} \| C_L \mathbf{L}_3 \mathbf{L}_2 \left(\mathbf{R}_r \overline{\mathbf{R}} \right)^T \mathbf{U} \right\} dl. \tag{2.18}$$

The rotation matrix $\left(\mathbf{R}_r \overline{\mathbf{R}}\right)^T$ is used to transform the relative fluid velocity, $\mathbf{U}$, into local coordinates. The operator $\mathbf{L}_2$ projects it onto the section plane Π_{23} and $\mathbf{L}_3 = \exp([\pi/2, 0, 0]^T)$ rotates it by $\pi/2$ radians around this plane to provide the local lift direction. Finally, $\overline{\mathbf{R}}$ and $\mathbf{E}$ transform the velocity from local to rigid and from rigid to global coordinates, respectively (Battini & Pacoste, 2002 ; Vanzulli & Zerpa, 2022).

This formulation handles large rotations and large displacements, obtaining accurate results with a smaller number of elements (Le et al., 2014).

CHAPTER 3 RESEARCH OBJECTIVES

Literature review summary

The investigation of soft coral vibrations, as observed by Gosselin (2019), lies at the intersection of biology, flexible structure dynamics, and flow-induced vibrations, making this project inherently multidisciplinary. In his Master's thesis, Boudina (2020) sheds light on the potential benefits of VIV for soft corals, particularly in enhancing their feeding capabilities. His 2D CFD simulations demonstrated that the presence of VIV in a cross section increased the interception rate by up to 40% compared to a fixed section. This project seeks to expand the investigation to incorporate the 3D aspect of coral geometry and further explore its biological implications.

Considering the computational complexity of running 3D simulations, a fully coupled approach of the FSI system appears impractical. Thus the WOM proposed by Facchinetti et al. (2004a) enriched with the in-line VIV model by Ge et al. (2009) emerges as a suitable and computationally efficient alternative. Soft corals are flexible and thus bend under the waves with large deflections (De Langre, 2008, 2012). The corotational model first developed by Crisfield et al. (1997), then extended to dynamic problems for frame elements by Le et al. (2014) appears ideal to compute such large displacements and rotations. Its finite element implementation including hydrodynamic forces is done in the open source solver for nonlinear structural analysis ONSAS[1] Pérez Zerpa et al. (2022) by Vanzulli et Zerpa (2022), presenting an excellent platform to incorporate the WOM into the force model for comprehensive consideration of VIV.

Does the 40% interception increase still hold true for a cantilever beam? How do the branches impact the vortex-induced dynamics of the structure? Should soft corals grow branches in order to better capture particles? By addressing these questions, this thesis aims to deepen our understanding of flow-induced dynamics of branched structures, and its biological impact on corals feeding.

Thesis objectives

From the literature review, we can formulate three research objectives for this thesis.

➢ Develop a consistent formulation of the WOM inside the corotational framework. Use

---

[1] `www.onsas.org`

the hydrodynamic formulation from Vanzulli et Zerpa (2022). Implement a numerical resolution procedure for simulating the finite Element Method (FEM) model under ONSAS (Pérez Zerpa et al., 2022). This numerical procedure is first verified with an analytical solution in small displacements, small rotation. The cross flow model is then validated in large displacements against a wake-oscillator from the literature, using the code used to generate results in Leclercq et de Langre (2018). The in-line VIV are validated against experimental data from Trim et al. (2005).

- Conduct an experimental study of VIV on a flexible structure with branches. Three geometries, with 0, 1 and 2 pairs of branches are 3D-printed from flexible and elastic material and submitted to a uniform steady flow in a water tunnel. A camera filming in the stream direction records the transverse displacements. A post-processing code is developed to detect the tip of the trunk, and extract its transverse displacements. Vibration amplitudes and frequencies are compared to simulations.
- Provide biological insights about the influence of the 3D vortex-induced dynamics of branches on the particle interception. In-line/cross-flow VIV simulations are performed on different geometries to discuss the influence of the number of branches. Linear modal analysis of the branched geometries is developed to analyse the frequency spectrum obtained from simulations. The 2D interception model developed in Boudina et al. (2021) is applied at each node of the 3D structure and a global interception gain is computed for different geometries.

CHAPTER 4 METHODOLOGY

In this chapter, we introduce our proposed corotational formulation for the added mass force and the wake-oscillator model, along with a numerical procedure for solving the governing equations. Additionally, we provide a detailed description of the experimental method used to validate our model.

4.1 Corotational formulation of the hydrodynamic forces

The formulation is developed for a frame element with a length ℓ_0 and a circular, uniform cross section of diameter D and second moment of inertia I. The material is considered to be elastic and isotropic, of density ρ and elasticity modulus E. The structure is submitted to a uniform and steady flow of velocity $\mathbf{U}$ and density ρ_{f} (Fig. 4.1).

The hydrodynamic forces acting on the structure are the added mass, the drag and lift forces. We define the relative velocity $\mathbf{U}_{\mathrm{rel}}$ that the cylinder receives based on $\mathbf{U}$ and the cylinder velocity $\dot{\mathbf{u}}$: $\mathbf{U}_{\mathrm{rel}} = \mathbf{U} - \dot{\mathbf{u}}$. In this formulation, the computation of the fluid forces is performed at every instant in each section plane by considering only the normal component of the flow velocity, as stated by the independence principle. Thus, the fluid velocity and relative velocity are projected on the cross section plane Π_{23}. We define the vector $\mathbf{t}_{\mathrm{U}}$ as the normalized projection of $\mathbf{U}$ on the cross section plane in local coordinates:

$$\mathbf{t}_{\mathrm{U}} = \mathbf{L}_2 \left(\mathbf{R}_{\mathrm{r}}\overline{\mathbf{R}}\right)^T \mathbf{U} / \|\mathbf{L}_2 \left(\mathbf{R}_{\mathrm{r}}\overline{\mathbf{R}}\right)^T \mathbf{U}\|, \tag{4.1}$$

with $\left(\mathbf{R}_r\overline{\mathbf{R}}\right)^T$ being the rotation matrix used to transform the relative fluid velocity, $\mathbf{U}_{\mathrm{rel}}$, into local coordinates. The operator $\mathbf{L}_2$ projects it onto the section plane Π_{23}. $\mathbf{t}_{\mathrm{U}}$ provides the flow direction seen by the cross section. The fluid velocity in the cross section plane is $\mathbf{U} - \mathbf{U} \cdot \mathbf{t}_1 = U\cos(\phi)\mathbf{t}_{\mathrm{U}}$, with ϕ being the angle between the fluid velocity $\mathbf{U}$ and Π_{23}. A 3D and planar representation of these vectors and angles is provided in Fig. 4.1.

4.1.1 Proposed corotational formulation of the added mass force

The added mass force per unit length acting on the section is:

$$\mathbf{f}_a(s,t) = m_{\mathrm{a}} \left(\dot{\mathbf{U}}(s,t) - \ddot{\mathbf{u}}(s,t)\right), \tag{4.2}$$

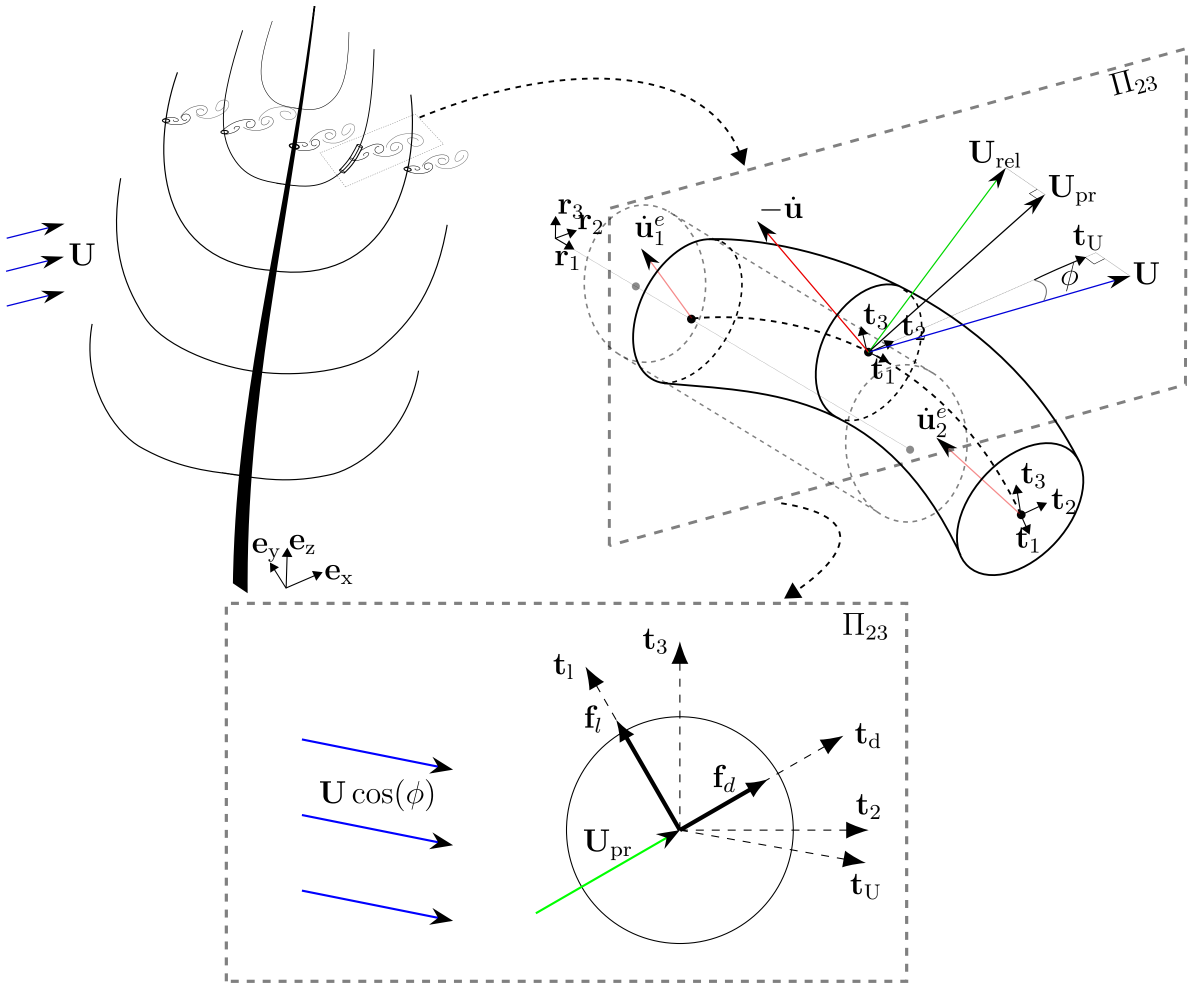

FIGURE 4.1 3D an planar illustration of corotational kinematics and hydrodynamics forces.

with $m_{\mathrm{a}} = C_a \rho_{\mathrm{f}} D\pi/4$ being the fluid added mass. The added mass coefficient C_a is assumed to be 1 for a circular cross section (Blevins, 1990). Here, the flow is considered as steady: $\dot{\mathbf{U}} = 0$. The corotational formulation of the added mass force acting on a beam element of length ℓ_0 is expressed as the inertial force of the same element having a density $C_a \rho_{\mathrm{f}}$ using Eq. (2.16):

$$\mathbf{f}_{am} = -\int_{\ell_0} \left\{ \mathbf{H}_1^T \mathbf{R}_{\mathrm{r}}^T C_a \rho_{\mathrm{f}} A \ddot{\mathbf{u}} + \mathbf{H}_2^T \mathbf{R}_{\mathrm{r}}^T [C_a \rho_{\mathrm{f}} \mathbf{I} \ddot{\mathbf{w}} + \tilde{\dot{\mathbf{w}}} C_a \rho_{\mathrm{f}} \mathbf{I} \dot{\mathbf{w}}] \right\} dl. \tag{4.3}$$

The negative sign ensures that this external force is opposed to the section acceleration. This model neglects the added mass contribution from fluid acceleration $C_a \rho_{\mathrm{f}} D\pi/4\dot{\mathbf{U}}$ and is only applicable to steady flows.

4.1.2 Corotational formulation of the wake-oscillator model

A wake-oscillator approach is used to model the fluctuating pressure field on the cylinder resulting from vortices in its wake. The corotational formulation of the WOM incorporates the drag and lift forces, as defined in Eqs (4.4,4.5). These forces are coupled to two scalar wake variables p and q for each beam element, as described in Eqs (2.6, 2.4). Consequently, the hydrodynamic forces acting on the element are obtained as follows:

$$\mathbf{f}_d = \frac{1}{2}\rho_{\mathrm{f}} D \mathbf{E} \int_{\ell_0} \left\{ \mathbf{H}_1^T \overline{\mathbf{R}} \| \mathbf{L}_2 \left(\mathbf{R}_r \overline{\mathbf{R}} \right)^T \mathbf{U}_{\mathrm{rel}} \| \left(C_D^0 + \frac{1}{2} C_{Di} p \right) \mathbf{L}_2 \left(\mathbf{R}_r \overline{\mathbf{R}} \right)^T \mathbf{U}_{\mathrm{rel}} \right\} dl, \tag{4.4}$$

$$\mathbf{f}_l = \frac{1}{2}\rho_{\mathrm{f}} D \mathbf{E} \int_{\ell_0} \left\{ \mathbf{H}_1^T \overline{\mathbf{R}} \| \mathbf{L}_2 \left(\mathbf{R}_r \overline{\mathbf{R}} \right)^T \mathbf{U}_{\mathrm{rel}} \| \frac{1}{2} C_L^0 q \mathbf{L}_3 \mathbf{L}_2 \left(\mathbf{R}_r \overline{\mathbf{R}} \right)^T \mathbf{U}_{\mathrm{rel}} \right\} dl. \tag{4.5}$$

Both wake variables p, q follow nonlinear Van der Pol oscillators coupled to the section acceleration as described in Eqs (2.7, 2.5). The in-line and cross-flow accelerations of any cross-section in the frame element are defined in 3D as:

$$\ddot{u}_p = \ddot{\mathbf{u}} \cdot \mathbf{t}_{\mathrm{U}}, \tag{4.6}$$

$$\ddot{u}_q = \ddot{\mathbf{u}} \cdot (\mathbf{t}_1 \times \mathbf{t}_{\mathrm{U}}). \tag{4.7}$$

At a bifurcation or branch node, both $\mathbf{t}_1$ and $\mathbf{t}_{\mathrm{U}}$ are discontinuous. Therefore, $\ddot{u}_p$ and $\ddot{u}_q$ at this node are ill-defined. To avoid this issue, we set the wake variables as uniform on each element where $\mathbf{t}_1$ and $\mathbf{t}_{\mathrm{U}}$ remain continuous. Therefore, the Van der Pol oscillator is solved once per element. This novel approach enables the application of the WOM to interconnected frame elements, accommodating arbitrary connections such as forks and sharp angles. For both in-line and cross-flow oscillators, the coupling is done by averaging the two nodal accelerations of the element:

$$\ddot{p} + 2\epsilon_p\Omega_f\left(p^2 - 1\right)\dot{p} + 4\Omega_f^2 p = \frac{A_p}{D}\left(\ddot{u}_p^1 + \ddot{u}_p^2\right)/2, \tag{4.8}$$

$$\ddot{q} + \epsilon_q\Omega_f\left(q^2 - 1\right)\dot{q} + \Omega_f^2 q = \frac{A_q}{D}\left(\ddot{u}_q^1 + \ddot{u}_q^2\right)/2, \tag{4.9}$$

where $\Omega_f = 2\pi S_t U \cos\phi / D$ is the wake angular frequency. The subscripts $\cdot_p$ and $\cdot_q$ denote the in-line and cross-flow directions, respectively, and the superscripts $\cdot^1$ and $\cdot^2$ refer to the element nodes.

Note that the fluid damping is included in the drag force. Indeed, as pointed out by Ogink et Metrikine (2010), a linearized form of the instantaneous drag force can lead to a fluid damping term proportional to the section velocity, named stall term by Skop et Balasubramanian (1997) ; Facchinetti, de Langre, et Biolley (2004b). In the 2D VIV, this hypothesis may not be respected. Here, we consider the full nonlinear drag force following (Ogink & Metrikine, 2010 ; Qu & Metrikine, 2020).

When attempting to solve for the dynamics of a branched structure, a system of differential equations needs to be solved for each branch, and continuity conditions must be imposed at the bifurcation nodes, which results in a significant increase in the complexity of the problem. In the proposed formulation, the FEM assembly approach is considered. Therefore, no complexity is added by including a fork node in the structure.

4.2 Balance equations and numerical resolution procedure

4.2.1 Coupled formulation

The governing equations are derived by applying the principle of virtual work to all elements of the structure for the forces described in Eqs.(2.16, 4.3, 4.5, 4.4), while simultaneously solving the Van der Pol equations, Eqs.(4.8, 4.9), for each element.

We denote the structure assembled vectors with subscripts $\cdot_s$ and elements variables with superscripts $\cdot^e$. The solid and wake residuals are:

$$\begin{cases} \mathbf{r}_u = \mathbf{f}_{int,s}(\mathbf{d}_s) + \mathbf{f}_{ine,s}(\mathbf{d}_s, \dot{\mathbf{d}}_s, \ddot{\mathbf{d}}_s) - \mathbf{f}_{am,s}(\ddot{\mathbf{d}}_s) - \mathbf{f}_{d,s}(\mathbf{d}_s, \dot{\mathbf{d}}_s, \mathbf{p}_s) - \mathbf{f}_{l,s}(\mathbf{d}_s, \dot{\mathbf{d}}_s, \mathbf{q}_s), & \\ r_p^e = \ddot{p}^e + 2\epsilon_p\Omega_f\left({p^e}^2 - 1\right)\dot{p}^e + 4\Omega_f^2 p^e - \frac{A_p}{D}\left(\ddot{u}_p^{e,1} + \ddot{u}_p^{e,2}\right)/2, & e = 1, \ldots, N_e \\ r_q^e = \ddot{q}^e + \epsilon_p\Omega_f\left({q^e}^2 - 1\right)\dot{q}^e + \Omega_f^2 q^e - \frac{A_q}{D}\left(\ddot{u}_q^{e,1} + \ddot{u}_q^{e,2}\right)/2, & \end{cases} \tag{4.10}$$

where $\mathbf{r}_u$ is the residual of the PVW equations, and the wake residuals r_p^e, r_q^e correspond to the Van der Pol equations. They are both computed independently for each element. For each time step, the system $\mathbf{r}_u = \mathbf{0}; r_p = r_q = 0$ must be solved, obtaining the current configuration of the structure (with velocities and accelerations) and wake variables for each element.

We define the following non-dimensional parameters: the reduced velocity, the Reynolds number, the aspect ratio and the mass ratio, respectively,

$$U_R = \frac{U}{D\ell^2}\sqrt{\frac{m_\mathrm{s} + m_\mathrm{a}}{EI}}, \quad R_\mathrm{e} = \frac{UD}{\nu_\mathrm{f}}, \quad \Gamma = \frac{\ell}{D}, \quad \mathcal{M} = \frac{\rho}{\rho_\mathrm{f}}, \tag{4.11}$$

with m_s being the structural mass per unit length and ν_f the fluid kinematic viscosity.

4.2.2 Numerical resolution methods

The system of nonlinear governing Eq. (4.10) is solved numerically using iterative methods. The internal forces are implemented according to the formulations described in (Le et al., 2014 ; Battini & Pacoste, 2002). The inertial forces in Eq. (2.16) and hydrodynamic forces in Eqs (4.3, 4.5, 4.4) are computed with 4 Gauss integration points. The tangent matrices of the hydrodynamic forces are considered for large displacement examples as recommended in Ref. (Vanzulli & Zerpa, 2022). The trapezoidal Newmark numerical method is used to solve the dynamic problem Eq. (4.10) with $\alpha = 1/4$, $\delta = 1/2$ (Bathe, 2006).

To solve for r_p and r_q in Eq. (4.10), a fourth-order Runge-Kutta algorithm (implemented using the `ode45` function in Matlab) solves the nonlinear Van der Pol equations Eqs (2.5, 2.7) with constant nodal accelerations $\ddot{\mathbf{u}}^1, \ddot{\mathbf{u}}^2$ at each Newton iteration. The wake variables (p, q) are defined as uniform in the element. In all of the examples, two stopping criteria are considered based on either the norm of the relative displacement, $||\Delta\mathbf{u}||/\mathbf{u} <$ tol $_u$, or the norm of the residual force, $r_u <$ tol $_r$. Both criteria are used to determine convergence of the numerical solution. Algorithms 1 and 2 describe the iterative procedure for resolution.

For non-homogeneous initial configurations, the numerical method is initialized with a given deformed configuration and initial velocities and accelerations. To start from the steady state, the Newton-Raphson method solves the static problem and obtain the initial configuration.

4.3 Experimental method

4.3.1 Experimental setup

We carry an experimental study of the cross-flow VIV in uniform flow. Three different model geometries are studied, with $N = 0, 1, 2$ pairs of branches. The planar branched geometry

Algorithm 1 Numerical procedure

```
Initialize the structure $u_t \leftarrow u_0,\ \ \dot{u}_t \leftarrow \dot{u}_0,\ \ddot{u}_t \leftarrow \ddot{u}_0$
Initialize the wake $(p^{k+1}, \dot{p}^{k+1}, q^k, \dot{q}^{k+1}) \leftarrow (p_0, \dot{p}_0, q_0, \dot{q}_0)$
while $t < t_f$ do
    Initial guess for $t + \Delta t$ : $(\mathbf{u}^k, \dot{\mathbf{u}}^k, \ddot{\mathbf{u}}^k) \leftarrow (\mathbf{u}_t, \dot{\mathbf{u}}_t, \ddot{\mathbf{u}}_t)$
    Compute $\mathbf{r}_u^{k+1}$ and assemble the tangent matrix
    while $\|\Delta\mathbf{u}^{k+1}\| > \text{tol}_u$ & $\|\mathbf{r}_u^{k+1}\| > \text{tol}_r$ & $k < \text{max}_{iter}$ do
        Compute $\Delta\mathbf{u}^{k+1}$
        Update $\mathbf{u}^{k+1} \leftarrow \mathbf{u}^k + \Delta\mathbf{u}^{k+1}$
        Newmark method gives next candidates $\dot{\mathbf{u}}^{k+1}, \ddot{\mathbf{u}}^{k+1}$
        Algorithm 2 computes wake variables: $p^{k+1}(\ddot{\mathbf{u}}^{k+1})$, $q^{k+1}(\ddot{\mathbf{u}}^{k+1})$
        Update $\mathbf{f}_{int,s}^{k+1}(\mathbf{u}^{k+1})$, $\mathbf{f}_{ine,s}^{k+1}(\mathbf{u}^{k+1}, \dot{\mathbf{u}}^{k+1}, \ddot{\mathbf{u}}^{k+1})$, $\mathbf{f}_{flu,s}^{k+1}(\mathbf{u}^{k+1}, \dot{\mathbf{u}}^{k+1}, p^{k+1}, q^{k+1})$
        Compute $\mathbf{r}_u^{k+1}(\mathbf{u}^{k+1}, \dot{\mathbf{u}}^{k+1}, \ddot{\mathbf{u}}^{k+1})$ and assemble the tangent matrix
    end while
    $(\mathbf{u}_{t+\Delta t}, \dot{\mathbf{u}}_{t+\Delta t}, \ddot{\mathbf{u}}_{t+\Delta t}, p_{t+\Delta t}, q_{t+\Delta t}) \leftarrow (\mathbf{u}^{k+1}, \dot{\mathbf{u}}^{k+1}, \ddot{\mathbf{u}}^{k+1}, p^{k+1}, q^{k+1})$
    $t \leftarrow t + \Delta t$
end while
```

Algorithm 2 Wake equations resolution

```
Returns Wake variables candidates $p^{k+1}$, $q^{k+1}$ of the element for time $t + \Delta t$
Initial guess $(p^{k+1}, \dot{p}^{k+1}, q^k, \dot{q}^{k+1}) \leftarrow (p_t, \dot{p}_t, q_t, \dot{q}_t)$
Compute averaged element in-line and cross-flow accelerations $\ddot{\mathbf{u}}_p^{k+1}, \ddot{\mathbf{u}}_q^{k+1}$ using Eqs (4.6, 4.7)
Compute $r_p(p^{k+1}, \dot{p}^{k+1}, \ddot{\mathbf{u}}_p^{k+1})$ and $r_q(q^k, \dot{q}^{k+1}, \ddot{\mathbf{u}}_q^{k+1})$ using Eqs (4.8,4.9)
ode45 solves $r_p = 0$
ode45 solves $r_q = 0$
$(p^{k+1}, \dot{p}^{k+1}) \leftarrow (p_{ode}, \dot{p}_{ode})$
$(q^k, \dot{q}^{k+1}) \leftarrow (q_{ode}, \dot{q}_{ode})$
```

is inspired by the gorgonian soft coral *Antillogorgia bipinnata*, which grows perpendicular to the ambient flow (Ribes et al., 1998). We denote as "trunk" the vertical cylinder to which the branches are attached. When $N = 0$, the trunk simply refers to the cylinder itself. The open-source software Fusion360 is used to design the 3D geometries. The elongated structure are printed with Selective Laser Sintering (SLS) using the Sinterit Lisa Pro printer in Polytechnique Montreal fabrication laboratory *Polyfab*. This 3D printing technology allows us to create complex geometries without supports by selectively fusing layer by layer polymer powder using a high-powered laser. The printed material is Thermoplastic Elastomer (TPE powder) known for its elasticity and flexibility. The three models are presented in Fig. 4.2.

The structures height are limited by the maximum length achievable by the printer: $\ell = 150$ mm. We selected a circular cross section with a diameter of $D = 5$ mm. This choice strikes a balance between having a high slenderness ($\Gamma = 30$) and achieving a satisfactory surface resolution. Branches have a length of $\ell_b = 80$ mm and are connected to the trunk at an angle of $\beta = 60°$. Note that this geometry is a coarsely represents the soft coral *Antillogorgia bipinnata* (Bayer, 1961 ; Coelho, 2018). The parameters for the model and the real coral are compared in Tab. 4.1. The aspect ratio of the branches Γ and angle of the branches β are similar. Since the material is porous, its density ρ is calculated by dividing its wet weight by its volume. To do so, we leave the heaviest structure ($N = 2$) fully immersed in a water container in order to remove all the air from the porous material. Its weight is measured by a precision scale to $m_s = 7.30$ g. The volume is provided by Fusion 360: $V_s = 9.21 \times 10^{-6}$ m^3. The ratio gives the wet density $\rho_s = 7.9 \times 10^2$ kg/m^3. A three-points bending test with a MTS insight provides the bending rigidity of the structure. The bending test procedure is detailed in Appendix A. We find a bending rigidity $EI = 4 \times 10^2$ N mm^2.

The structure is placed in a closed water tunnel, which is operated by two pumps. The main pump is used for flow velocities ranging from 0.13 m/s to 9 m/s, while the secondary pump is utilized to achieve flow velocities below 0.18 m/s. One flow meter measures the flow rate for each pump, which is then converted to a mean flow velocity in the test section. A detailed specification on the rig can be found in Dhar (2020). The test section area is 250 × 250 mm^2. The bottom end of the cylinder is screwed on a M5 hexagonal nut which is

TABLE 4.1 Geometric parameters of the printed model and the soft coral *Antillogorgia bipinnata*

Parameters	ℓ (mm)	ℓ_b (mm)	D (mm)	β (°)
Printed model	150	80	5	60
Antillogorgia bipinnata	570	25 - 40	1 - 1.5	65

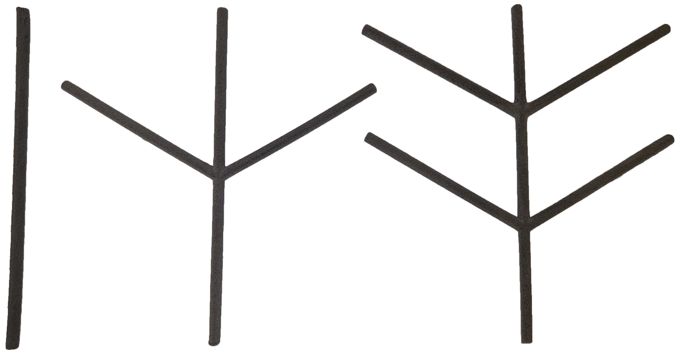

FIGURE 4.2 3D printed models with $N = 0, 1, 2$ pairs of branches

embedded to the support plate. The quantities of interest are the amplitude and frequency of the transverse displacements at the tip as they vary with the reduced velocity. The flow velocity U is varied in steps, and for each step, we wait 30 seconds for the steady-state regime to establish. Then, a Go Pro Hero Black 12 records a 4K-quality movie for 20 seconds ($\sim$ 100 periods) of the transverse displacements at a frame rate of 120 frames per second. The camera is positioned 340 mm downstream from the structure, as shown in Fig. 4.3. This distance satisfies a compromise between a sufficient pixel resolution in the captured images (as the Go Pro does not have a built-in optical zoom) and ensuring that it does not cause interference with the upstream flow. We suppose without further verification this non-interference hypothesis since the wake of a cylinder is a few diameters long and the Go Pro is placed $68D$ behind the clamping point of the structure. Two LED panels are positioned on both sides of the section to illuminate the structure and enhance the contrast with the dark background.

4.3.2 Images post-processing

The quantity of interest is the tips transverse displacements. The objective of the post-processing is to provide a consistent routine able to accurately detect the tips on the image sequence.

A Matlab image processing script is developed to detect the tips on each frame. Fig. 4.4 displays the different steps of the process. The frames sequence is first converted to 8bit gray scale images and binarized with a threshold, to separate the structure from the background. Thanks to the LED panels, the trunk edges appear bright, ensuring a satisfactory contrast with the background. However, unlike the trunk, there is a poor contrast between the branches

Figure 4.3 Experimental setup for $U = 0.56$ m/s ($U_R = 20$). Flow direction is from left to right

and the image background. Indeed, the branches overlap with the bright edges of the section (green vertical bands in Fig. 4.4.a). We tried to numerically remove this vertical band by subtracting the average pixel value over the recording, or detecting pixels with color changes between consecutive frames. These methods resulted in the removal of pixels within the structure, compromising the quality of the cut. Thus, the focus is only on the trunk tip. A global threshold on the image using the Matlab function `imbinarize` is enough to cut the trunk. To eliminate the presence of certain grid parts in the binarized image, we extract the largest connected component, which refers to the largest region of connected white pixels. This step effectively removes any unconnected blocks of pixels that are not linked to the trunk. In addition, we find undetected pixels at the center of the cylinder, which appear black due to the relatively darker shade compared to the edges. Any connected block of zeros surrounded by ones is considered as valid pixels and converted to ones (the hollow spots are filled).

A quadratic regression curve is then fitted on the cylinder pixels to follow its center line. The tip stands on the end of this regression line. We estimate the detection error of the tip to be approximately 1 pixel = 0.1 mm. As the displacements are normalized by the cylinder diameter D, the error is 2%. Each root mean square value of a 20-seconds recording counting more than 2000 values, the standard error becomes negligible compared to experiments repeatability.

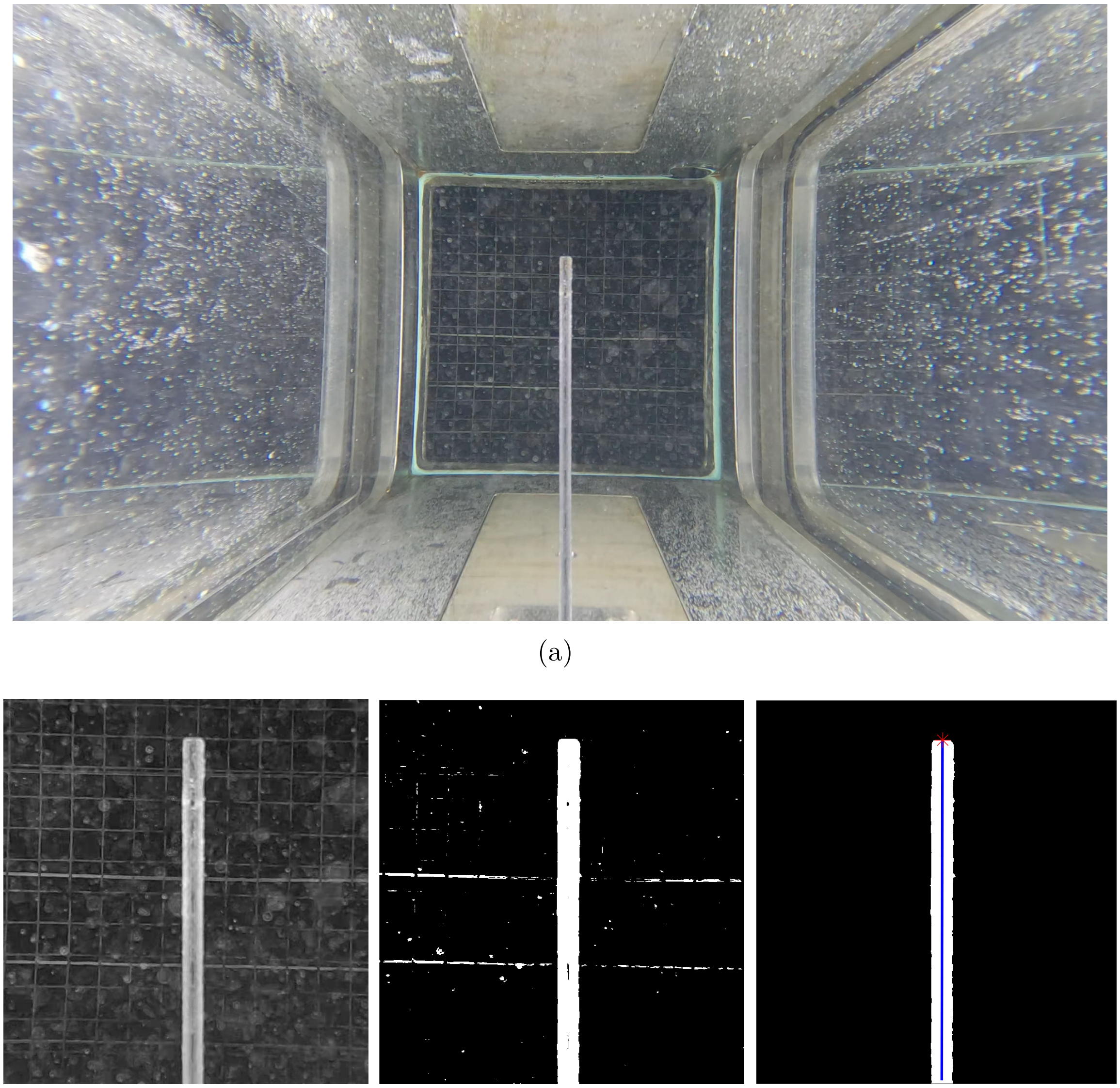

(a)

(b) (c) (d)

Figure 4.4 Image processing steps on the $N = 0$ structure. The original frame (a) is first cropped around the the region of interest and converted to gray scale (b). Then, a threshold is applied to have a binary image (c). Finally, the image is cleaned and a polynom is fitted on the white pixels (—), stopping at the tip (*) (d)

4.3.3 Damping test

In order to assess the structural damping coefficient of the TPE material, a damping test is performed on the cylinder ($N = 0$). The structure is clamped at one end, and an initial transverse displacement is applied at the free tip. A release from this deformed configuration without any initial velocity mainly excites the first mode of vibration. It is assumed that the damping coefficient measured for this first mode is representative of the damping behavior across all vibration modes. This hypothesis allows for a simplified characterization of the structural damping properties of the cylinder. The transverse response of the structure is then recorded at 60 frames per seconds, over 10 periods of oscillations. The regime is considered pseudo-oscillatory: the tip transverse displacement is of the form

$$u_{\mathrm{y}}(t) = u_{\mathrm{y}}(0)\cos\left(2\pi\frac{t}{T}\right)e^{-\zeta\omega_n t} \tag{4.12}$$

with T the period of oscillation, ω_n is the natural frequency and ζ the damping ratio. It relates to the damping coefficient: $\zeta = r_s/2\omega_n$. To quantify the decay of vibration amplitudes we compute the logarithmic decrement δ_l, which is a measure of the rate at which the vibration amplitude decreases over successive cycles. It is defined as:

$$\zeta = \frac{\delta_l}{\sqrt{\delta_l^2 + (2\pi)^2}}, \quad \delta_l = \log\left(\frac{U_{i+1}}{U_i}\right). \tag{4.13}$$

where U_i, U_{i+1} are the amplitudes of any two successive peaks.

In the FEM, the damping coefficient r_s multiplies the velocity vector of all the elements, so the structural damping depends on the element length l_0. To simulate the TPE material, we work with a fixed element length for which we determine the correct damping coefficient. By carefully selecting this element length associated with the proper damping, we can ensure that the structural damping properties of the TPE material are properly represented in the simulations. We run several simulations of the damping test with the same initial conditions as in the experiment, with varying r_s. For each simulations, the logarithmic decrement δ_l is computed between each successive peaks over 10 periods and averaged, then the damping ratio ζ is computed. When it matches the experimental damping ratio $\zeta = 0.023$, the damping coefficient r_s is selected for this length of element. Results for $10, 20, 50$ elements are presented in Tab. 4.2. Fig. 4.5 compares the evolution of the tip transverse displacements with time from the simulations and experiments over 10 periods. We chose to model the trunk with 50 frame elements and the branches with $50\ell/\ell_b$ elements, so that all the elements have the same length and the value $r_s = 6 \times 10^{-5}$ can be used.

TABLE 4.2 Damping coefficients matching the experimental damping ratio for different element lengths

Number of elements	10	20	50
Element length (mm)	$1.4{\times}10^{-2}$	$7.0{\times}10^{-3}$	$2.8{\times}10^{-3}$
Damping coefficient (kg/s)	$2.4{\times}10^{-4}$	$1.3{\times}10^{-4}$	$6.0{\times}10^{-5}$

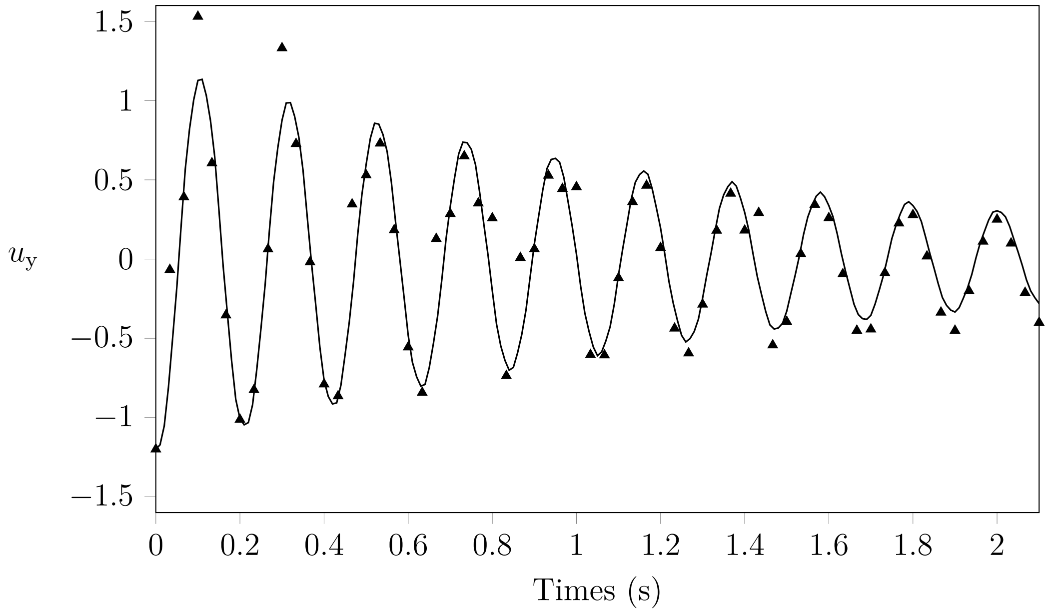

FIGURE 4.5 Time evolution of the tip of the cylinder transverse displacements in air. The simulation (——) using 50 elements and $r_s = 6 \times 10^{-5}$ is compared to experimental results (▲)

CHAPTER 5 MODEL VALIDATION

This chapter presents comparisons to validate the implementation of the model. For all the examples, the fluid considered is water. Gravitational and buoyancy forces are neglected. To ensure deterministic results, we initialize the wake variables p and q with a uniform value of 0.001. The stopping criteria have default values $\text{tol}_{\,r} = 10^{-5}, \text{tol}_{\,u} = 10^{-8}$.

In the subcritical range $300 < \text{Re} < 1.5 \times 10^5$, the values of C_D^0, C_{Di}^0, C_L^0 and S_t for a fixed cylinder are commonly assumed constant (Facchinetti et al., 2004a ; Gao et al., 2021) with values given in Tab. 5.1. For all the examples, the fluid considered is water with density $\rho_\text{f} = 10^3$ kg/m^3 and kinematic viscosity $\nu_\text{f} = 10^{-6}$ mm^2/s. While Facchinetti et al. (2004a) studied cross-flow VIV on a rigid cylinder and recommended $A_q = 12, \epsilon_q = 0.3$ from experiments, so that $A_q/\epsilon_q \approx 40$, calibrations from Srinil et Zanganeh (2012) showed that this ratio for coupled in-line/cross-flow VIV strongly depends on the structural damping and the mass ratio and can reach up to 2727. In this work, unless otherwise mentioned, empirical parameters of the wake-oscillator are set to $A_p = 96, A_q = 12, \epsilon_p = 0.02, \epsilon_q = 0.04$. This set of parameters is widely used for in-line/cross-flow WOM and have been validated for slender pipes (L. Wang et al., 2018 ; Li et al., 2020). The frequencies are normalized by the first natural frequency f_1. The i^{th} mode natural frequency of a clamped-free cylinder in water is given by :

$$f_i = \frac{\lambda_i^2}{2\pi\ell^2}\sqrt{\frac{EI}{m_s + m_\text{a}}}, \tag{5.1}$$

where λ_i is the modal parameter for the ith mode of vibration (R. D. Blevins, 2015). It's value for the three first modes are provided in Tab. 5.2. The codes are made publicly available on GitHub on this link.

Table 5.1 Dimensional and dimensionless parameters values for each example

<table>
<tr><th>Parameter</th><th>Example 1</th><th>Example 2</th><th>Example 3</th><th>Example 4</th><th>Example 5</th><th>Example 6</th></tr>
<tr><td colspan="7">Dimensional</td></tr>
<tr><td>ℓ (mm)</td><td>1000</td><td>3000</td><td>200</td><td>1000</td><td>37800</td><td>150</td></tr>
<tr><td>D (mm)</td><td>10</td><td>1</td><td>10</td><td>1</td><td>27</td><td>5</td></tr>
<tr><td>E (GPa)</td><td>30</td><td>10000</td><td>0.5</td><td>50</td><td>36.2</td><td>0.014</td></tr>
<tr><td>Θ (kN)</td><td colspan="4">0</td><td>5</td><td>0</td></tr>
<tr><td>ρ (kg/m^3)</td><td>700</td><td colspan="3">1000</td><td>1600</td><td>792</td></tr>
<tr><td>ρ_f (kg/m^3)</td><td colspan="6">1000</td></tr>
<tr><td>U (m/s)</td><td>N/A</td><td>0</td><td>0.05</td><td>N/A</td><td>0.4</td><td>N/A</td></tr>
<tr><td colspan="7">Dimensionless</td></tr>
<tr><td>$\mathcal{M}$</td><td>0.7</td><td colspan="3">1</td><td>1.6</td><td>0.79</td></tr>
<tr><td>Γ</td><td>100</td><td>3000</td><td>20</td><td>1000</td><td>1400</td><td>30</td></tr>
<tr><td>S_T</td><td colspan="6">0.2</td></tr>
<tr><td>C_D^0</td><td>1.2</td><td>1.2</td><td>1.2</td><td>2</td><td>1.2</td><td>N/A</td></tr>
<tr><td>C_{Di}^0</td><td colspan="2">N/A</td><td>0.2</td><td>N/A</td><td colspan="2">0.2</td></tr>
<tr><td>C_L^0</td><td colspan="6">0.3</td></tr>
<tr><td>A_p</td><td colspan="2">N/A</td><td>96</td><td>N/A</td><td colspan="2">96</td></tr>
<tr><td>A_q</td><td colspan="2">N/A</td><td colspan="4">12</td></tr>
<tr><td>ϵ_p</td><td colspan="2">N/A</td><td>0.02</td><td>N/A</td><td colspan="2">0.02</td></tr>
<tr><td>ϵ_q</td><td colspan="2">N/A</td><td>0.04</td><td>0.3</td><td>0.04</td><td>0.04</td></tr>
</table>

Table 5.2 Modal parameters for the first three modes of a flexible cantilever beam with constant cross section

Mode number i	1	2	3
λ_i	1.87510	4.69409	7.85476

5.1 Example 1: Reconfiguration validation

In this example, we validate the steady reconfiguration of a cantilever beam under drag flow.

A clamped-free cantilever beam with a circular cross section is submitted to a uniform flow of velocity U.

To study this problem, we define the dimensionless Cauchy and reconfiguration numbers as follow :

$$C_{\mathrm{Y}} = \frac{\rho_{\mathrm{f}} \ell^3 U^2}{16EI}, \quad \mathcal{R} = \frac{F_d}{1/2 \rho_{\mathrm{f}} L D C_D U^2}. \tag{5.2}$$

The reconfiguration number is defined as the ratio of the drag force on the structure F_d to the drag force on the same rigid structure. The Cauchy number is the the ratio of the inertial forces to the elastic forces acting on the structure and indicates how much the fluid affects the deformation of the structure. The fluid velocity U takes 20 values in the range $[0.14; 4.5]$ m/s such that the C_{Y} increases linearly. Since the solution can reach large deformations, the stiffness aerodynamic matrix is computed as recommended in (Vanzulli & Zerpa, 2022). Reference data are generated from the publicly available script [1] used in (Gosselin, de Langre, & Machado-Almeida, 2010).

Fig. 5.1 shows the evolution of the reconfiguration number against the Cauchy number, both displayed in logarithmic scales. In the first regime for $C_{\mathrm{Y}} C_D < 1$, the cylinder stays pretty straight and the drag force acting on it is similar to the one on the undeformed structure. For $C_{\mathrm{Y}} C_D > 1$, the bending becomes significant. As the structure bends, its surface area exposed to the flow direction decreases, which in turn changes the drag force acting on the structure. This nonlinearity in the drag force due to the change in surface area is referred to as reconfiguration. This phenomenon explains why the drag force on flexible structures does not increase with the square of the fluid velocity, as it would for a rigid structure.

The relative error between the two solutions is defined by

$$\epsilon_{\mathbf{x}} = \frac{\|\mathbf{x}_{model} - \mathbf{x}_{ref}\|_2}{\|\mathbf{x}_{ref}\|_2} \tag{5.3}$$

where $\mathbf{x}$ is a vector of values.

With 20 frame elements, we find a relative error of $\epsilon_{\mathcal{R}} = 0.53\%$.

---

[1] https ://github.com/lm2-poly/Reconfiguration-Beam

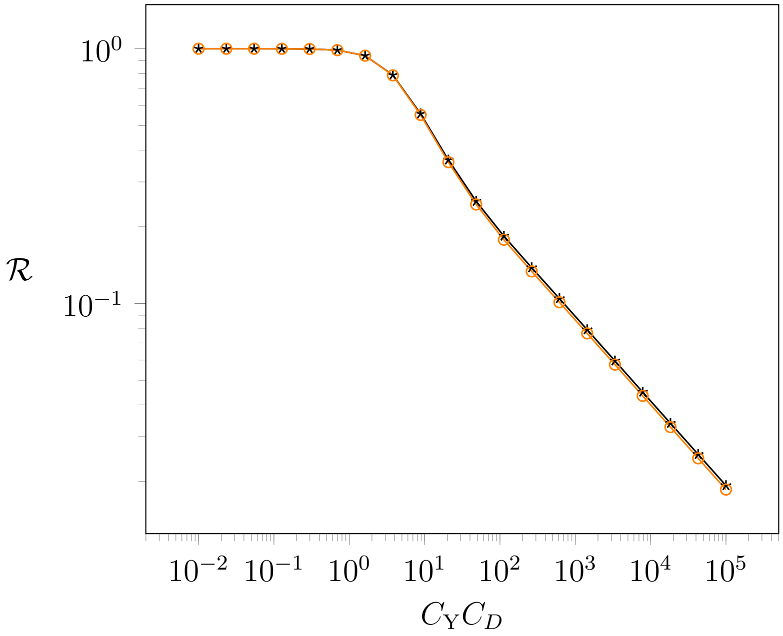

FIGURE 5.1 Reconfiguration number evolution with the Cauchy number for a flexible cylinder bending under uniform fluid load from the present model (─★─) and reference solution (─○─)

5.2 Example 2: Added mass validation

In this example we aim to validate the added mass implementation by comparing the simulated tip displacements to a reference solution.

We consider a rigid bar pendulum initially deviated from its equilibrium position by an angle $\theta_0 = 5°$ and released with no initial velocity in a still fluid, as displayed on Fig. 5.2. The only force considered here is the weight of the cylinder. To simplify the analytical solution, we neglect the effects of drag and lift forces. As a result, the motion of the cylinder experiences no hydrodynamic damping, and we expect sustained oscillations in its motion. The confinement effect from the container walls is neglected.

The analytical solution is derived from the kinetic momentum conservation :

$$(J_{\Delta s} + J_{\Delta a})\,\ddot{\theta} + m_s g \frac{\ell}{2} \sin\theta = 0, \tag{5.4}$$

with $J^s_{\Delta,O}$, $J^f_{\Delta,O}$ being the moment of inertia at point O relative to the axis of rotation Δ from the solid mass and fluid added mass, respectively, and m_s the solid mass. $\theta(t)$ is the angle of the pendulum from its equilibrium position at instant t and g is the gravitational acceleration.

With the hypothesis of small oscillations, $\sin\theta \sim \theta$:

$$\ddot{\theta}(t) + \frac{m_s g \ell/2}{J_{\Delta s} + J_{\Delta a}} \theta(t) = 0, \tag{5.5}$$

leading to the analytical solution

$$\theta(t) = \theta_0 \cos\left(2\pi t/T\right), \tag{5.6}$$

$$T = 2\pi\sqrt{\frac{J_{\Delta s} + J_{\Delta a}}{m_s g \ell}}. \tag{5.7}$$

At the center of gravity of a cylinder, the moment of inertia through a perpendicular axis is:

$$J^{s,f}_{\Delta,G} = m_{s,f}\left(\frac{1}{4}\left(d/2\right)^2 + \ell^2/12\right). \tag{5.8}$$

According to the theorem of parallel axes, the moment of inertia $J_{\Delta,O}$ about a parallel axis

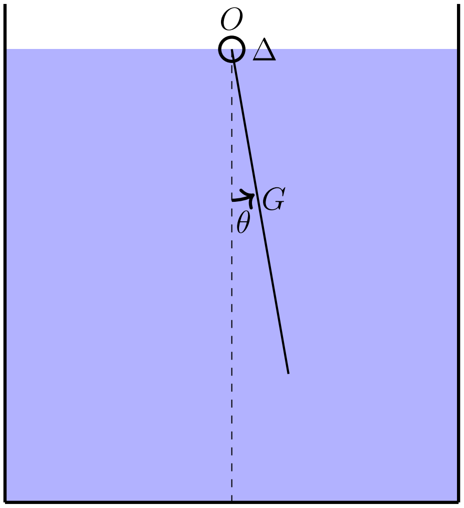

FIGURE 5.2 Sketch of the immersed bar pendulum

at a distance $OG = \ell/2$ from the center of gravity is

$$J^{s,f}_{\Delta,O} = J^{s,f}_{\Delta,G} + m_{s,f}\left(\frac{\ell}{2}\right)^2, \tag{5.9}$$

$$J^{s,f}_{\Delta,O} = m_{s,f}\left(\frac{1}{4}\left(\frac{d}{2}\right)^2 + \frac{\ell^2}{12} + \left(\frac{\ell}{2}\right)^2\right), \tag{5.10}$$

$$J^{s,f}_{\Delta,O} = m_{s,f}\left(\frac{d^2}{16} + \frac{\ell^2}{3}\right). \tag{5.11}$$

$$\tag{5.12}$$

Hence

$$J_{\Delta s} + J_{\Delta a} = (m_s + m_f)\left(\frac{d^2}{16} + \frac{\ell^2}{3}\right). \tag{5.13}$$

Finally we get the oscillation period :

$$T = 2\pi\sqrt{\frac{(m_s + m_f)\left(\frac{d^2}{16} + \frac{\ell^2}{3}\right)}{m_s g\ell/2}}, \tag{5.14}$$

$$T = 2\pi\sqrt{\left(1 + \frac{1}{\mathcal{M}}\right)\frac{1}{g}\left(\frac{d^2}{8\ell} + \frac{2\ell}{3}\right)}. \tag{5.15}$$

$$\tag{5.16}$$

Fig. 5.3 shows a simulation on 3 periods with 1 beam element and $dt = 0.005$ s. The angle displacements closely follows the oscillations provided by the theoretical model. The relative error computed using Eq. (5.3) is $\epsilon_\theta = 0.32\%$.

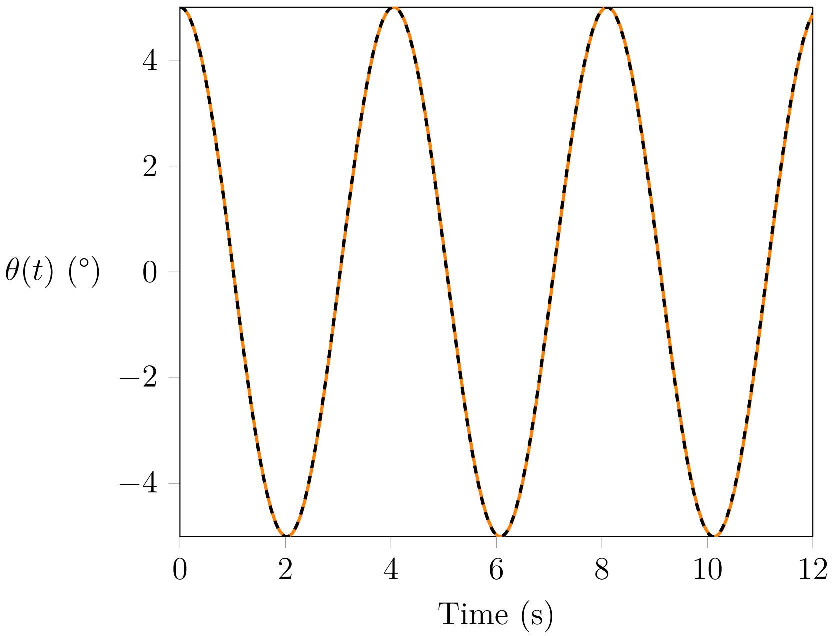

FIGURE 5.3 Time evolution of the pendulum angle from the present model (- - -) and reference solution (—)

5.3 Example 3: In-line and cross-flow VIV verification in small displacements

This example verifies the implementation of the in-line and cross-flow VIV on a single linear beam element with a semi-analytical solution.

The problem consists in a cantilever beam submitted to a transverse flow with a uniform and steady velocity $U\mathbf{e}_{\mathrm{x}}$ as illustrated in Fig. 5.4. The material has a Young modulus of E and a density ρ. The structure has a linear elastic behavior for the internal forces and a lumped mass formulation for the inertial terms. Additionally, we consider small displacements and no structural damping.

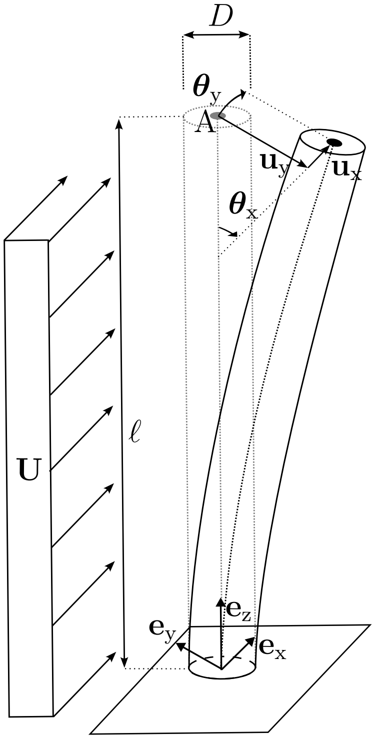

Figure 5.4 3D view of the cantilever beam with small displacements

We only consider the transverse displacement in the yz-plane. The fluid has constant velocity U and exerts oscillating drag and lift forces. The parameter values are presented in Tab. 5.1.

Consider the distributed nonlinear drag and lift loads:

$$\mathbf{b}_d\left(p, \dot{u}_y, \dot{u}_y\right) = b_d\left(p, \dot{u}_y, \dot{u}_y\right)\mathbf{e}_{\mathrm{x}} = \frac{1}{2}\left(C_0^D + \frac{pC_i^D}{2}\right)\rho_{\mathrm{f}} D U_{\mathrm{rel}}^2, \tag{5.17}$$

$$\mathbf{b}_l\left(q, \dot{u}_x, \dot{u}_y\right) = b_l\left(q, \dot{u}_y, \dot{u}_y\right)\mathbf{e}_{\mathrm{y}} = \frac{1}{2}\frac{qC_0^L}{2}\rho_{\mathrm{f}} D U_{\mathrm{rel}}^2, \tag{5.18}$$

with the relative velocity $U_{\mathrm{rel}}^2 = \left(U^2 - \dot{u}_x/2\right)^2 + \left(\dot{u}_y/2\right)^2$. The nodal velocities are averaged to compute a relative velocity constant along the element. For this specific validation case, the change in load direction is neglected as small displacements are considered. The equivalent nodal forces and moments are given by the principle of virtual work. Considering a single linear Bernoulli beam element with length ℓ the equivalent nodal force and moment at the tip A are $\frac{1}{2}b_d\ell\mathbf{e}_{\mathrm{x}} + \frac{1}{2}b_l\ell\mathbf{e}_{\mathrm{y}}$ and $-\frac{1}{12}b_d\ell^2\mathbf{e}_{\mathrm{x}} + \frac{1}{12}b_l\ell^2\mathbf{e}_{\mathrm{y}}$ respectively (Oñate, 2013). The equation of motion of node A is:

$$\begin{bmatrix} m & 0 & 0 & 0 \\ 0 & 0 & 0 & 0 \\ 0 & 0 & m & 0 \\ 0 & 0 & 0 & 0 \end{bmatrix}\begin{bmatrix} \ddot{u}_y \\ \ddot{\theta}_x \\ \ddot{u}_x \\ \ddot{\theta}_y \end{bmatrix} + \frac{EI}{\ell^3}\begin{bmatrix} 12 & -6\ell & 0 & 0 \\ -6\ell & 4\ell^2 & 0 & 0 \\ 0 & 0 & 12 & 6\ell \\ 0 & 0 & 6\ell & 4\ell^2 \end{bmatrix}\begin{bmatrix} u_y \\ \theta_x \\ u_x \\ \theta_y \end{bmatrix} = \frac{1}{12}\begin{bmatrix} 6b_l\ell \\ -b_l\ell^2 \\ 6b_d\ell \\ b_d\ell^2 \end{bmatrix}, \tag{5.19}$$

where m corresponds to the lumped solid and fluid added mass at the free end:

$$m = \frac{1}{2}\left(m_{\mathrm{s}} + C_a\rho_{\mathrm{f}}\ell\pi\left(\frac{d}{2}\right)^2\right). \tag{5.20}$$

System (5.19) can be simplified to two equations:

$$m\ddot{u}_x + u_x\frac{12EI}{\ell^3} + \left(-\frac{b_d\ell}{8} - u_x\frac{9EI}{\ell^3}\right) = \frac{b_d\ell}{2}, \tag{5.21}$$

$$m\ddot{u}_y + u_y\frac{12EI}{\ell^3} + \left(\frac{b_l\ell}{8} - u_y\frac{9EI}{\ell^3}\right) = \frac{b_l\ell}{2}. \tag{5.22}$$

We set the equivalent stiffness $k_u = 3EI/\ell^3$. The reference system is:

$$\begin{cases} m\ddot{u}_x + k_u u_x = \dfrac{3b_d\ell}{8}, \\ m\ddot{u}_y + k_u u_y = \dfrac{3b_l\ell}{8}, \\ \ddot{p} = -2\epsilon_p\Omega_f^2(p^2-1)\dot{p} - 4\Omega_f^2 p + \dfrac{A_p}{D}\dfrac{\ddot{u}_x}{2}, \\ \ddot{q} = -\epsilon_q\Omega_f(q^2-1)\dot{q} - \Omega_f^2 q + \dfrac{A_q}{D}\dfrac{\ddot{u}_y}{2}. \end{cases} \tag{5.23}$$

This nonlinear reference solution is used to validate the amplitude displacements of the coupled variables (u_x, u_y, p, q). The Matlab function `ode45` using a 4^{th} order Rung-Kutta algorithm solves this nonlinear system.

System (5.23) is solved numerically over 2000 time steps. The relative error computed using Eq. (5.3) for this simulation are displayed in Tab. 5.3.

TABLE 5.3 Relative errors of u_x, u_y, p, q

Error	$\epsilon_{\mathbf{u}_x}$	$\epsilon_{\mathbf{u}_y}$	$\epsilon_{\mathbf{p}}$	$\epsilon_{\mathbf{q}}$
Value	0.29%	0.23%	0.15%	0.000087%

Fig. 5.5 compares temporal evolution of u_x, u_y, p, q from the model with the reference solution over one period T of the motion. The model follows closely the reference solution. The doubled vortex shedding pulsation in the in-line Van der Pol oscillator Eq. (2.5) causes a doubling of frequency of the oscillator p. The present model is in agreement with the reference solution and the relative errors of the four investigated quantities are below 0.3%.

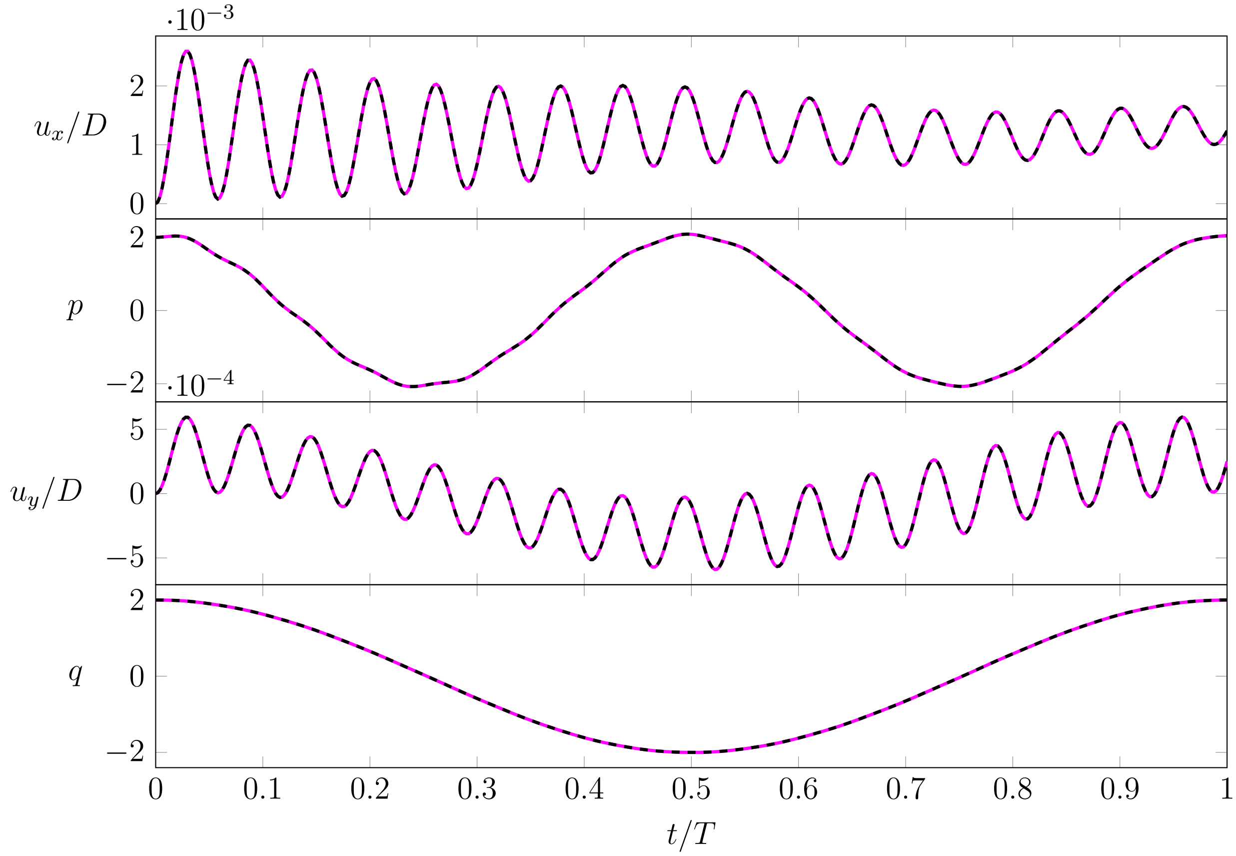

FIGURE 5.5 Verification of the in-line and cross-flow displacements u_x, u_y and wake variables p, q of a cantilever beam in a uniform flow with small displacements. Present model (- - -), Reference solution (—)

5.4 Example 4: Validation of cross-flow VIV with large displacements

This example validates the cross-flow VIV model in large displacements with (Leclercq & de Langre, 2018) wake-oscillator.

A cantilever beam of length ℓ, density ρ and uniform circular cross section with diameter D is clamped at one end. It bends under a transverse uniform and steady flow of velocity $\mathbf{U} = U\mathbf{e}_\mathrm{x}$ and density ρ_f (see Tab. 5.1 for exact values). The beam bends in the xz-plane with large deformation and undergoes cross-flow vibrations along $\mathbf{e}_\mathrm{y}$ as displayed on Fig. 5.4. In this specific validation example, in-line VIV forces are neglected: the drag coefficient takes the constant value $C_D = 2$. The wake-oscillator parameters for cross-flow VIV are $A_q = 12, \epsilon_q = 0.3$ as recommended in Facchinetti et al. (2004a) and used in (Leclercq & de Langre, 2018).

The beam is discretized in 100 elements and the time using 10^6 time steps. The static solution is first computed with increasing reduced velocity. The dynamic problem is then solved using the steady solution as the initial configuration. The analysis considers only the second half of the simulation. This cuts off the transient and allows the vibrational dynamics to build up. The amplitudes are normalized by D and the frequencies by the first structural frequency f_1 obtained by Eq. (5.1). The root mean square amplitudes of the transverse displacement of the cylinder tip is presented in Fig. 5.6. Note that the definition of U_R used in (Leclercq & de Langre, 2018) incorporates the Strouhal number $S_t = 0.2$, resulting in a stretching of the x-axis by a factor of 5. Fig. 5.7(a, b) presents the normalized transverse displacements along the span of the cylinder for the reference and the present model. Both models seem to present the same mode of bending for each reduced velocity.

One noticeable difference are the vertical bands before the transition from mode 3 to mode 4. At the limit of a mode transition, two structural frequencies are excited by the wake and the lock-in can occur on either on or the other mode. That is what happens between $U_R = 75$ and $U_R = 85$: the fourth mode is increasingly excited and for some simulations, the lock-in jumps from the third to the fourth mode, then comes back to the third. Fig. 5.8 compares the frequencies of the transverse displacement of the cylinder tip from the present model and the reference.

For small deflections ($U_R < 150$), the cylinder is excited with single-mode lock-in: the peaks of amplitude at $U_R = 2.8$, $U_R = 18$, $U_R = 56$ and $U_R = 110$ in Fig. 5.6 correspond to the lock-in between the wake frequency and the first, second, third and fourth modes respectively. At those values, only one frequency is excited (Fig. 5.8), except around $U_R = 80$ where the jumps from the third to the fourth mode can be observed. When the deflection is large

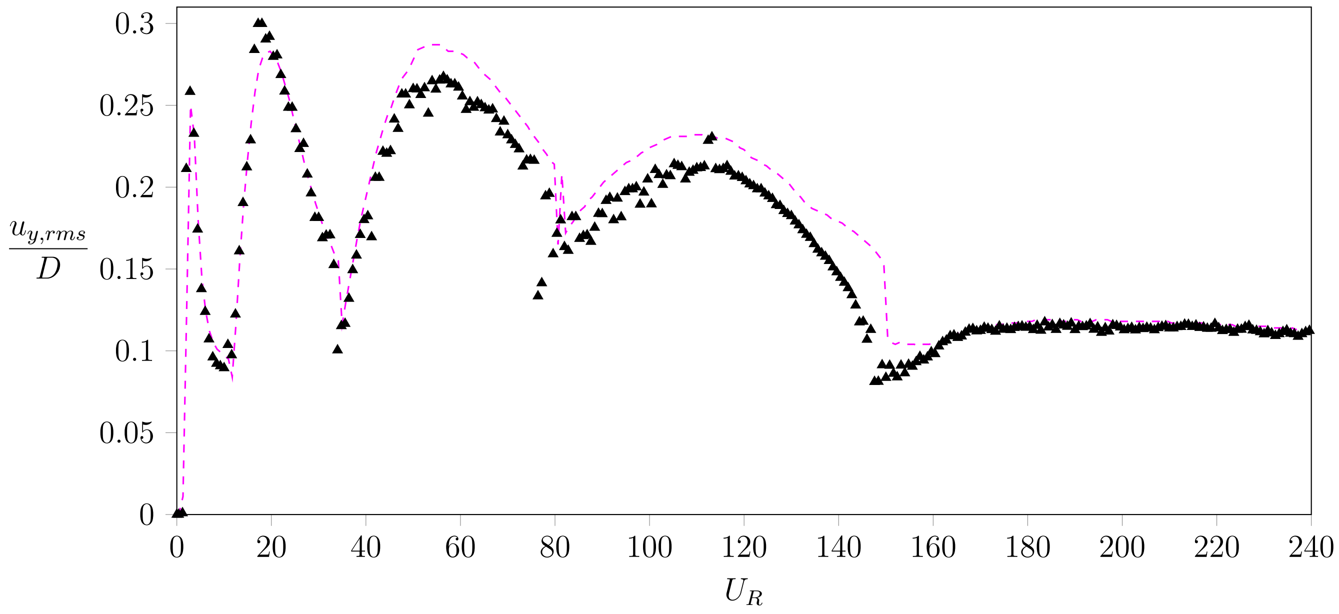

FIGURE 5.6 Cross-flow RMS amplitude of the tip of the cylinder: present model (▲) ; reference data (- - -)

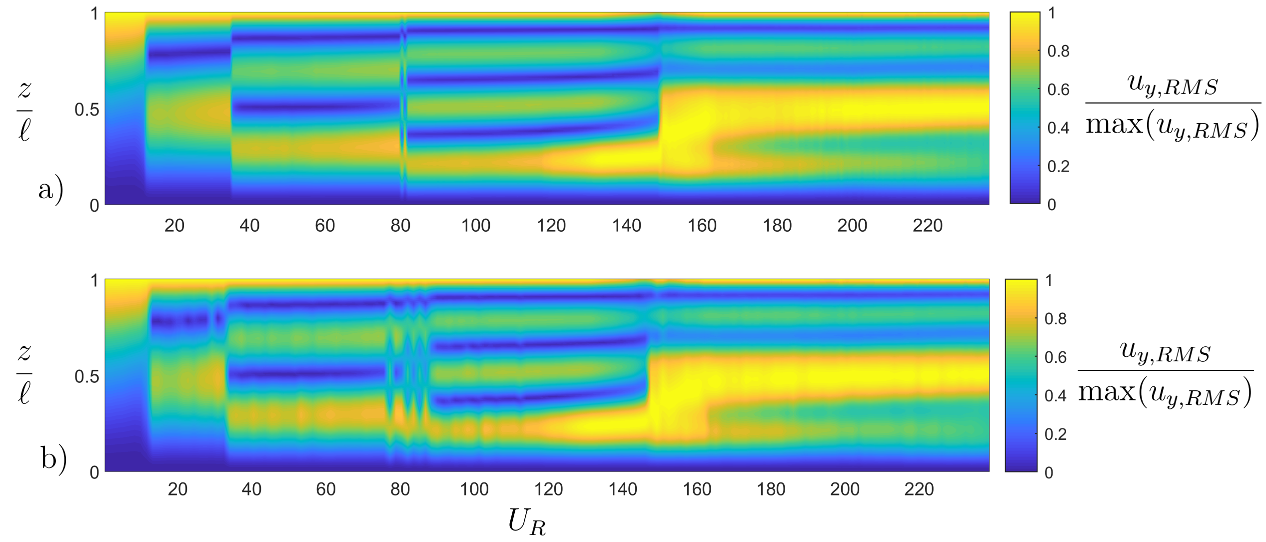

FIGURE 5.7 Tip cross-flow RMS displacements along the span of the cylinder, normalised by the maximum RMS displacement. Result from the reference model (a) is compared with the present model (b)

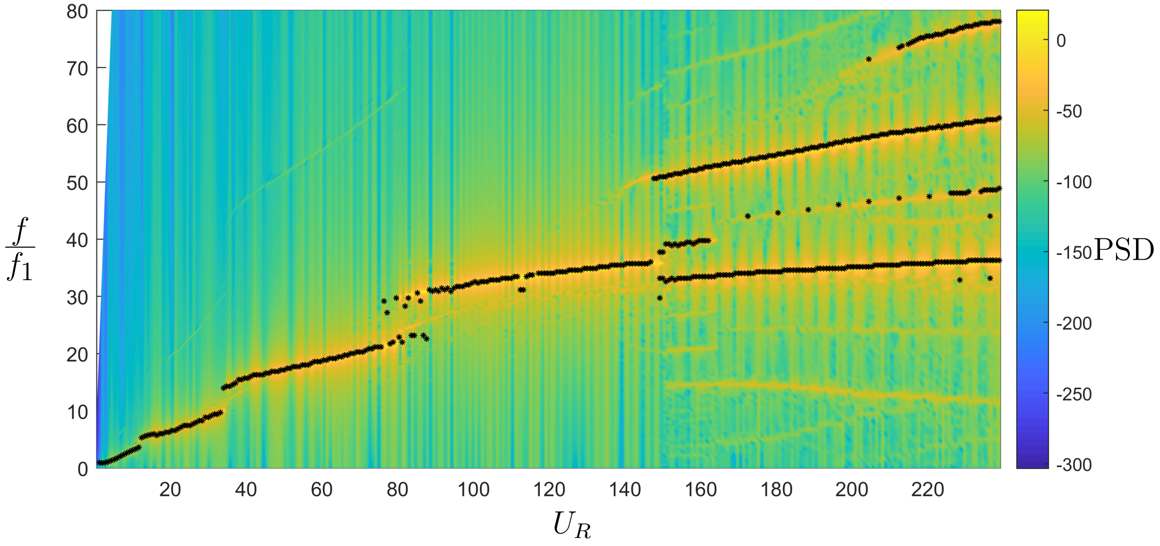

Figure 5.8 Cross-flow displacements of the cylinder tip: dominating frequencies from the present model ($*$) is plotted over the reference spectrogram

enough ($U_R > 150$), the transverse amplitudes reach a lower constant value of 0.1 (Fig. 5.6) and several frequencies are excited at the same time (Fig. 5.8). The variations in the normal flow profile along the span of the structure induces a lower and multi-frequency response compared with uniform flow, as described in (Leclercq & de Langre, 2018).

The present model is capable of reproducing the same amplitudes and frequencies as in (Leclercq & de Langre, 2018) up to reduced velocities as large as $U_R = 240$, validating the cross-flow VIV in large displacements and large rotations.

5.5 Example 5: Validation of in-line VIV and mesh analysis

This example aims to validate the implementation of the in-line and cross-flow wake-oscillator model against experimental results form Trim et al. (2005) and DNS results from Holmes et al. (2006).

We study a cantilever hollow pipe of external diameter $D = 27$ mm and internal diameter $D_{\text{int}} = 21$ mm. It has pinned boundary conditions at both ends. Riser tension is constant, set to $\Theta = 5$ kN (even if experimental measurements show oscillations between 4 kN and 6 kN). The uniform and steady current has a velocity U and flows transverse to the pipe. The other parameters are summarized in Tab. 5.1.

A mesh analysis is performed on this example in order to estimate the number of elements needed to accurately solve both in-line and cross-flow VIV. We compare the numerical displacements $\mathbf{d}_{N_e}(x,t)$ with a reference solution $\mathbf{d}_{ref}(x,t)$ over $N_t = 1000$ time steps, equivalent to 20 periods of motion. The comparison is performed for different numbers of elements, $N_e = 1000$ being the reference value. The relative error between the displacement histories is given by:

$$\epsilon_{N_e} = \frac{\int_0^\ell \int_0^{t_f} \|\mathbf{u}_{N_e}(x,t) - \mathbf{u}_{ref}(x,t)\|_1 dtdx}{\int_0^\ell \int_0^{t_f} \|\mathbf{u}_{ref}(x,t)\|_1 dtdx}. \tag{5.24}$$

Fig. 5.9 displays the evolution of the relative error with N_e. The error is inversely proportional to the square of the number of elements: $\epsilon_{N_e} \sim 1/N_e^2$. In this example, $N_e = 100$ is enough to have an error $\epsilon_{N_e} < 10^{-3}$.

Numerical results are presented with the reference solution $N_e = 1000$ in Fig. 5.10. The first half of the simulation is ignored in the analysis to cut out the transient. RMS values of both cross-flow and in-line displacements along the span are compared to experimental results from Trim et al. (2005) as well as DNS simulation from Holmes et al. (2006). The fifth mode emerges as the dominant in-line mode in both the model and experimental data, while the third mode remains the dominant cross-flow mode in all the presented data. The symmetry of the problem about the pipe midpoint leads to a symmetric response of the pipe. This differs from the richer experimental response, underlying the complexity of the VIV process.

The maximum RMS displacement is predicted with a relative error of 0.4% for in-line and 0.2% for cross-flow compared with the experimental data. This is often a quantity of interest when assessing structural fatigue from VIV (Gao et al., 2015), well estimated by this simple numerical model. We obtain general agreement with the experimental data from Trim et al. (2005).

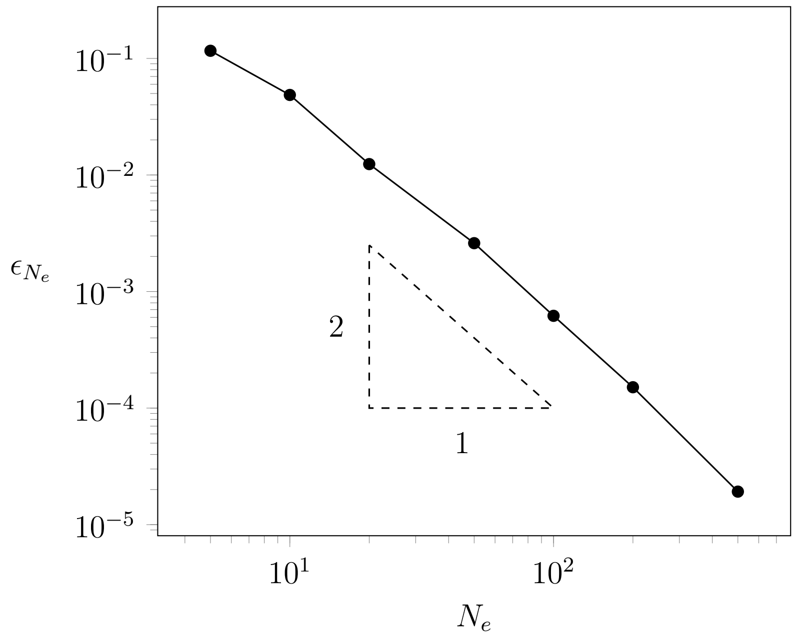

FIGURE 5.9 Mesh analysis with a reference solution of 1000 elements (—●—)

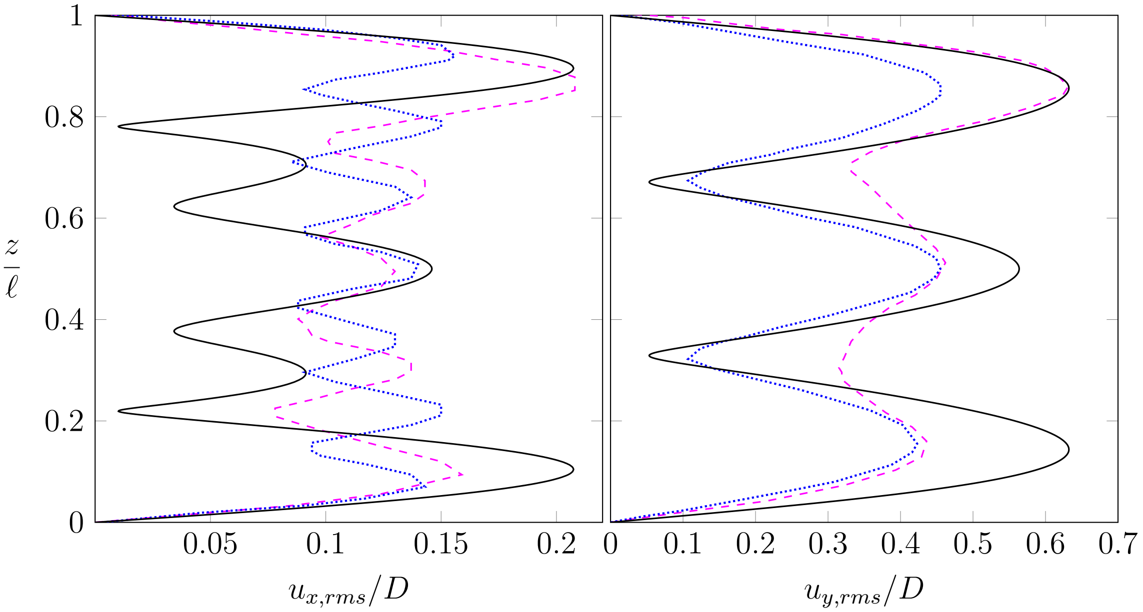

FIGURE 5.10 In-line and cross-flow RMS displacements along the pipe. Present model (——), experimental data (- - -), DNS data (·······)

5.6 Experimental validation

This example compares the model with lab experimental data obtained following the experimental methodology described in chapter 4. A cylinder is submitted to a transverse flow with a constant and uniform velocity U with clamped and free ends. The simulation and experimental parameters are displayed in Tab. 5.1. The cylinder has a length ℓ, diameter D and bending stiffness EI. Unlike previous examples, the mass ratio is lower than $1 : \mathcal{M} = 0.79$. To account for the Reynolds number effect on the drag, the constant drag coefficient C_D^0 follows the empirical model for a circular cross section from Cheng (2013):

$$C_D^0(R_\mathrm{e}) = 11R_\mathrm{e}^{-0.75} + 0.9\left(1 - e^{-1000/R_\mathrm{e}}\right) + 1.2\left(1 - e^{-(R_\mathrm{e}/4500)^{0.7}}\right). \tag{5.25}$$

Fig. 5.11 plots the cylinder center line in the xz-plane for increasing U_R, providing a visual representation of the deformations.

The experimental data are compared with the numerical results. Fig. 5.12 displays the transverse RMS amplitudes of the tip $u_{y,rms}/D$ over the range of interest $U_R = [0, 50]$. During the intermediate flow regimes between the two lock-ins, the cylinder experiences very low oscillations, with the experimental RMS amplitude dropping below 0.1 for $U_R \in [8.5, 14.3]$, and after the second lock-in for $U_R > 39$ (Fig. 5.12). In Eq. (5.25), the drag coefficient decreases with the reduced velocity, which might explain the higher amplitudes observed during the second lock-in.

Fig. 5.13 presents the spanwise localization of the RMS transverse amplitudes obtained from simulations for varying reduced velocities. The transverse beam shapes are plotted for two different flow velocities: $U_R = 4.5$ and $U_R = 18$. In the first lock-in, the vibration is dominated by the first mode, while in the second lock-in, mode 2 becomes predominant. The ranges of U_R where the first and second lock-in occur in the simulation are coloured with pink and purple

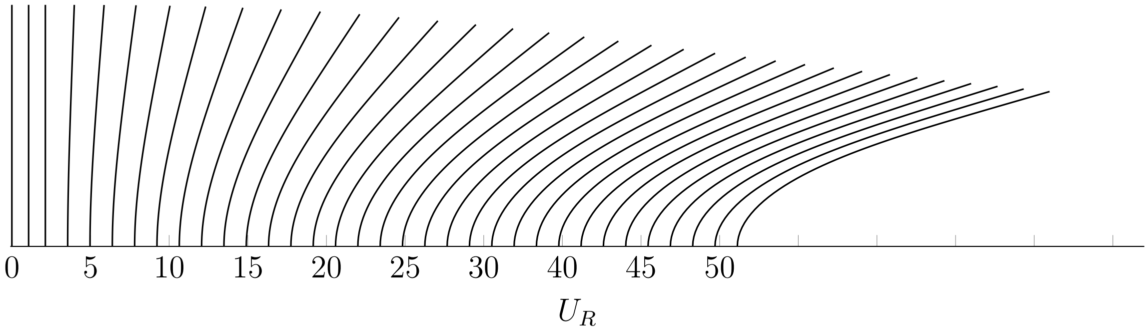

FIGURE 5.11 Cylinder center line static deflection in xz-plane with increasing U_R

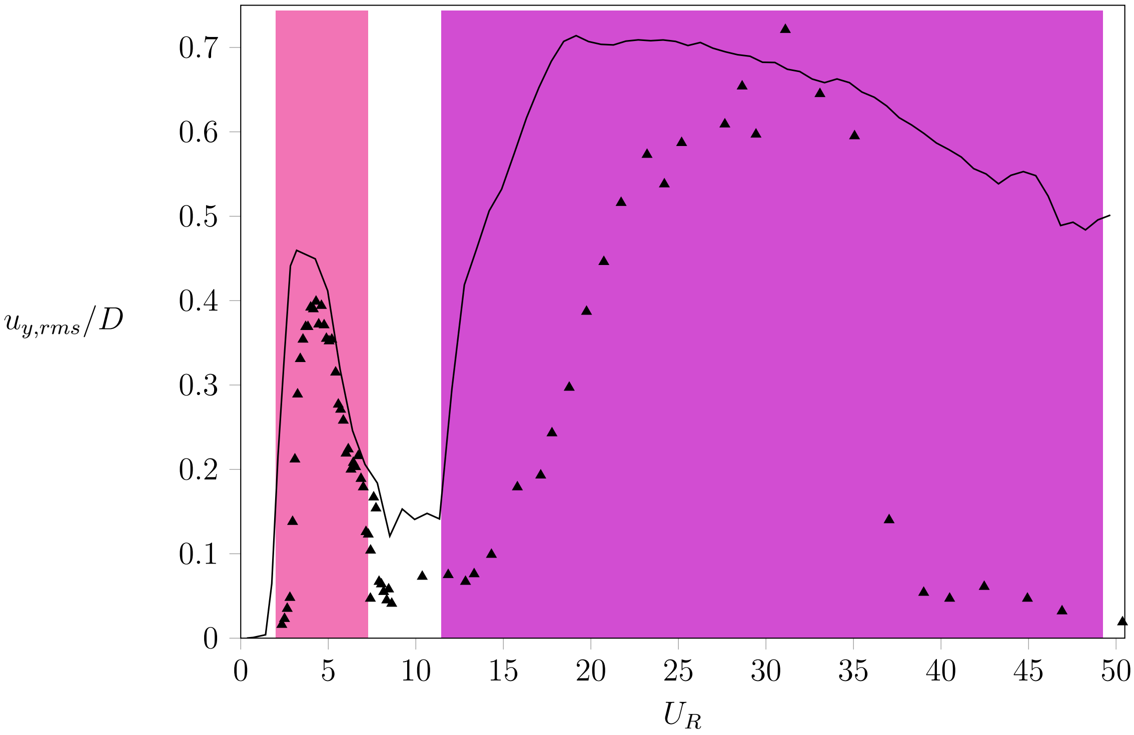

Figure 5.12 Cross-flow RMS displacements of the cylinder tip: present model (——), experimental data (▲). Pink and purple regions represent the mode 1 and 2 lock-in ranges, respectively, where $u_{y,rms} < 0.2D$

rectangles, respectively. First and second lock-ins occur on the range $U_R = [1.7, 7.8]$ and $U_R = [11, 50]$ respectively, with a gap in between the two lock-ins where the cylinder almost doesn't vibrate. Fig. 5.14 displays the frequencies PSD of the tip transverse displacements at different reduced velocities, as obtained from both simulation and experimental data. Fig. 5.14 also displays the vortex shedding frequency $f_w = S_t U/D$ and the three first natural frequencies of the cylinder f_1, f_2, f_3 on horizontal dotted lines, computed with Eq. (5.1). All the frequencies are normalized by $f_1 = 2.7$ Hz.

In Fig. 5.14(a), the main excited frequency in the simulation first follows the vortex shedding frequency. For $U_R > 12$ the frequency strongly locks on f_2. However, the second mode lock-in in the experimental data Fig. 5.14(b) is not that strong and slightly increases. We deduce that the numerical lock-in is stronger than an experimental lock-in.

The decrease in vibration observed experimentally between the two lock-in regions makes the displacements signal very low and noisy. As a result, the Fast Fourier Transform (FFT) algorithm fails to detect any experimental frequency on these ranges, hence the gap observed in Fig. 5.14(b). Both lock-in regions extend on wider U_R ranges and have higher amplitudes compared with results from Fig. 5.12 in Section 5.4. This is a well known effect of reducing the mass ratio, dropping from 1 in Section 5.4 to 0.79 in this example (Vandiver, 1993). The first two lock-in ranges in Fig. 5.14(a) are dominated with a single frequency, while a multi-frequency response appears for $U_R > 45$. This multi-frequency response was observed by Leclercq et de Langre for $U_R > 150$ in Fig. 5.8. In a large deflection case, as the elements are closer to the tip they perceive a decreasing normal flow velocity. Thus, when moving towards the tip, the structure is excited by the wake at a decreasing frequency. This spreading of the wake excitation spectrum during large deformations is thus attributed to the variations in the spanwise profile of the normal free-stream component (Leclercq & de Langre, 2018). This feature is also captured in our model.

The proposed model effectively captures the overall physics of VIV measured experimentally. Figs 5.12, 5.14 demonstrate that the model accurately represents the tip amplitudes, frequencies and the right mode number for the first and second lock-in ranges. The observed decrease in vibration between them is also present. The relative errors on the tip transverse maximum RMS amplitude in Fig. 5.12 for the first and second lock-in ranges are 19.6% and 0.9%, respectively. However the second one is predicted on a wider range of U_R than the experimental data. Note that the WOM empirical parameters could be optimized for this specific study to improve the prediction, but it is beyond the scope of this work.

In order to gain a deeper understanding of the dynamics of branched geometries, it is essential to conduct an analysis of the structural modes. This is the focus of the upcoming chapter,

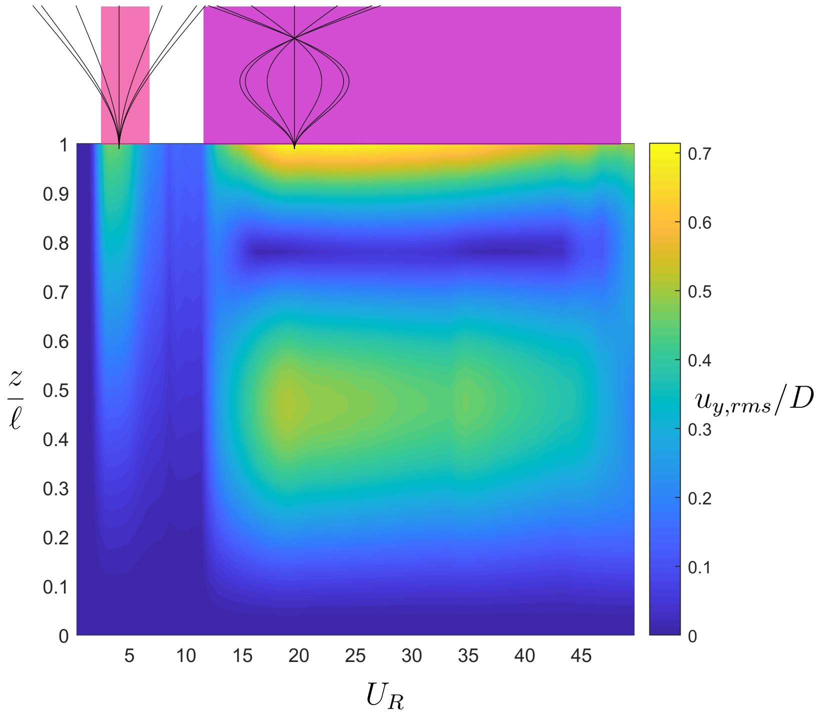

FIGURE 5.13 Spanwise localization of the RMS transverse displacement for varying U_R. Beam shapes transverse displacements (—) appear for $U_R = 4.5$ and $U_R = 18$. Pink and purple regions represent the mode 1 and 2 lock-in ranges, respectively, where $u_{y,rms} < 0.2D$

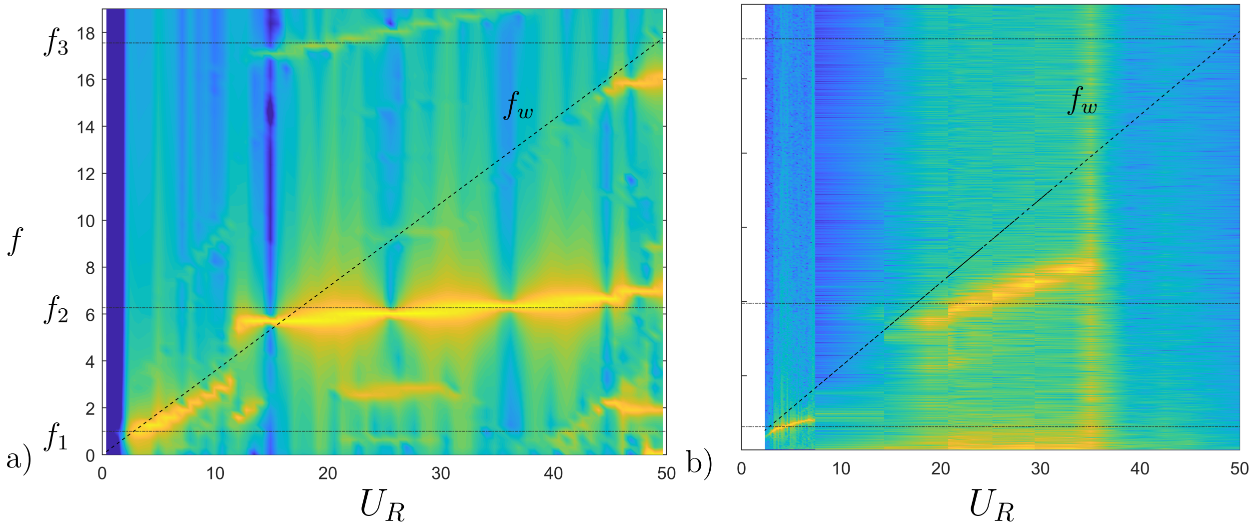

FIGURE 5.14 Spectrograms of the cross-flow displacements of the cylinder tip from the present model (a) and experimental data (b). All frequencies are normalized by f_1

allowing for further insights into the behavior of these complex structures.

CHAPTER 6 RESULTS

This chapter aims to analyse the impact of the number N of pairs of branches parameter on the 3D dynamics of the coral. Each pair of branches is symmetric, forming an angle $\beta = 60°$ with the trunk and has a length $\ell_b = 0.08$ m. Each pair of branch is evenly distributed along the span of the trunk. The simulation parameters are the same as in Example 5 presented in Tab. 5.1.

First, a linear modal analysis is performed on different coral geometries in order to capture the added modes when adding branches. Then, we run simulations on these geometries using the present in-line and cross-flow VIV model. Amplitudes and frequencies are analysed in the light of the computed modes. Finally, the interception model developed in (Boudina et al., 2021) is extended to 3D-structures and the interception gain of the different geometries are analysed.

6.1 Structural modes of branched structures

Linear modal analysis is conducted on the initial configurations of the various geometries. The objective is to calculate the structural modes of the structures, disregarding dissipative terms and forcing terms, in order to gain a deeper understanding of their dynamics. The framework is developed in Appendix B.

When N varies, selecting a single frequency as a universal reference for all instances is not meaningful due to the differing natural frequencies. In addition, normalizing with each structure's natural frequency would complicate the comparison between them, as the same frequency value would shift. Consequently, in this chapter, the frequencies are not normalized and are maintained in their original Hertz representation. Fig. 6.1 presents the first modes shape and frequency for $N = 0, 1, 2, 3$ pairs of branches.

As expected, the 3D modal analysis of a cylinder ($N = 0$) reveals two modes: the first mode in both transverse directions. Fig. 6.1 shows a increasing number of modes below 10 Hz with N : as the number of branch pairs increases from $N = 0$ to $N = 3$, the number of modes below 10 Hz also increases. Specifically, we observe $2, 5, 8$ and 12 modes below 10 Hz for $N = 0, 1, 2$ and 3 pairs of branches, respectively. These added modes can be seen as additional degrees of freedom in the structure when branches are added. The modal analysis allows us to understand which new modes are introduced by a new pair of branches.

To better visualize the frequency distribution of these modes, Fig. 6.2 plots the modes fre-

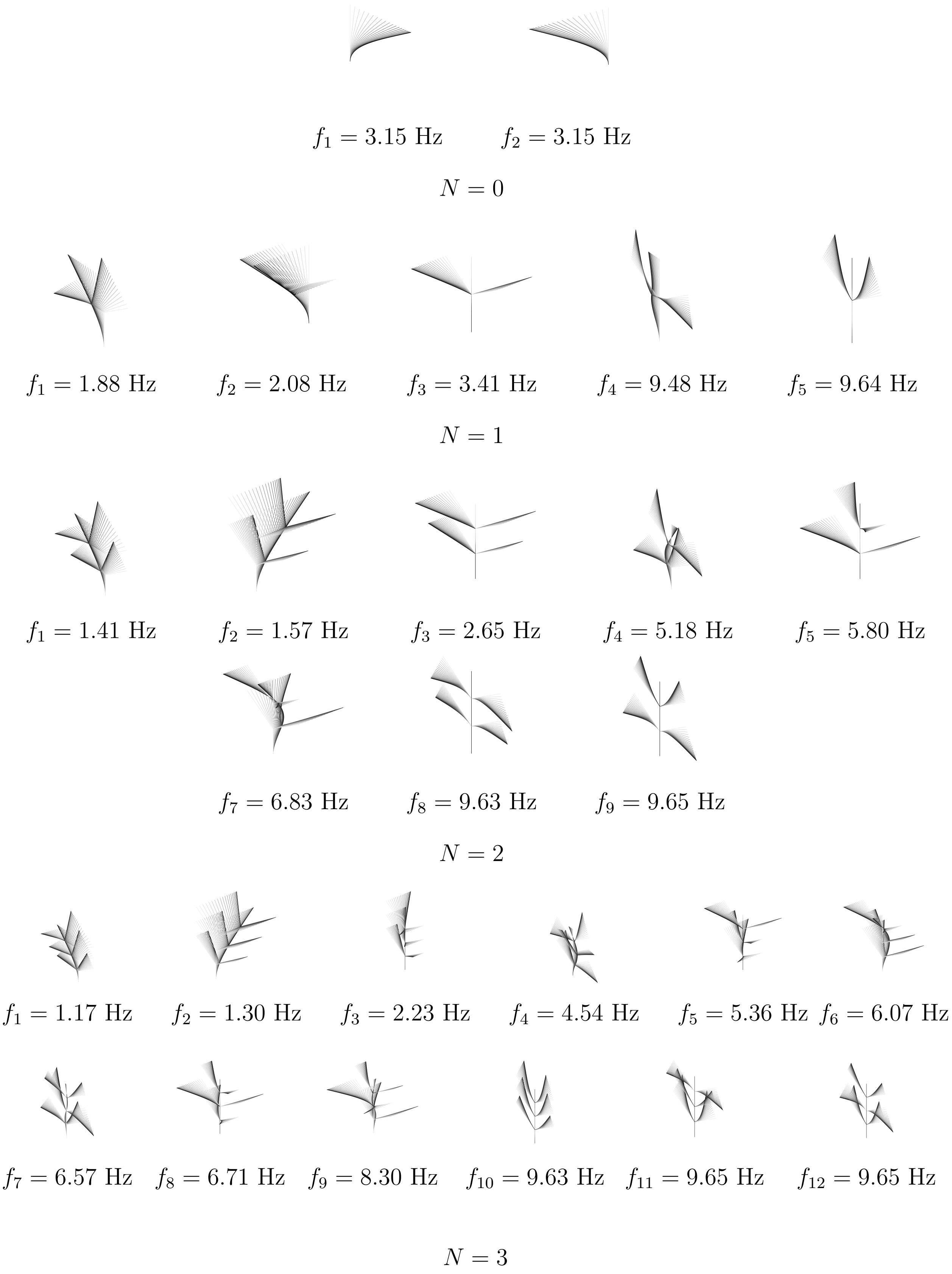

$f_1 = 3.15$ Hz $f_2 = 3.15$ Hz

$N = 0$

$f_1 = 1.88$ Hz $f_2 = 2.08$ Hz $f_3 = 3.41$ Hz $f_4 = 9.48$ Hz $f_5 = 9.64$ Hz

$N = 1$

$f_1 = 1.41$ Hz $f_2 = 1.57$ Hz $f_3 = 2.65$ Hz $f_4 = 5.18$ Hz $f_5 = 5.80$ Hz

$f_7 = 6.83$ Hz $f_8 = 9.63$ Hz $f_9 = 9.65$ Hz

$N = 2$

$f_1 = 1.17$ Hz $f_2 = 1.30$ Hz $f_3 = 2.23$ Hz $f_4 = 4.54$ Hz $f_5 = 5.36$ Hz $f_6 = 6.07$ Hz

$f_7 = 6.57$ Hz $f_8 = 6.71$ Hz $f_9 = 8.30$ Hz $f_{10} = 9.63$ Hz $f_{11} = 9.65$ Hz $f_{12} = 9.65$ Hz

$N = 3$

FIGURE 6.1 Mode shapes from the linear modal analysis of the initial configuration with free-oscillations. Images represent the mode over a quarter of a cycle, with the darker lines at the most deformed position. Modes with frequencies below 10 Hz are plotted for $N = 0, 1, 2, 3$.

quency against the mode number for all modes below 15 Hz and for $N = 0, 1, 2, 3$.

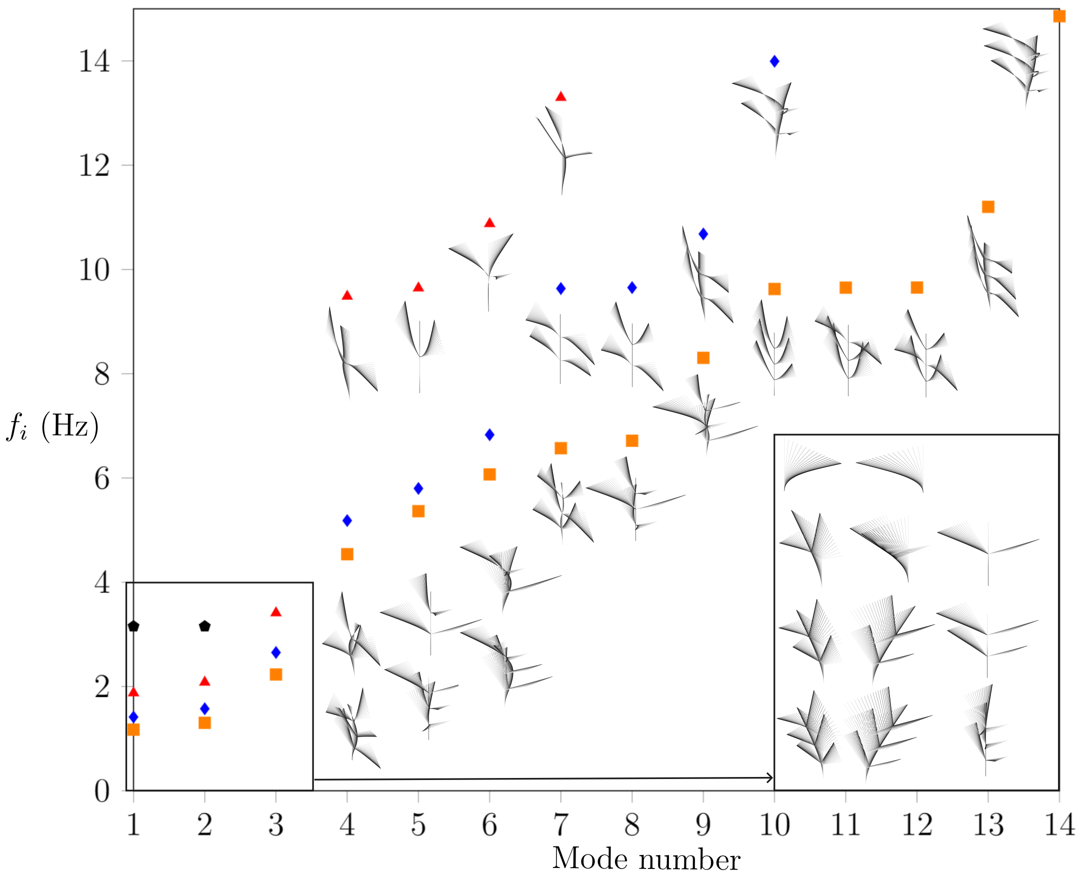

FIGURE 6.2 Mode frequencies of structures with $N = 0$ (⬟), $N = 1$ (▲), $N = 2$ (♦), $N = 3$ (■) pairs of branches

The first two modes exhibit a similar pattern for all N, resembling the first bending mode of the trunk in two different directions. These modal frequencies decrease as N increases, which is expected as the addition of branches introduces additional inertia to the rotational motion. When adding one pair of branches ($N = 1$), four new modes are introduced. The third mode is a rotation in the same direction of the branches around the trunk axis. The fourth and fifth modes are a motion of the two branches in the structure plane in the same direction (anti-symmetric motion) and in the opposite direction (symmetric motion), respectively. The sixth mode is a motion of the trunk and branches in opposite directions. The same four new modes are also found with $N = 2$ (modes number $3, 9, 7$ and 10, respectively) and $N = 3$ (modes number $3, 13, 10$ and 14, respectively). When adding one more pair of branches ($N = 2$), four new modes are again introduced. The fourth mode is an anti-symmetric motion of the two pairs of branches in a different direction for both pairs. The fifth mode is a rotation in the opposite direction of the branches around the trunk axis. The sixth mode combines a bending of the trunk and branches. The eighth mode is a symmetric motion of the two pairs of branches in a different direction for both pairs. The same four new modes are also found with $N = 3$ (modes number $4, 5, 6$ and 11, respectively). In a similar manner, adding one more pair of branches ($N = 3$) introduces 4 new modes (modes number $7, 8, 9, 12$). Note that the seventh mode for $N = 1$ has been excluded from this analysis since its counterpart for $N = 2, 3$ has a frequency above 15 Hz and is not displayed here. We constrained the study to the modes with low frequency, but a similar analysis can be performed for higher frequencies.

To conclude, adding a new pair of branches introduces new degrees of freedom in the structure (4 by pair of branches in this study). The each mode found its counterpart in the higher N, but its frequency may vary.

To visualize the frequency distribution of the structural modes, we present Fig. 6.3, which illustrates the modal frequencies and the associated mode shape below 10 Hz for varying N.

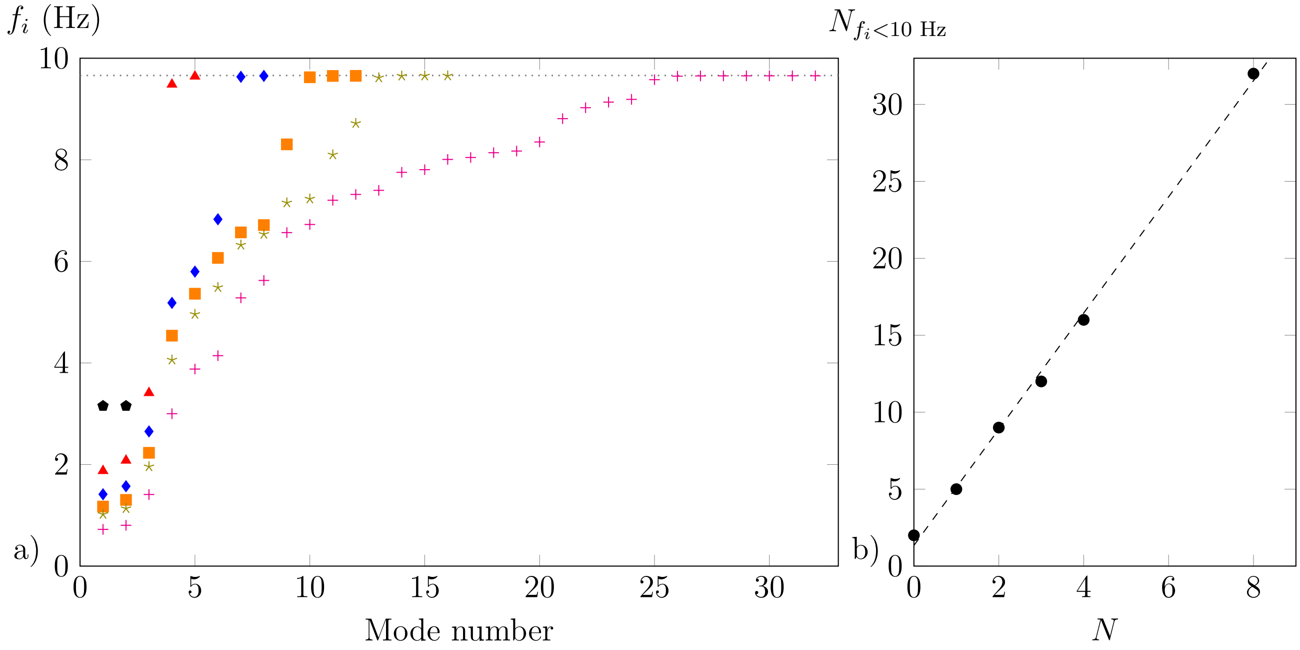

Figure 6.3 Mode frequencies of structures with $N = 0$ (⬟), $N = 1$ (▲), $N = 2$ (♦), $N = 3$ (■), $N = 4$ (⋆), $N = 8$ (+) pairs of branches (a). The fundamental frequency of a clamped-free branch (9.6 Hz) is plotted in dotted line (……). Number of structural modes below 10 Hz for varying number of pairs of branches (b). The dashed line (- - -) is a linear regression ($r^2 = 0.997$): $N_{f_i<10\text{ Hz}} = aN + b$ with $a = 3.78,\ b = 1.34$

Fig. 6.3(a) displays the same modal frequency evolution for $N = 0, 1, 2, 3, 4, 8$. It shows a pronounced concentration of the modal frequencies around the fundamental frequency of a clamped-free branch (9.6 Hz). At this frequency, each pair of branches moves symmetrically inducing no deformation in the trunk. Specifically, the number of modes with this frequency corresponds to the number of branch pairs (0 for $N = 0$, 1 for $N = 1$, and so on). It is consistent with the symmetrical motion of each pair of branches at this frequency: adding one pair of branches adds one degree of freedom to this symmetrical motion. Fig. 6.3(b) shows the evolution of the number of structural modes below 10 Hz $N_{f_i<10\text{ Hz}}$ with N. The linear regression highlights a linear dependency: $N_{f_i<10\text{ Hz}} = 3.78N + 1.34$.

With increasing N, modes increase in number, and their frequency become closer together. However, some ranges of frequency stay less dense even at high N. The additional mode frequencies do not distribute uniformly on the frequency spectrum. They seem to appear more often above 5 Hz than below. Thus, some frequency gaps remain, the largest being between the third and fourth mode for all N. Eventually, as N increases, a greater continuity appears in the distribution of modal frequencies, except for the empty spot around the fourth mode where the density does not increase. We expect from these non uniformity in the added mode frequencies to impact the VIV response of branched structures.

In their modal analysis of a pine tree, which shares the same monopodial branch architecture as our model, Rodriguez et al. (2008) also observed frequency groups that are separated by small gaps. The first group encompasses the first bending modes of the trunk and is distinctly separated from the modes exhibiting deformation in the branches (second group) by a narrow frequency gap. Their second group modes do not distribute evenly in the frequency spectrum, in accordance with our observations. However, when conducting the same modal analysis on another tree architecture, the frequency distribution inside the second group appears more continuous, implying that the modal analysis is sensitive to the specific tree geometry being considered.

6.2 Coral with two branches

Here we consider the planar structure of an idealised coral colony placed perpendicular to the flow and the flow velocity is increased by steps. For $N = 0$, we study the tip of the trunk cross-flow displacements. For $N > 0$ when branches are added, we chose to study the tip of the upper right branch, i.e. the closest branch to the tip of the trunk, on the right side. Fig. 6.4 displays the problem geometry.

The in-line displacement at all nodes is u_x. We define the transverse displacements of the

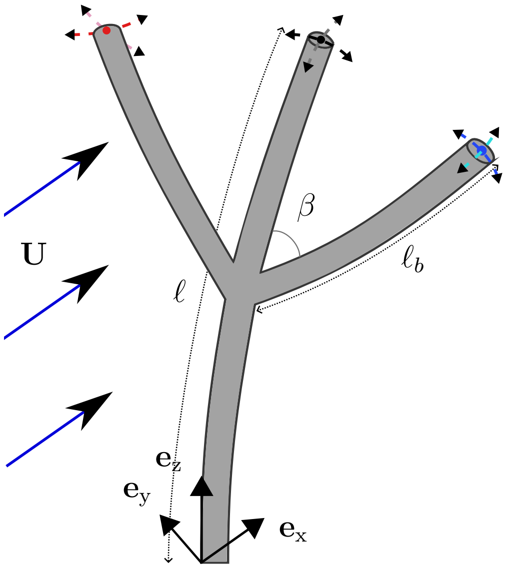

Figure 6.4 Coral geometry with two branches. Arrows at the tips indicate for each branch the in-line direction (lighter color) and cross-flow direction (darker color)

nodes located at the tips of the trunk, the right and left branches respectively as :

$$u_t^{\text{trunk}} = u_y, \tag{6.1}$$

$$u_t^{\text{b1}} = \cos(\beta)u_y - \sin(\beta)u_z, \tag{6.2}$$

$$u_t^{\text{b2}} = \cos(\beta)u_y + \sin(\beta)u_z. \tag{6.3}$$

We keep the definition of the reduced velocity: $U_R = U\ell^2 D^{-1}(m_\text{s} + m_\text{a})^{1/2}(EI)^{-1/2}$ using the initial height of the structure ℓ. The mass of the added branches is included in the structural mass m_s.

6.2.1 Comparison with experimental data

This example compares the present model with our experimental measurement using the $N = 1$ geometry (Fig. 6.4). The materials and method are the same as in Section 5.6. The reduced velocity range of interest is kept to $U_R = 50$ for the simulations. However, the experimental data are presented up to $U_R = 26$. At higher velocities, the structural deformation causes the tip of the trunk to align almost parallel to the flow direction, making it challenging to detect using post-processing techniques. Moreover, we were unable to extract the tip of the branches displacements from the movie frames because the vertical green bands from the test section overlap with the end of the branches, as shown in Fig. 4.4(a). A simple threshold is insufficient to isolate the branch contour from the background. Therefore, only the tip of the trunk is analyzed in the experimental study.

Fig. 6.5 displays the coral displacements from the simulation with two points of view over half a period of the motion at chosen reduced velocities: $U_{R,1} = 2.4$, $U_{R,2} = 7.9$, $U_{R,3} = 15.8$, $U_{R,4} = 23.8$, $U_{R,5} = 35.5$, $U_{R,6} = 48.4$. Fig. 6.6 shows the same displacements from GoPro point of view at $U_{R,1} = 2.4$, $U_{R,2} = 7.9$, $U_{R,3} = 15.8$, $U_{R,4} = 23.8$. It provides a qualitative representation of the structure motion at these reduced velocities. At $U_{R,1} = 2.4$, the simulation in Fig. 6.5 predicts an oscillation of the coral where the trunk bends in the first mode and the branches do not have an independent motion, recalling the first structural mode in Fig. 6.1. This first mode is observed experimentally in Fig. 6.6. The second vibration mode predicted at $U_{R,2} = 7.9$ in Fig. 6.5, however, is not observed experimentally. At this reduced velocity, the coral is almost still. At $U_{R,3} = 15.8$, a combination of the sixth and seventh mode shapes (Fig. 6.1) is observed in both the simulation and the experiments in Figs (6.5, 6.6). They are characterized by an anti-symmetric branches motion and a tip of the trunk oscillation. At $U_{R,4} = 23.8$, the same displacements shape is observed in both the simulation and experimental data.

The cross-flow RMS amplitude from the experimental data and the simulation against U_R are displayed in Fig. 6.7. The present model predicts the two main peaks of amplitude observed at $U_R \sim 2.8$ and $U_R \sim 20$ in the experimental data. However, the model overestimates the maximum RMS displacement for both peaks with a relative error of 68% and 49% respectively. While the experiments show a drastic decrease in vibrations between the two peaks at $U_R \in [5 - 12]$, the model predicts a local maximum in the amplitudes.

To better understand the frequency spectrum present at each reduced velocity, we plot the spectrograms in Fig. 6.8(a,b) depicting the PSD of the cross-flow displacements at the trunk tip from the simulation and experiment.

Three lock-in regions appear on the simulation spectrogram in Fig. 6.8(a) at $U_R \sim 3, 10, 20$. In the experimental spectrogram Fig. 6.8(b), only two lock-in regions occur at $U_R \sim 3, 20$. These lock-ins correspond to the local maxima of amplitude in Fig. 6.7, highlighting the addition of a lock-in at $U_R \sim 10$ in the simulation that is absent in the experimental data. Similar to the previous example, the simulation spectrogram shows a strong lock-in on the fourth mode, where the excited frequency consistently locks onto the same frequency within the entire lock-in range. In contrast, the experimental spectrogram reveals that the second lock-in region closely follows the vortex-shedding frequency, deviating from the model's prediction.

Eventually, the model successfully predicts the two main lock-in regions within the appropriate ranges of reduced velocities. A qualitative analysis of simulation and experiments

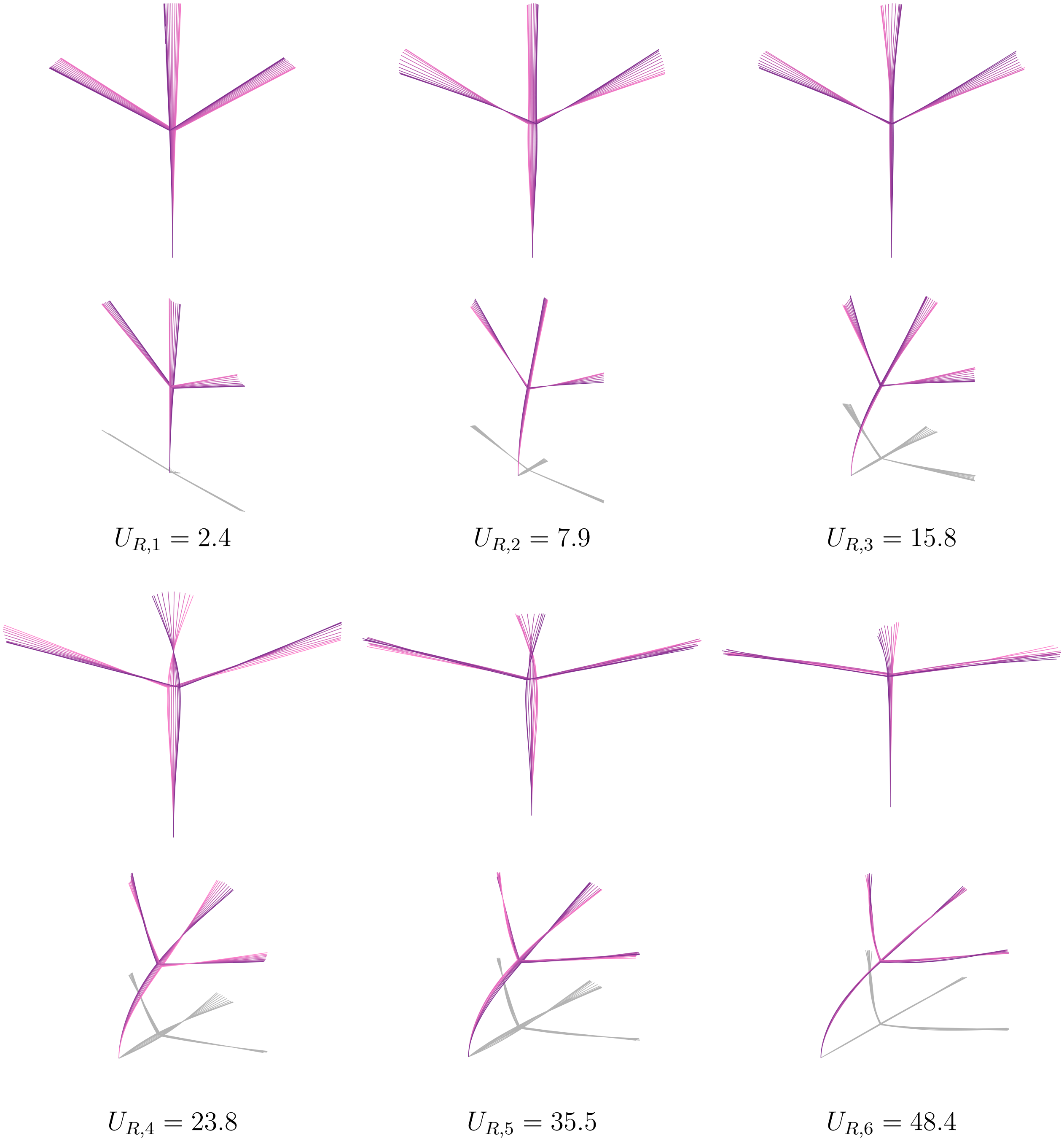

$U_{R,1} = 2.4$

$U_{R,2} = 7.9$

$U_{R,3} = 15.8$

$U_{R,4} = 23.8$

$U_{R,5} = 35.5$

$U_{R,6} = 48.4$

FIGURE 6.5 Shape of the structure motion during half a limit cycle observed at the end of the simulation for different reduced velocities. For each reduced velocity, a projection in the yz-plane is shown above an isometric view which points towards the vector [-1 -1 1]

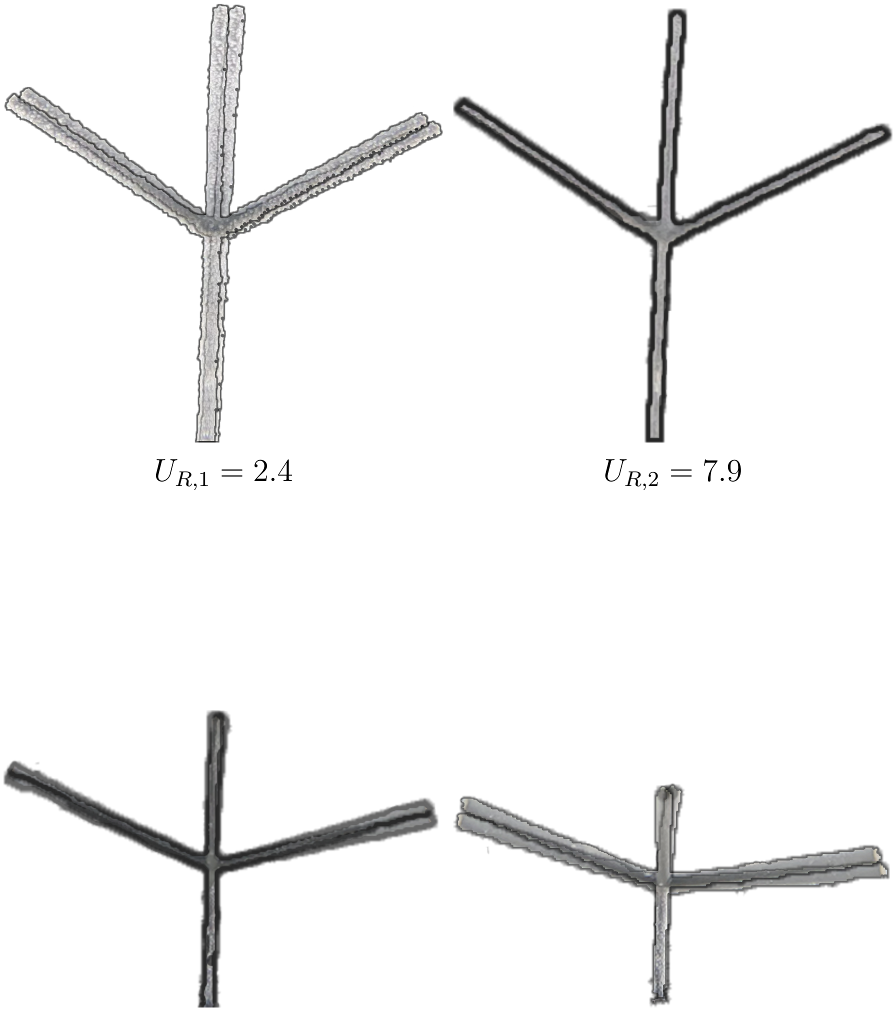

$U_{R,1} = 2.4$

$U_{R,2} = 7.9$

$U_{R,3} = 15.8$

$U_{R,4} = 23.8$

Figure 6.6 Experimental snapshots of the structure motion photographed by the camera inside the test section and pointing upstream for different reduced velocities. The opacity is set to 60% and the borders are darkened

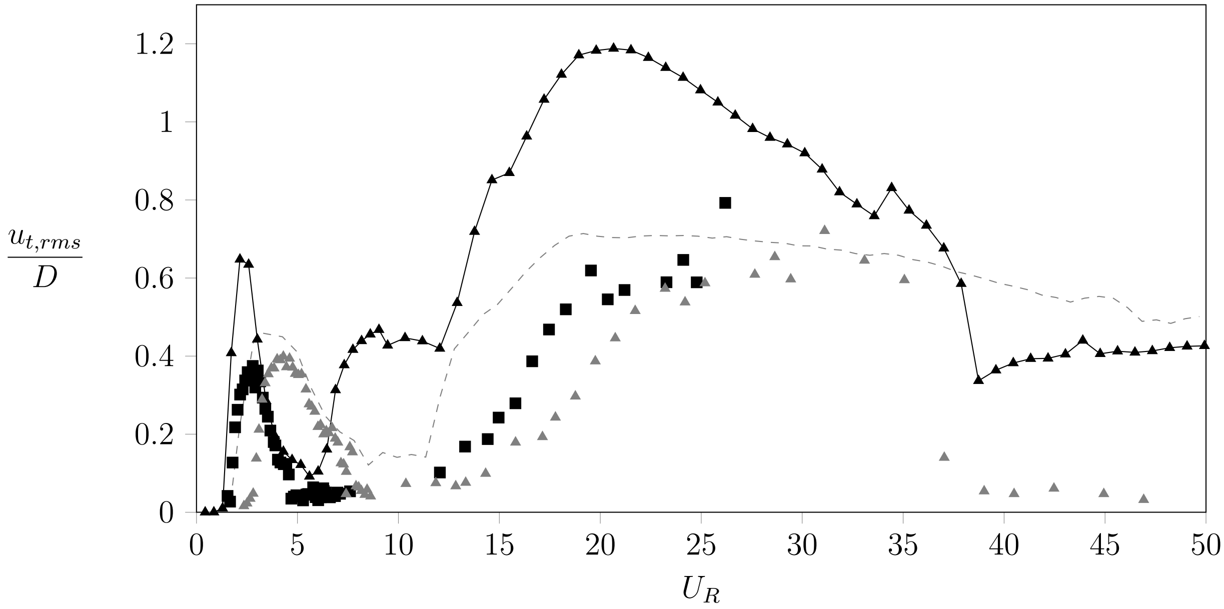

FIGURE 6.7 Cross-flow RMS displacements of the trunk tips from experimental data (■), from simulations (—▲—) and from the cylinder experimental data (▲) and simulation (- - -) in the previous example

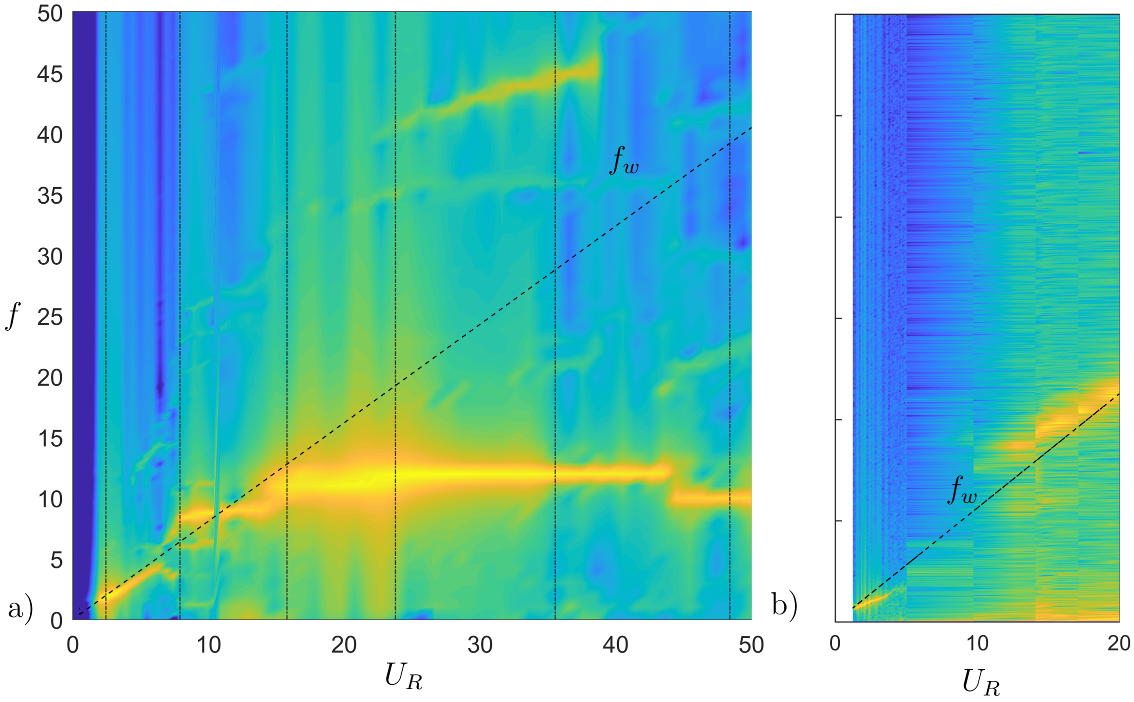

FIGURE 6.8 Spectrograms of the cross-flow displacements at the tip of the trunk from the present model (a) and experimental data (b). Vertical lines (—·) are plotted for $U_{R,1-6} = 2.4, 7.9, 15.8, 23.8, 35.5, 48.4$, as well as the vortex shedding frequency (· · ·)

snapshots of the structure displacements shows good agreement of the displacement shape between the model and the experimental data. However, the model tends to overestimate the amplitude of vibrations, and there are some vibration modes that are not observed in the experimental data.

6.2.2 Comparison with modal analysis

This analysis focuses on the simulation results and aims to uncover the additional dynamics of VIV introduced by the presence of branches.

The in-line and cross-flow RMS amplitude against U_R are displayed in Fig. 6.9. The plot colors correspond to the color of the arrows in Fig. 6.4. The two branches tip RMS amplitudes are similar, which is relevant with the problem symmetry. The two main peaks of the trunk tip cross-flow amplitude occur at $U_R \sim 2$ and $U_R \sim 20$, just as in the previous example for the cylinder. However, the two peaks are much higher: up to $0.6D$ and $1.2D$. The magnitude of the in-line displacements is comparable to that of the cross-flow displacements within the range $U_R \in [6-9]$. In order to explain these observations, we study the excited frequencies. Fig. 6.10 presents the spectrograms of the right branch tip in-line and cross-flow displacements against U_R. The spectrogram from the left branch (not displayed here) is visually indistinguishable from the right branch.

Adding branches to the straight cylinder increases the number of modes and shrinks the frequency gap between two modes. Here, four modes have a frequency between 9.2 Hz and 11.8 Hz (Fig. 6.2). The concentration of these modes explains the broad frequency response around $f = 10$ Hz. The simulated response is compared with the mode shape of frequency excited at the corresponding reduced velocity. Qualitative similarities are observed between them.

At $U_{R,1} = 1.8$, the trunk undergoes first bending mode oscillations and the branches follow the trunk's motion as a rigid body, matching the first structural mode of frequency $f_1 = 2.3$ Hz. This mode oscillates mainly in the cross-flow direction and appears only in Fig. 6.10(b). This rigid rotation results in similar amplitudes for both the trunk and branches when $U_R < 3$ (Fig. 6.9). The added lift force on the structure from the branches lead to an increase of the maximum RMS amplitude rising from 0.46 for the straight cylinder to 0.58 with the branches. The first plateau on the range $U_R = [6.5 - 13]$ in Fig. 6.10 at 9.6 Hz is caused by the excitation of modes 4 and 5 where the branches are greatly moving. These modes contribute to the in-line motion of the branches, and their lock-in regions result in the high in-line amplitude peak observed in this range of U_R (Fig. 6.9). The next plateau at 11 Hz on the range $U_R = [14-19]$ is the sixth mode lock-in. The seventh mode at 13.4 Hz is excited on

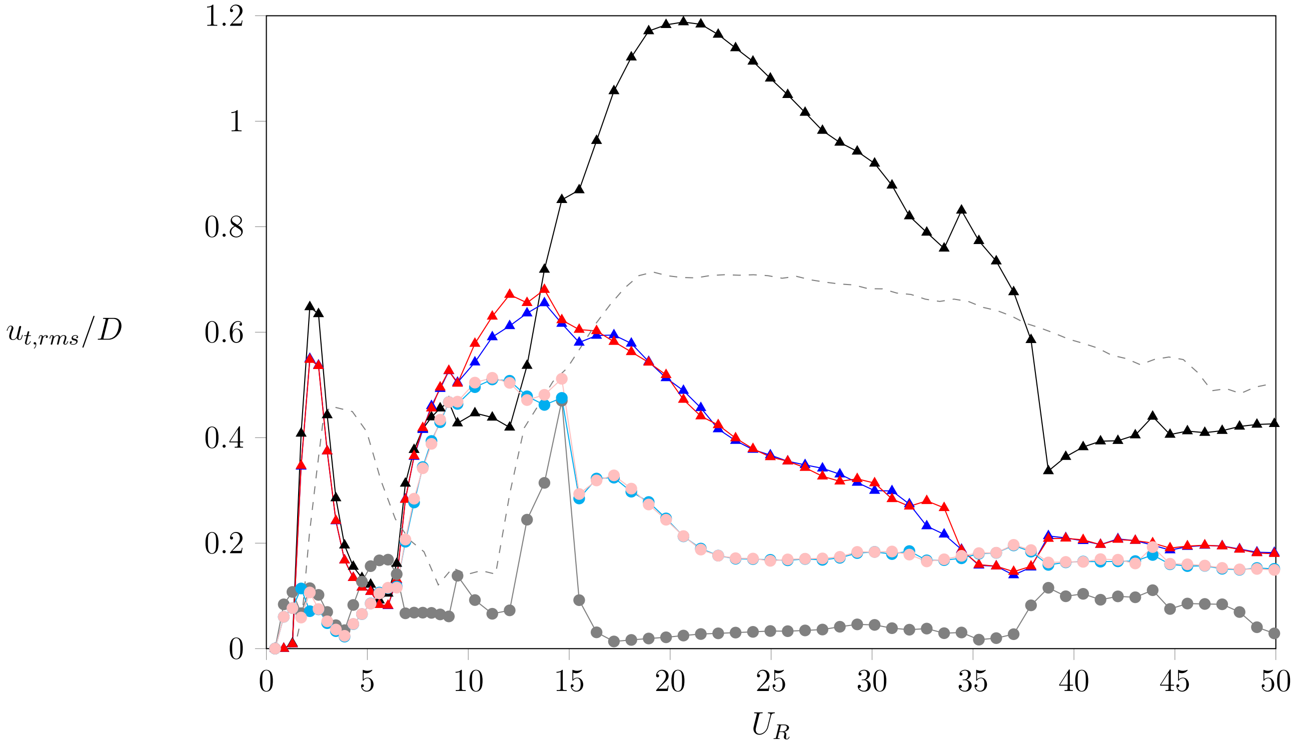

FIGURE 6.9 In-line RMS displacements of the cylinder tips from simulations: trunk tip (—●—), left branch tip (—●—), right branch tip (—●—). Cross-flow RMS displacements of the cylinder tips from simulations: trunk tip (—▲—), left branch tip (—▲—), right branch tip (—▲—), cantilever beam (- - -)

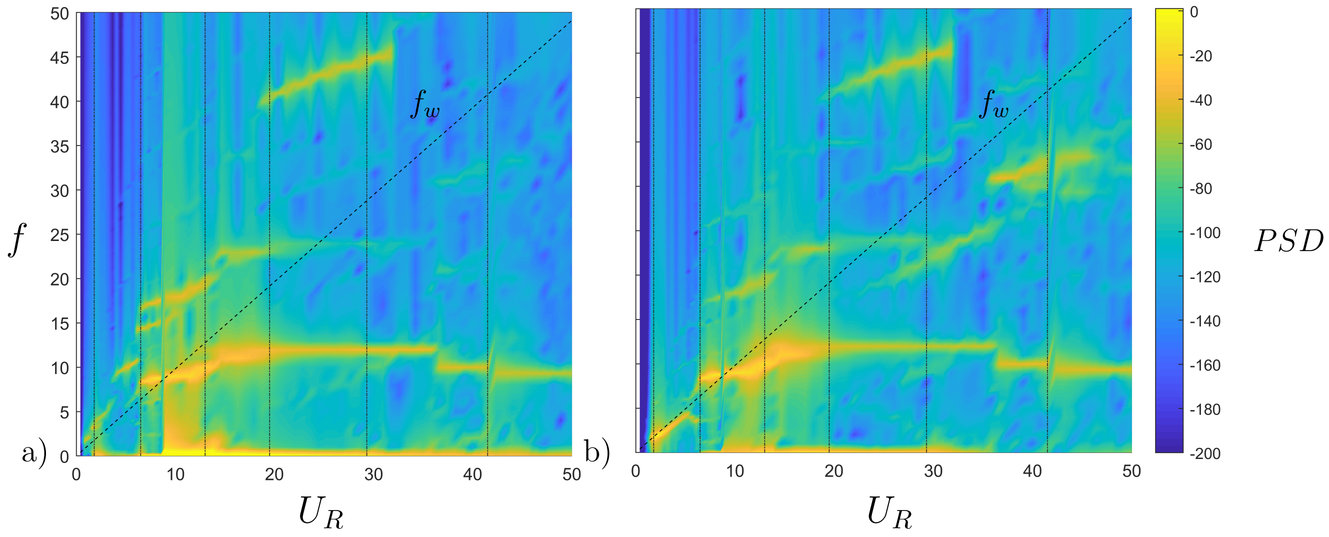

FIGURE 6.10 Spectrogram of the in-line (a) and cross-flow (b) displacements at the tip of the right branch from the simulations. Vertical lines (−·) are plotted for $U_{R,1-10} = 2.0, 6.5, 13, 19.5, 29.3, 39.9$. Frequencies are normalized by the first bending frequency of a cylinder in water f_1

$U_R = [19-35]$. This mode involves mainly a motion of the trunk, hence a stronger excitation at this frequency in the trunk spectrogram (Fig. 6.8).

The maximum RMS amplitude response of the trunk tip reaches 1.2 at $U_{R,4} = 21$. The increase in amplitude observed in the branched cylinder compared to a straight cylinder can be attributed to the added lift force generated by the two branches, which amplifies the swaying of the trunk in mode 7.

All these qualitative features are predicted by high PSD regions in the presented spectrograms. Linear modal analysis is a useful tool for gaining a basic understanding of the complex lock-in phenomena. However, it has its limitations and is not valid for large reduced velocities where the reconfigured structure deviates significantly from the initial configuration.

6.3 Number of branches influence

This section presents and discusses the numerical results of VIV simulations on different coral geometries. The VIV dynamics are analyzed by studying the evolution of amplitude and frequency spectrum with respect to U_R for different values of N. The range of N considered in this study is $[0, 1, 2, 4, 8]$. The range of U_R is reduced to $[0, 34]$.

We define $\mathbf{u}^{\text{branch}}$ the tip of the upper right branch on the structure. Fig. 6.11 presents the in-line and cross-flow RMS displacements of the trunk and this branch tips against U_R.

The in-line amplitudes are about half the cross-flow amplitudes. For $N = 0$, two main peaks of cross-flow amplitude are observed in Fig. 6.11(b). However, as the number of branches is increased to $N = 1, 2, 4, 8$, we count $3, 4, 4$ and 3 local maxima, respectively. This indicates that the number of lock-in regions increases when branches are present, which is consistent with the increase in the number of modes. Yet, adding more branches do not seem to increase the number of amplitude maxima. This is due to the loss of some peaks while N increases. For instance, the cross-flow VIV shown in Fig. 6.11(b,d) exhibits an initial peak at $U_R \sim 2$, which gradually diminishes as N increases and eventually disappears entirely at $N = 8$. Interestingly, the cross-flow vibrations of the trunk tip Fig. 6.11(b) are maximized for $N = 1$. It seems that adding branches inhibits vibrations of the trunk. However, Fig. 6.11(d) shows that the cross-flow amplitudes of the tip of the branch increase with N. For $N > 1$, the cross-flow amplitude of the trunk and branch tips in Fig. 6.11(b,d) seem to converge towards a common peak at $U_R = 6$ with the same amplitude. The lock-in regions occur at closer U_R when N increases. This behavior aligns with the modal frequencies becoming closer together. The reduced velocities at which the lock-in ranges occur do not seem to converge towards one trend for high N. Even the $N = 4$ and $N = 8$ exhibit peaks at different U_R.

To better understand the complex behavior of the branched structure displacements, we compare the frequency spectrum of different geometries. Fig. 6.12 illustrates the PSD of the cross-flow displacements at the tip of the upper right branch, plotted against the reduced velocity, for $N = 0, 1, 2, 4, 8$.

The high PSD regions evolve with U_R in a staircase fashion, where the flat portions exhibit a lock-in on one mode, after which a jump of frequency is observed to the next lock-in. As this figure presents the cross-flow displacements, the frequency spectrum mainly follows the f_w line. Yet, some frequencies are observed along the $2f_w$ line for $U_R > 5$. This is due to our simple definition of the cross-flow direction. Indeed, u_t^{branch} is defined on the straight geometry. While the structure reconfigures, the cross-flow direction at the branch tip slightly changes and the in-line oscillator double frequency starts to appear in the spectrogram.

While increasing the number of branches, the frequency spectrum gets closer to the Strouhal law (Fig. 6.12). This is counter intuitive since by adding branches, the modal response of the structures becomes more complex as more modes are excited. Yet, the frequency response becomes simpler by approaching the linear relation provided by the Strouhal law. Paradoxically, the simple linear Strouhal law applies better when the structure geometry is more complex. This is because by adding structural modes they become closer together in frequency and the lock-in range on each mode is shorter. The closest mode to the vortex shedding frequency is

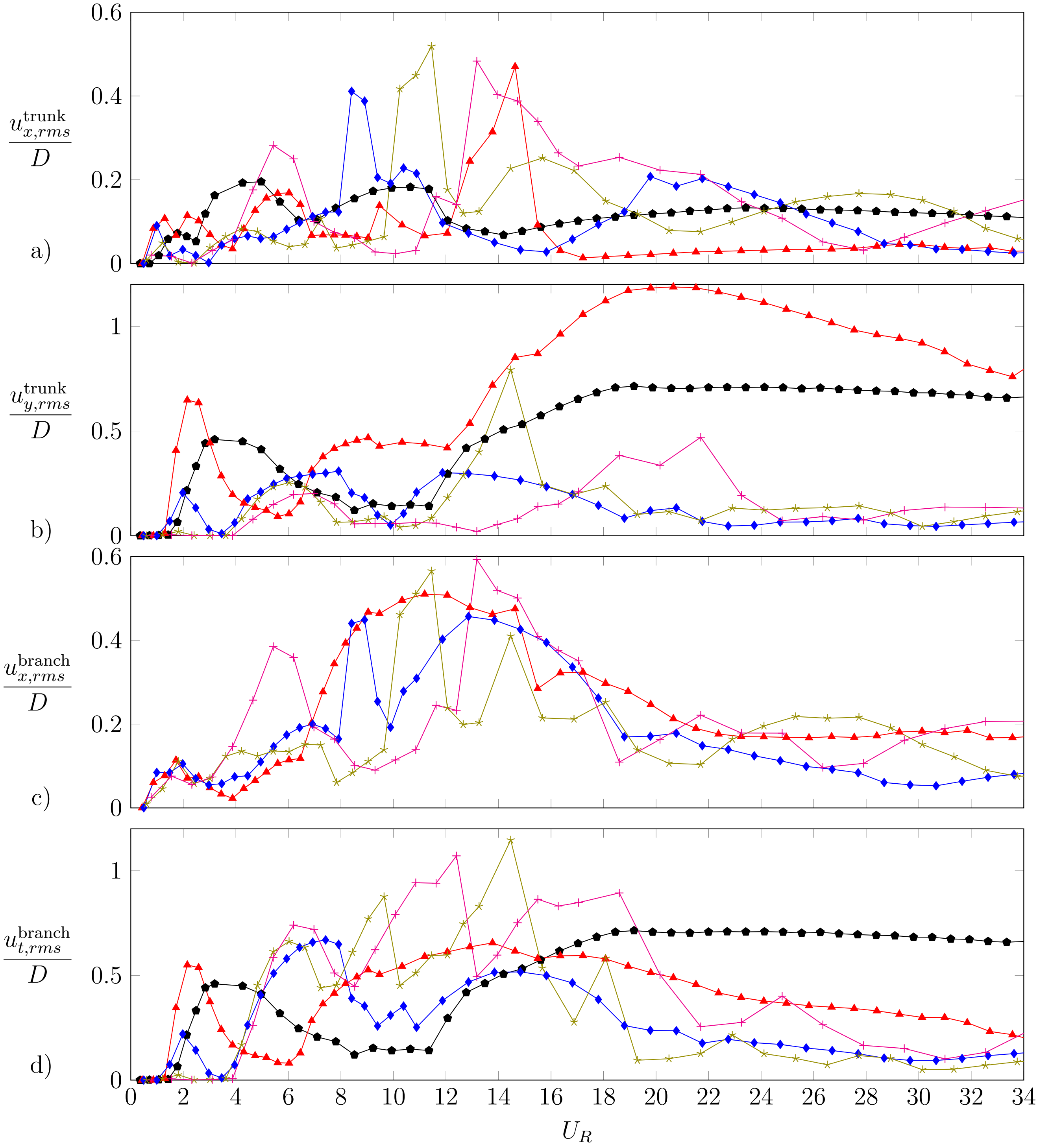

FIGURE 6.11 In-line and cross-flow RMS amplitude of the trunk tip (a and b) and upper right branch tip (c and d) structures with $N = 0$ (—⬟—), $N = 1$ (—▲—), $N = 2$ (—◆—), $N = 4$ (—✶—), $N = 8$ (—+—) pairs of branches

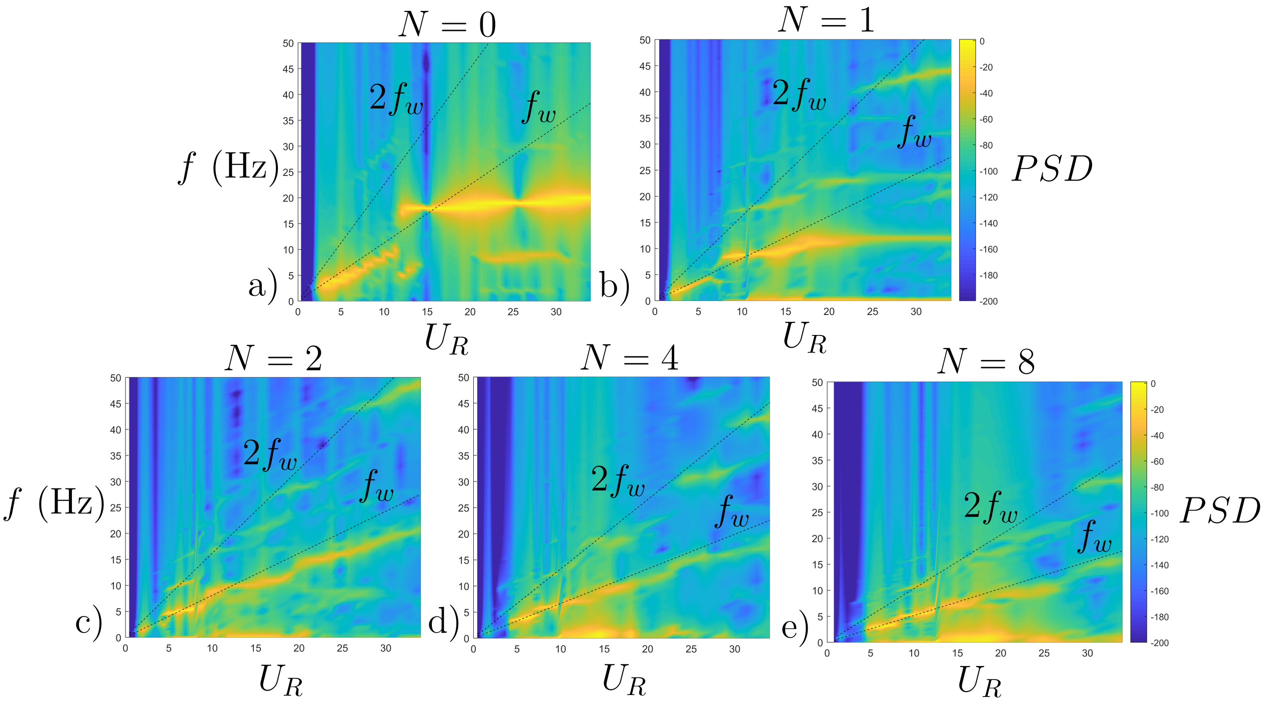

FIGURE 6.12 Tip of the branch cross-flow displacement PSD evolution with U_R for $N = 0, 1, 2, 4, 8$ from the simulations. The vortex shedding frequency and its double are plotted in dotted line $(\cdots)$

excited. Using this hypothesis that a branched structure with many pairs of branches vibrates at the vortex shedding frequency, soft corals can be used as flow meter.

This paradoxical behavior can be explained by the fact that as more branches are added, the structural modes become closer together in frequency. Consequently, the lock-in range on each mode becomes shorter, allowing the closest mode to the vortex shedding frequency to be more strongly excited. As a result, the overall vibration behavior of the structure tends to converge towards the vortex shedding frequency predicted by the Strouhal law.

This observation suggests that branched structures with numerous pairs of branches can be utilized as effective flow meters. By monitoring the vibration frequency of soft corals branches, one can potentially infer the flow velocity. The flow velocity is simply deduced from the measured frequency f at the tip of a branch of diameter D by

$$U = \frac{fD}{S_t}, \tag{6.4}$$

with $S_t \sim 0.2$. This provides a unique and intriguing application for understanding fluid dynamics using natural structures.

To try to explain the common amplitude peak at $U_R \sim 6$ in Fig. 6.11(b,d), we study this region on the spectograms in Fig. 6.12(c,d,e). At this reduced velocity, the vortex shedding frequency for $N = 2, 4, 8$ is at 5 Hz, 4 Hz and 3 Hz, respectively. Reporting these frequencies in the structural modes in Fig. 6.3(a), we find that they correspond to the fourth mode, corresponding to the largest frequency gap for all N.

Guided by the intuition that the high frequency regions in the cross-flow spectograms are correlated to low modal density frequency ranges, we compare the tip of the branch RMS amplitudes and spectrogram for a $N = 8$ structure with its modal frequencies in Fig. 6.13. The first peak in amplitude occurs at U_R in Fig. 6.13(b) which corresponds to a dominant frequency of 3 Hz according to the spectrogram in Fig. 6.13(a). This frequency aligns with the lock-in of the fourth mode, which is characterized by transversely anti-symmetric motion of the two pairs of branches, as shown in Fig. 6.2. This finding may explain why the fourth mode is the dominant mode observed in the experimental data. If structural modes are close in frequency, their lock-in ranges overlap, resulting in no clear resonance as each lock-in is perturbed by neighboring mode lock-ins. However, if a structural mode's frequency is isolated, such as the fourth mode, it has a wider range to develop a lock-in. As demonstrated in (Leclercq & de Langre, 2018), a single-mode lock-in leads to higher vibration amplitudes compared to a multi-frequency response. It is important to note that the modal analysis is conducted on the undeformed structure, and at higher reduced velocities and large reconfi-

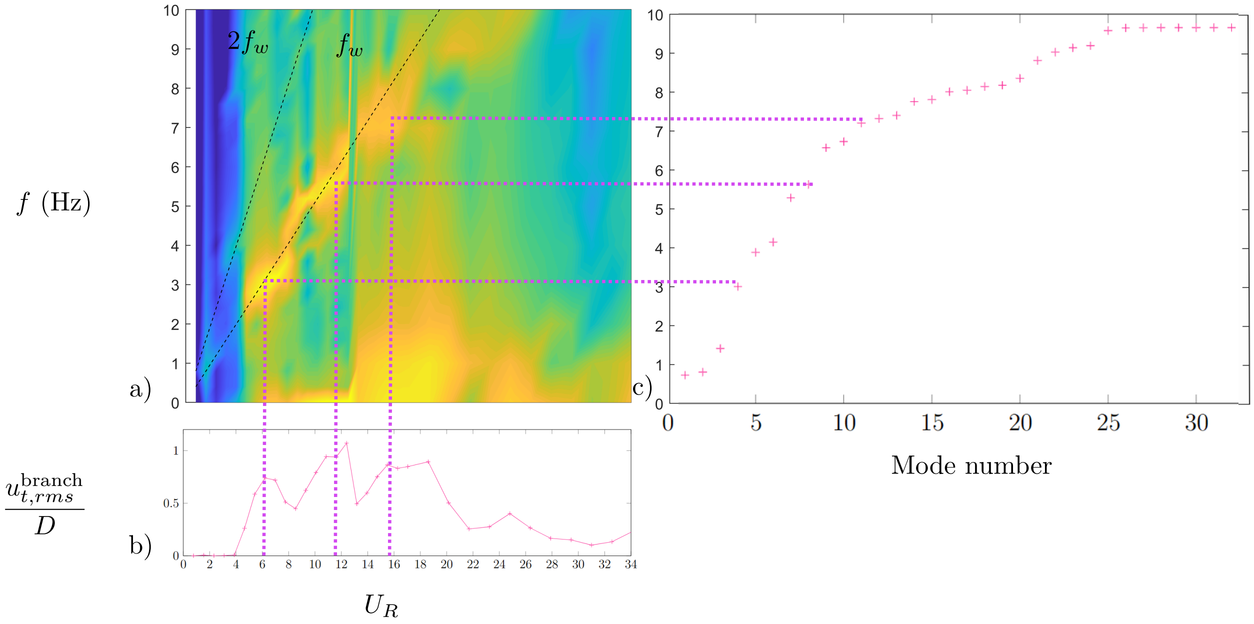

FIGURE 6.13 Tip of the branch cross-flow PSD (a), amplitude (b) and modal frequencies distribution (c) for a $N = 8$ structure. Amplitude peaks are reported vertically on the spectogram and horizontally on the modal frequency plot at the highest PSD region with magenta dotted lines $(\cdots)$

guration, different modes may come into play.

6.4 Interception model for branched structure

This section aims to develop a simple model linking the corals dynamics to a particle interception efficiency. We employ the interception model introduced in (Boudina et al., 2021) for a cross section undergoing VIV on every nodes in the 3D mesh. By performing a spatial integration, we calculate the overall gain in interception of the entire structure at various reduced velocities, thereby gaining valuable insights into the enhanced feeding capabilities of soft corals through VIV.

6.4.1 2D interception model

Let's consider a 2D problem where a cross section is submitted to constant and uniform flow velocity $\mathbf{U} = U\mathbf{e}_x$. The particle interception gain of a vibrating cross section compared to a static one is

$$\delta = \frac{\langle \eta \rangle - \langle \eta_0 \rangle}{\langle \eta_0 \rangle}. \qquad (6.5)$$

with $\langle \eta \rangle$ and $\langle \eta_0 \rangle$ being the interception rate of the vibrating and fixed cross section, respectively, time-average over one period of motion.

Simulation results from Boudina et al. (2021) are used in this analysis: 2D DNS data provide the cross section displacements and velocities for

$$U_R = [1, 2, 3, 3.5, 4, 4.5, 5, 6, 7, 8, 9, 10, 11, 12, 13], \tag{6.6}$$

$$R_e = [50, 100, 150, 200]. \tag{6.7}$$

A particle tracer algorithm computes the passively transported particles trajectory using the DNS solution. Capture is defined as solid contact between a particle and the cylinder. These 2D results serve as calibration data for the model, assuming that the same model can be applied in 3D for each cross section plane. Boudina et al. (2021) find a correlation between the interception gain δ and the counter current distance d_{cc}, which is the distance covered in the opposite of the streamwise direction during the 8-shape trajectory. In order to extend the 2D model to 3D simulations, we investigate a coupling between δ and a kinematic quantity that can be computed in the developed FEM in large deformations. Defining $\mathbf{U}_{pr} = \mathbf{U} - \dot{\mathbf{u}}$ the relative fluid velocity in the cross section plane, we have at time t :

$$U_{pr}(t) = \|\mathbf{U}_{pr}(t)\| = \sqrt{(U - u_2(t))^2 + u_3(t)^2}, \tag{6.8}$$

with u_2, u_3 being the transverse displacements of the cross-section.

We define $\delta_{U_{pr}}$ the gain in relative velocity of a vibrating cylinder with respect to a fixed one, on one period the cross flow displacement T :

$$\delta_{U_{pr}} = \frac{1}{T} \int_0^T \frac{U_{pr}(t) - U}{U} dt, \tag{6.9}$$

with T being the period of the 8-motion. The quantity $\delta_{U_{pr}}$ physically refers to the amount of fluid swept by a vibrating section compared to a fixed one. It is positive if the vibrations enhance the sweeping of the flow, negative otherwise. The interest in this quantity arises from the idea that interception of particles in enhanced with the relative velocity. The interception gain against $\delta_{U_{pr}}$ for particles of diameter $d_p = 0.035D$ are presented in Fig. 6.14.

A linear regression performed on all the data provide the interception law with a correlation coefficient $r^2 = 0.87$:

$$\delta = 2.4\delta_{U_{pr}} - 0.016, \quad r^2 = 0.87. \tag{6.10}$$

By tracking the relative velocity of a cross section at each moment, we make the assumption that the interception gain can be determined using Eq. (6.10).

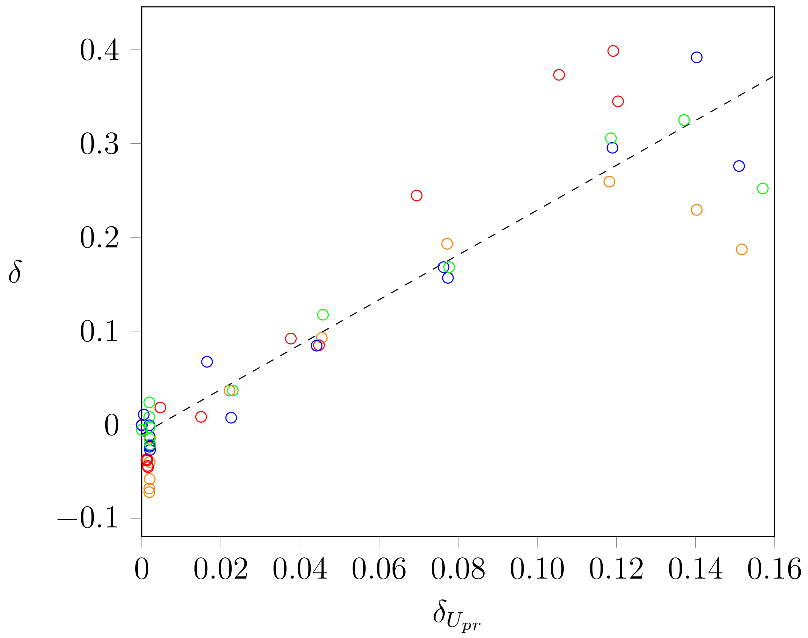

FIGURE 6.14 Interception gain of a 2D circular cross section for $Re = 50$ (○), $Re = 100$ (○), $Re = 150$ (○), $Re = 200$ (○). The dashed line (- - -) is a linear regression ($r^2 = 0.87$): $\delta = a\delta_{U_{pr}} + b$ with $a = 2.39$, $b = -0.02$. Analysis based on data of Boudina et al. (2021)

6.4.2 3D extension of the model

We now consider a cross section of a 3D frame structure at curvilinear coordinate s and time t. We define the interception gain of the entire structure Δ_s computed by integrating Eq. (6.10) on the structural domain Ω, of total length ℓ_Ω :

$$\Delta_s = \frac{1}{\ell_\Omega} \int_{s \in \Omega} \delta(s) \mathrm{ds}, \tag{6.11}$$

with $\theta_0(s, t)$ being the angle of attack of the flow velocity on the cross section plane.

For each reduced velocity, the static solution is first computed. The dynamic problem is then solved using the steady solution as the initial configuration. The numerical integration of the interception gain on one simulation is done by storing in memory two quantities for every time step and nodes (t_i, s_j): the deformed configuration displacements in global coordinates $\mathbf{u}_{ij}$ and the velocity vector of the node in global coordinate $\dot{\mathbf{u}}_{ij}$. The displacements allow to compute the cross section plane perpendicular to the structure at the node Π_{23}, in which the model is applied. The velocities are used to compute the relative velocity vector at each node: $\mathbf{U}_{r,ij} = \mathbf{U} - \mathbf{u}_{ij}$. $\mathbf{U}_{r,ij}$ and $\mathbf{U}$ are then projected on Π_{23}. To achieve this, the projector $\mathbf{P}_{ij}$ is applied at each node in the deformed configuration, which removes the component of the velocity along the tangent vector of the structure :

$$\mathbf{U} \cdot \mathbf{P}_{ij} = \mathbf{U} - (\mathbf{U} \cdot \mathbf{t}_{1,ij})\mathbf{t}_{1,ij}. \tag{6.12}$$

The final interception gain of the structure is numerically integrated on N_t instants and N_s nodes :

$$\Delta_s = \frac{1}{N_s N_t} \sum_{s_j=1}^{N_s} \sum_{t_i=1}^{N_t} 2.4 \frac{U_{pr}(s_j, t_i) \cdot \mathbf{P}_{ij} - U \cdot \mathbf{P}_{ij}}{U \cdot \mathbf{P}_{ij}} - 0.016. \tag{6.13}$$

The discreet 3D gain Δ_s is computed once per complete period of the motion in the second half of the simulation (ignoring the transient), and then averaged. An FFT algorithm computes the 8-shape period as the inverse of the main frequency in the transverse displacement signal.

6.4.3 Biological implications

By considering particle interception as a feeding strategy for passive feeders such as soft corals, we can interpret the parameter Δ_s as the feeding enhancement achieved through VIV. Fig. 6.15 presents the interception gain against U_R for $N = 0, 1, 2, 4, 8$. The interception gain is maximized if a coral does not have branches ($N = 0$) and when a lock-in occurs (41% and 45% at $U_R = 2.9$ and $U_R = 14.9$, respectively). However, if the reduced velocity deviate from these lock-in regions, the capture gain drops dramatically, and becomes one of the lowest among all the considered geometries. The same phenomenon is observed for $N = 1$: a very low interception efficiency is computed for $U_R \in [4 - 6]$. For $N = 2, 4, 8$, the maximum value of the interception efficiency decreases, but the minimal value increases in return, resulting in flattened variations. The advantage of observing a less erratic interception gain for soft corals is that it remains relatively high over a wider range of reduced velocities U_R. This is beneficial because the flow conditions in which soft corals typically reside are often characterized by oscillatory currents rather than steady ones (Bayer, 1961). As a result, the fluctuating nature of U_R allows the coral to potentially benefit from a broader range of interception gain, ensuring a more consistent feeding efficiency in varying flow conditions.

Interestingly, there appears to be a correlation between the interception gain and the cross-flow amplitude of the branches, presented in Fig. 6.11(d). This plot captures all the peaks of amplitudes for all the branched structures ($N > 0$). However, the in-line RMS amplitudes or the trunk tip amplitudes in Fig. 6.11(a,b,c) exhibit a different trend. This finding is consistent with the observation that the cross-flow vibrations are approximately twice as large as the in-line vibrations. The branch tip are more significant indicator of the interception gain compared to the trunk tip, especially as the number of pairs of branches (N) increases. This can be attributed to the fact that the branch tip constitutes a larger proportion of the coral's

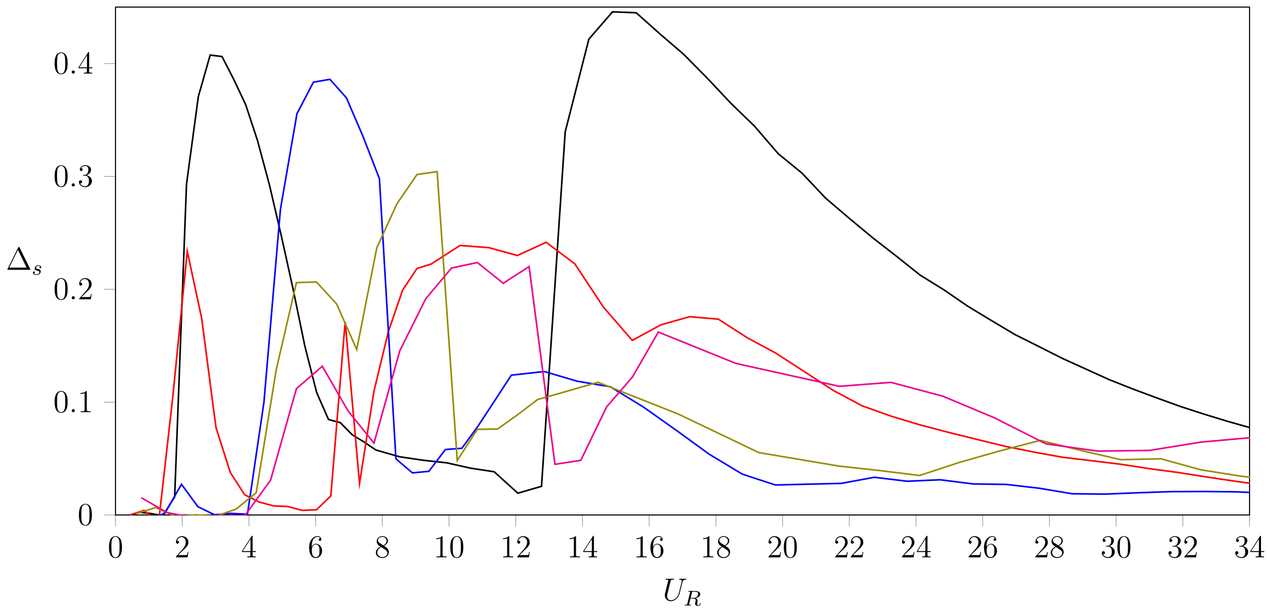

FIGURE 6.15 Interception gain of structures with $N = 0$ (—), $N = 1$ (—), $N = 2$ (—), $N = 4$ (—), $N = 8$ (—) pairs of branches

volume. The discrepancies in peak amplitudes can be attributed to the frequency of oscillations, which plays a role in determining the measured Δ_s value. When comparing vibrations with the same amplitude, higher frequencies correspond to higher reduced velocities experienced by the cross section. For example, the first peak of transverse RMS displacements in Fig. 6.11(d) is higher for $N = 1$ compared to $N = 0$, but its frequency is lower, explaining why the interception gain is lower in Fig. 6.15 for $N = 1$ despite the higher amplitude of vibrations.

Rough estimations from the online video Youtube (2013) shot in the Caribbean Sea provide the observed vibrations frequency $f \sim 8$ Hz, and the flow velocity $U_0 \sim 10$ cm/s. The diameter for soft corals *Antillogorgia bipinnata* is $D = 2$ (Bayer, 1961). This leads to a reduced velocity of

$$U_R = \frac{U_0}{fD} \sim 6. \tag{6.14}$$

It appears that $U_R = 6$ is a meaningful indicator of the conditions encountered by a soft coral in the Caribbean Sea. At this reduced velocity, the $N = 0$ and $N = 1$ geometries show a poor interception gain, of 11% and 0%, respectively. For $N = 2, 4, 8$, the peaks at $U_R \sim 6$ corresponding to a lock-in on the fourth mode, as discussed in Fig. 6.11, are still present in Fig. 6.15. The $N = 2$ model has the highest interception gain of 39%. For $N = 4$ and $N = 8$, the peak at $U_R = 6$ decreases to $\Delta_s = 21\%$ and $\Delta_s = 13\%$, respectively. This makes sense since the fourth mode frequency decreases with N (Fig. 6.2) while the transverse RMS amplitude peak is the same in Fig. 6.11(d). Thus, it seems that it VIV enhances the particle interception for the optimal number of pairs of branches $N = 2$.

CHAPTER 7 CONCLUSION

7.1 Summary of works

In this work, we extended the capabilities of the WOM by developing a new formulation that accounts for coupled in-line and cross-flow VIV in branching structures. We provide a simple yet accurate open-source tool for simulating 3D VIV problems on arbitrarily complex beam structures, including tree-like geometries. To do so, we integrated the WOM and added mass effects into the corotational framework. This constitutes a novelty since previous applications of the WOM are restricted to straight geometries such as pipes or cylinders. Furthermore, the numerical implementation of the proposed formulation has been incorporated into the open-source FEM library ONSAS, making it accessible to the research community. We have submitted a manuscript to the *Journal of Fluids and Structures* (Villié et al., s. d.), presenting the coupling between the 3D-corotational framework and the in-line and cross-flow wake-oscillators.

The present model is verified and validated through a comprehensive analysis involving five examples of a clamped-free flexible cantilever cylinder in a uniform flow. An experimental study of a 3D printed flexible branched structure was carried out and served as a comparison with our model.

Two main insights about the branches impact on the vortex-induced dynamics are found :

- Adding branches increases the number of modes, and as the reduced velocity increases, the vortex shedding frequency excites each mode successively. With a low number of branches, the mode frequencies are spaced, resulting in large jumps in the frequency response. However, as the number of branches increases, the frequency gaps between modes decrease, leading to smaller jumps in the frequency response. The frequency response approaches the vortex shedding frequency of a rigid cylinder, in accordance with the Strouhal law. Interestingly, the addition of complexity to the structure geometry tends to linearize the vibration frequencies.
- The addition of branches introduces additional modes that are distributed unevenly across the frequency spectrum, forming clusters of frequencies. When the modes are close in frequency, they are excited simultaneously, leading to a multi-modal response. In this case, the overlapping lock-in regions of the different modes result in lower vibration amplitudes. However, when regions with a lower density of modes are excited, the interactions between the modes are weaker, allowing for stronger resonance on each individual mode. This leads to higher vibration amplitudes on isolated modes.

A simple model based on the correlation between the interception gain and the relative velocity experienced by the cross section is used to approximately assess the interception gain in the coral FEM. The interception gain shows a consistent trend with the cross-flow RMS amplitudes of the branch tip displacements. However, the addition of branches affects the frequency of the modes, which also impacts the particle interception gain. Specifically, for structures with $2, 4$, and 8 pairs of branches all present a peak of interception gain at $U_R = 6$, but its value decreases to $38.6\%, 20.6\%$, and 13.2%, respectively.

7.2 Limitations

The limitations of this work should be acknowledged. Firstly, the printed geometry used in the study is a simplified representation of a coral and may not fully replicate the intricate vortex-induced dynamics observed in real soft corals. The coarse parametrized model is employed to gain insights into the influence of branches on the VIV behavior, but further research is needed to refine the model and capture the complexities of soft coral dynamics more comprehensively. The model does not consider certain factors such as the larger diameter of the trunk and the significant number of branches found in natural corals. Additionally, the model does not account for the oscillating flow typically experienced by soft corals, which could impact their VIV behavior.

Another limitation of the present model is the lack of consideration for interactions between branches. In scenarios where the structure undergoes significant reconfigurations, upper branches enter the wake of lower upstream branches, the dynamics may be dominated by wake instability rather than VIV. This interaction between branches should be addressed in future studies to provide a more comprehensive understanding of the complex behavior.

Additionally, it is important to note that the model only considers hydrodynamic forces and neglects the tangential component of the flow. This means that effects such as skin friction drag, tangential added mass, flow added damping and flutter mechanisms are not accounted for, particularly when the structure aligns with the flow at high reduced velocities. Therefore, caution is required when interpreting the results obtained at high reduced velocities.

7.3 Future Research

Future research can build upon the findings of this study and explore several avenues for further investigation. Some potential directions for future research include:

1. Extension of the Parametric Study: The parametric study can be expanded by incorporating additional parameters such as the Keulegan-Carpenter number, the aspect

ratio of the branches, and variations in lengths and diameters of the branches and trunk. This would provide a more comprehensive understanding of the effects of these parameters on the vortex-induced dynamics and interception gain.

2. Investigation of Oscillatory Flow: Soft corals are typically found in shallow waters with oscillatory flows, which may have a significant impact on the vortex-induced dynamics and interception gain. It would be interesting to study how the presence of an oscillatory flow influences the behavior of branched structures and their ability to capture particles. This research could provide insights into the adaptations of soft corals to their natural environment.
3. Consideration of Polyps-Induced Roughness: Soft corals have retractable polyps that extend to feed on microscopic organisms. The presence of polyps and their effects on the surface roughness of the coral could potentially influence the vortex-induced vibrations. Future investigations should explore the influence of polyps-induced roughness on the dynamics of branched structures to better understand its impact on vortex-induced vibrations.
4. Fully Coupled FSI Validation: Validating the proposed formulation with a fully coupled FSI study of a branched structure would be valuable. Combining CFD and FEM to simulate the dynamics of a 3D soft coral colony would provide a more comprehensive understanding of the interaction between the structure and the wake, considering the bidirectional coupling between fluid and structural dynamics.
5. Modal Analysis of Branched Structures: Carrying out a modal analysis of branched structures by incorporating a linearized version of the WOM in the forcing terms can provide further insights into the complex interaction between the structure and the wake. This analysis would allow for a detailed examination of the modal properties and the influence of different modes on the overall dynamics of the structure.

Overall, this study opens new avenues for the numerical study of the vortex-induced dynamics of branched structures and tree-like organisms. The implications of this research extend beyond the realm of marine biology. One could think of improving the Bladeless windturbine design by adding branches on the cylinder. This Spanish technology uses a straight cylindrical shape coupled with an alternator to harness the energy from the von Kármán vortex street (Francis et al., 2021). As this study demonstrated that adding one pair of branches can increase the amplitude of vibrations, such a bioinspired bladeless turbine could potentially be more efficient at extracting energy from the flow.

Références

Akagi, Y., & Kitajima, K. (2006). Computer animation of swaying trees based on physical simulation. *Computers & Graphics*, *30*, 529–539.

Augarde, C. E., Lee, S. J., & Loukidis, D. (2021). Numerical modelling of large deformation problems in geotechnical engineering : A state-of-the-art review. *Soils and Foundations*, *61*(6), 1718–1735.

Bathe, K.-J. (2006). *Finite element procedures.* Klaus-Jurgen Bathe.

Battini, J.-M., & Pacoste, C. (2002). Co-rotational beam elements with warping effects in instability problems. *Computer Methods in Applied Mechanics and Engineering*, *191*(17-18), 1755–1789.

Bayer, F. M. (1961). The shallow-water Octocorallia of the West Indian region. *Studies on the Fauna of Curaçao and other Caribbean Islands*, *12*(1), 1–373.

Beem, H. R., & Triantafyllou, M. S. (2015). Wake-induced 'slaloming'response explains exquisite sensitivity of seal whisker-like sensors. *Journal of Fluid Mechanics*, *783*, 306–322.

Bernitsas, M. M., Raghavan, K., Ben-Simon, Y., & Garcia, E. M. (2008, septembre). VIVACE (Vortex Induced Vibration Aquatic Clean Energy) : A New Concept in Generation of Clean and Renewable Energy From Fluid Flow. *Journal of Offshore Mechanics and Arctic Engineering*, *130*(4), 041101–041101.

Bishop, R. E. D., & Hassan, A. Y. (1964, janvier). The lift and drag forces on a circular cylinder oscillating in a flowing fluid. *Proc. R. Soc. Lond. A*, *277*(1368), 51–75.

Blevins. (1977). Flow-induced vibration. *New York.*

Blevins. (1990). *Flow-induced vibration.* Van Nostrand Reinhold.

Blevins, R. D. (2015). *Formulas for dynamics, acoustics and vibration.* John Wiley & Sons.

Blevins, R. D., & Coughran, C. S. (2009, septembre). Experimental Investigation of Vortex-Induced Vibration in One and Two Dimensions With Variable Mass, Damping, and Reynolds Number. *Journal of Fluids Engineering*, *131*(10), 101202–101202–7.

Boschma, H. (1925). On the feeding reactions and digestion in the coral polyp astrangia danae, with notes on its symbiosis with zooxanthellae. *The Biological Bulletin*, *49*(6), 407–439.

Boudina, M. (2020). *On the mechanics of flow-induced vibration of soft corals and particle interception* (Thèse de doctorat non publiée). Ecole Polytechnique, Montreal (Canada).

Boudina, M., Gosselin, F. P., & Étienne, S. (2021). Vortex-induced vibrations : a soft coral feeding strategy ? *Journal of Fluid Mechanics*, *916*, A50.

Bourne, D., & Webster, N. (2013). Coral reef bacterial communities. *The Prokaryotes–*

Prokaryotic communities and ecophysiology, *4*, 163–187.

Chaplin, J. R., Bearman, P. W., Huera Huarte, F. J., & Pattenden, R. J. (2005, novembre). Laboratory measurements of vortex-induced vibrations of a vertical tension riser in a stepped current. *Journal of Fluids and Structures*, *21*(1), 3–24.

Chapuliot, S., Moulin, D., & Plancq, D. (2002). Mechanical behavior of a branch pipe subjected to out-of-plane bending load. *J. Pressure Vessel Technol.*, *124*(1), 7–13.

Cheng, N.-S. (2013). Calculation of drag coefficient for arrays of emergent circular cylinders with pseudofluid model. *Journal of Hydraulic Engineering*, *139*(6), 602–611.

Chizfahm, A., & Jaiman, R. (2021). Data-driven stability analysis and near-wake jet control for the vortex-induced vibration of a sphere. *Physics of Fluids*, *33*(4), 044104.

Cho, H., Gong, D., Lee, N., Shin, S., & Lee, S. (2019). Combined co-rotational beam/shell elements for fluid–structure interaction analysis of insect-like flapping wing. *Nonlinear Dynamics*, *97*, 203–224.

Coelho, M. A. (2018). *Life history traits of caribbean octocorals of the genus antillogorgia and their implications for larval dispersal* (Thèse de doctorat non publiée). State University of New York at Buffalo.

Crisfield, M., Galvanetto, U., & Jelenić, G. (1997). Dynamics of 3-d co-rotational beams. *Computational Mechanics*, *20*(6), 507–519.

Daly, M., Brugler, M. R., Cartwright, P., Collins, A. G., Dawson, M. N., Fautin, D. G., ... others (2007). The phylum cnidaria : a review of phylogenetic patterns and diversity 300 years after linnaeus.

de Langre, E. (2001). *Fluides et solides.* Editions Ecole Polytechnique. (Google-Books-ID : IFnLwQ4eTIwC)

De Langre, E. (2008). Effects of wind on plants. *Annu. Rev. Fluid Mech.*, *40*, 141–168.

De Langre, E. (2012). Methodological advances in predicting flow-induced dynamics of plants using mechanical-engineering theory. *Journal of Experimental Biology*, *215*(6), 914–921.

Der Loughian, C., Tadrist, L., Allain, J.-M., Diener, J., Moulia, B., & de Langre, E. (2014, janvier). Measuring local and global vibration modes in model plants. *Comptes Rendus Mécanique*, *342*(1), 1–7.

Dhar, L. (2020). Étude de l'injection d'air à travers des fentes dans un écoulement d'eau transverse. *ProQuest Dissertations and Theses*, 103. (Copyright - Database copyright ProQuest LLC ; ProQuest does not claim copyright in the individual underlying works ; Dernière mise à jour - 2023-03-08)

Elkaranshawy, H. A., Elerian, A. A., & Hussien, W. I. (2018). A corotational formulation based on hamilton's principle for geometrically nonlinear thin and thick planar beams and frames. *Mathematical Problems in Engineering*, *2018*.

Etienne, S., & Pelletier, D. (2012, mai). The low Reynolds number limit of vortex-induced vibrations. *Journal of Fluids and Structures*, *31*, 18–29.

Evangelinos, C., & Karniadakis, G. E. (1999a). Dynamics and flow structures in the turbulent wake of rigid and flexible cylinders subject to vortex-induced vibrations. *Journal of fluid mechanics*, *400*, 91–124.

Evangelinos, C., & Karniadakis, G. E. (1999b, décembre). Dynamics and flow structures in the turbulent wake of rigid and flexible cylinders subject to vortex-induced vibrations. *Journal of Fluid Mechanics*, *400*, 91–124. (Publisher : Cambridge University Press)

Fabricius, K., & Hopley, D. (2011). *Octocorallia. encyclopedia of modern coral reefs. encyclopedia of earth sciences series.* Netherlands : Springer.

Facchinetti, M., de Langre, E., & Biolley, F. (2004a, feb). Coupling of structure and wake oscillators in vortex-induced vibrations. *Journal of Fluids and Structures*, *19*(2), 123–140.

Facchinetti, M., de Langre, E., & Biolley, F. (2004b, janvier). Vortex-induced travelling waves along a cable. *European Journal of Mechanics - B/Fluids*, *23*(1), 199–208.

Feng, Y., Chen, D., Li, S., Xiao, Q., & Li, W. (2022). Vortex-induced vibrations of flexible cylinders predicted by wake oscillator model with random components of mean drag coefficient and lift coefficient. *Ocean Engineering*, *251*, 110960.

Fernandes, M. C., Saadat, M., Cauchy-Dubois, P., Inamura, C., Sirota, T., Milliron, G., … Weaver, J. C. (2021, septembre). Mechanical and hydrodynamic analyses of helical strake-like ridges in a glass sponge. *Journal of The Royal Society Interface*, *18*(182), 20210559.

Francis, S., Umesh, V., & Shivakumar, S. (2021). Design and analysis of vortex bladeless wind turbine. *Materials Today : Proceedings*, *47*, 5584–5588.

Gao, Y., Fu, S., Ren, T., Xiong, Y., & Song, L. (2015). Viv response of a long flexible riser fitted with strakes in uniform and linearly sheared currents. *Applied Ocean Research*, *52*, 102–114.

Gao, Y., Zhang, Z., Pan, G., Peng, G., Liu, L., & Wang, W. (2021). Three-dimensional vortex-induced vibrations of a circular cylinder predicted using a wake oscillator model. *Marine Structures*, *80*, 103078.

Gao, Y., Zou, L., Zong, Z., Takagi, S., & Kang, Y. (2019). Numerical prediction of vortex-induced vibrations of a long flexible cylinder in uniform and linear shear flows using a wake oscillator model. *Ocean Engineering*, *171*, 157–171.

Ge, F., Long, X., Wang, L., & Hong, Y. (2009). Flow-induced vibrations of long circular cylinders modeled by coupled nonlinear oscillators. *Science in China Series G : Physics,* *Mechanics and Astronomy*, *52*(7), 1086–1093.

Gosselin, F. P. (2019). Mechanics of a plant in fluid flow. *Journal of Experimental Botany*, *70*(14), 3533–3548.

Gosselin, F. P., de Langre, E., & Machado-Almeida, B. A. (2010, mai). Drag reduction of flexible plates by reconfiguration. *Journal of Fluid Mechanics*, *650*, 319.

Habel, R., Kusternig, A., & Wimmer, M. (2009). Physically guided animation of trees. In *Computer graphics forum* (Vol. 28, pp. 523–532).

Hanke, W., Witte, M., Miersch, L., Brede, M., Oeffner, J., Michael, M., … Dehnhardt, G. (2010, juillet). Harbor seal vibrissa morphology suppresses vortex-induced vibrations. *Journal of Experimental Biology*, *213*(15), 2665–2672.

Hoegh-Guldberg, O., Mumby, P. J., Hooten, A. J., Steneck, R. S., Greenfield, P., Gomez, E., … others (2007). Coral reefs under rapid climate change and ocean acidification. *science*, *318*(5857), 1737–1742.

Holmes, S., Oakley Jr, O. H., & Constantinides, Y. (2006). Simulation of riser viv using fully three dimensional cfd simulations. *International Conference on Offshore Mechanics and Arctic Engineering*, *47497*, 563–570.

Hu, X.-y., Tao, W.-m., & Guo, Y.-m. (2008). Using fem to predict tree motion in a wind field. *Journal of Zhejiang University-Science A*, *9*, 907–915.

Jain, A., & Modarres-Sadeghi, Y. (2013). Vortex-induced vibrations of a flexibly-mounted inclined cylinder. *Journal of Fluids and Structures*, *43*, 28–40.

Kang, Z., & Jia, L. (2013). An experiment study of a cylinder's two degree of freedom viv trajectories. *Ocean Engineering*, *70*, 129–140.

Khalak, A., & Williamson, C. H. K. (1999, octobre). Motions, forces and mode transitions in vortex-induced vibrations at low mass-damping. *Journal of Fluids and Structures*, *13*(7), 813–851.

Knowlton, N., Brainard, R. E., Fisher, R., Moews, M., Plaisance, L., & Caley, M. J. (2010). Coral reef biodiversity. *Life in the world's oceans : diversity distribution and abundance*, 65–74.

Law, Y. Z., & Jaiman, R. K. (2017). Wake stabilization mechanism of low-drag suppression devices for vortex-induced vibration. *Journal of Fluids and Structures*, *70*, 428–449.

Le, T.-N., Battini, J.-M., & Hjiaj, M. (2011). Efficient formulation for dynamics of corotational 2d beams. *Computational Mechanics*, *48*, 153–161.

Le, T.-N., Battini, J.-M., & Hjiaj, M. (2014, feb). A consistent 3D corotational beam element for nonlinear dynamic analysis of flexible structures. *Computer Methods in Applied Mechanics and Engineering*, *269*, 538–565.

Leclercq, T., & de Langre, E. (2018, jul). Vortex-induced vibrations of cylinders bent by the flow. *Journal of Fluids and Structures*, *80*, 77–93.

Lei, J., & Nepf, H. (2019). Wave damping by flexible vegetation : Connecting individual blade dynamics to the meadow scale. *Coastal Engineering*, *147*, 138–148.

Li, X., Wei, W., & Bai, F. (2020). A full three-dimensional vortex-induced vibration prediction model for top-tensioned risers based on vector form intrinsic finite element method. *Ocean Engineering*, *218*, 108140.

Ltd., O. (2007). Orcaflex user manual [Manuel de logiciel].

Lucor, D., Mukundan, H., & Triantafyllou, M. S. (2006, août). Riser modal identification in CFD and full-scale experiments. *Journal of Fluids and Structures*, *22*(6), 905–917.

Lyons, K., Murphy, C. T., & Franck, J. A. (2020). Flow over seal whiskers : Importance of geometric features for force and frequency response. *Plos one*, *15*(10), e0241142.

Malul, D., Holzman, R., & Shavit, U. (2020, juin). Coral tentacle elasticity promotes an out-of-phase motion that improves mass transfer. *Proceedings of the Royal Society B : Biological Sciences*, *287*(1929), 20200180. (Publisher : Royal Society)

McCombe, D., & Ackerman, J. D. (2018, juillet). Collector Motion Affects Particle Capture in Physical Models and in Wind Pollination. *The American Naturalist*, *192*(1), 81–93. Consulté le 2018-10-16, sur `https://www.journals.uchicago.edu/doi/10.1086/697551` doi: 10.1086/697551

Menter, F., Sharkey, P., Yakubov, S., & Kuntz, M. (2006). Overview of fluid-structure coupling in ansys-cfx. In *International conference on offshore mechanics and arctic engineering* (Vol. 47497, pp. 579–585).

Modarres-Sadeghi, Y. (2022). Vortex-induced vibrations of flexible beams. In *Introduction to fluid-structure interactions* (pp. 211–225). Springer.

Moynihan, M. A., Amini, S., Goodkin, N. F., Tanzil, J. T., Chua, J. I., Fabbro, G. N., ... Miserez, A. (2021). Environmental impact on the mechanical properties of porites spp. corals. *Coral Reefs*, *40*(3), 701–717.

Mukundan, H., Modarres-Sadeghi, Y., Dahl, J. M., Hover, F. S., & Triantafyllou, M. S. (2009, mai). Monitoring VIV fatigue damage on marine risers. *Journal of Fluids and Structures*, *25*(4), 617–628.

Naudascher, E. (2017). *Flow-induced vibrations : an engineering guide.* Routledge.

Newman, D. J., & Karniadakis, G. (1997). A direct numerical simulation study of flow past a freely vibrating cable. *Journal of Fluid Mechanics*, *344*, 95–136.

Ogink, R., & Metrikine, A. (2010). A wake oscillator with frequency dependent coupling for the modeling of vortex-induced vibration. *Journal of sound and vibration*, *329*(26), 5452–5473.

Oñate, E. (2013). *Structural analysis with the finite element method. linear statics : volume*

2 : beams, plates and shells. Springer Science & Business Media.

Paidoussis, M. P. (1998). *Fluid-structure interactions : slender structures and axial flow* (Vol. 1). Academic press.

Païdoussis, M., Price, S., & de Langre, E. (2010). *Fluid-Structure Interactions : Cross-Flow-Induced Instabilities.* Cambridge University Press.

Pérez Zerpa, J. M., Vanzulli Pena, M. C., Villié, A., Bazzano García, J. B., Viera Sosa, J., Forets, M., & Battini, J.-M. (2022). *Onsas.m : an open nonlinear structural analysis solver for gnu-octave/matlab.* Consulté sur `https://github.com/ONSAS/ONSAS.m`

Qu, Y., & Metrikine, A. V. (2020). A single van der pol wake oscillator model for coupled cross-flow and in-line vortex-induced vibrations. *Ocean Engineering*, *196*, 106732.

Quigley, E., Yu, Y., Huang, J., Lin, W., & Fedkiw, R. (2017). Real-time interactive tree animation. *IEEE transactions on visualization and computer graphics*, *24*(5), 1717–1727.

Ribes, M., Coma, R., & Gili, J.-M. (1998, septembre). Heterotrophic feeding by gorgonian corals with symbiotic zooxanthella. *Limnology and Oceanography*, *43*(6), 1170–1179. (Publisher : John Wiley & Sons, Ltd)

Rodriguez, M., Langre, E. d., & Moulia, B. (2008, décembre). A scaling law for the effects of architecture and allometry on tree vibration modes suggests a biological tuning to modal compartmentalization. *American Journal of Botany*, *95*(12), 1523–1537.

Rodriguez, M., Ploquin, S., Moulia, B., & de Langre, E. (2012). The multimodal dynamics of a walnut tree : experiments and models. *Journal of Applied Mechanics*, *79*(4), 044505.

Rukavishnikov, V. A., Ryabokon, A. S., & Tkachenko, O. P. (2023). Numerical investigation of pipe deformation under pressure with branch. *International Journal of Applied Mechanics*, 2350052.

Sarpkaya, T. (1976). *Vortex shedding and resistance in harmonic flow about smooth and rough circular cylinders at high reynolds numbers* (Rapport technique). Naval Postgraduate School Monterey CA.

Sehat, H., Abdolahpour, M., Jamali, M., & Ghisalberti, M. (2023). The impact of plant oscillation on dispersion in emergent aquatic canopies. *Water Resources Research*, e2022WR032035.

Shafir, S., van Rijn, J., & Rinkevich, B. (2016). Coral farming as a tool for reef restoration and livelihood improvement in tanzania. *Marine Policy*, *63*, 126–133.

Shinya, M., & Fournier, A. (1992). Stochastic motion—motion under the influence of wind. In *Computer graphics forum* (Vol. 11, pp. 119–128).

Skop, R. A., & Balasubramanian, S. (1997). A new twist on an old model for vortex-excited vibrations. *Journal of Fluids and Structures*, *11*(4), 395–412.

Spencer, T. L., Mohebbi, N., Jin, G., Forister, M. L., Alexeev, A., & Hu, D. L. (2019). Moth-inspired methods for particle capture on a cylinder. *Journal of Fluid Mechanics*, *884*. (Publisher : Cambridge University Press)

Srinil, N., & Zanganeh, H. (2012, oct). Modelling of coupled cross-flow/in-line vortex-induced vibrations using double Duffing and van der Pol oscillators. *Ocean Engineering*, *53*, 83–97.

Sukhodolov, A., Sukhodolova, T., & Aberle, J. (2022). Modelling of flexible aquatic plants from silicone syntactic foams. *Journal of Hydraulic Research*, *60*(1), 173–181.

Sumer, B. M., et al. (2006). *Hydrodynamics around cylindrical strucures* (Vol. 26). World scientific.

Tian, F.-B., Dai, H., Luo, H., Doyle, J. F., & Rousseau, B. (2014). Fluid–structure interaction involving large deformations : 3d simulations and applications to biological systems. *Journal of computational physics*, *258*, 451–469.

Trim, A., Braaten, H., Lie, H., & Tognarelli, M. (2005). Experimental investigation of vortex-induced vibration of long marine risers. *Journal of fluids and structures*, *21*(3), 335–361.

Vandiver, J. K. (1993). Dimensionless parameters important to the prediction of vortex-induced vibration of long, flexible cylinders in ocean currents. *Journal of Fluids and Structures*, *7*(5), 423–455.

Vanzulli, M. C., & Zerpa, J. M. P. (2022). A consistent co-rotational formulation for aerodynamic nonlinear analysis of flexible frame structures. *arXiv preprint arXiv :2204.10545*.

Vedeld, K., Sollund, H. v., & Fyrileiv, O. (2011). Fatigue and environmental loading of large-bore manifold piping. In *International conference on offshore mechanics and arctic engineering* (Vol. 44335, pp. 313–321).

Villié, A., Gosselin, F., Zerpa, J. P., Pena, M. V., Etienne, S., & Vétel, J. (s. d.). Modelling vortex-induced vibrations of branched structures by coupling a 3d-corotational frame finite element formulation with wake-oscillators.

Violette, R., de Langre, E., & Szydlowski, J. (2007, juin). Computation of vortex-induced vibrations of long structures using a wake oscillator model : Comparison with DNS and experiments. *Computers & Structures*, *85*(11), 1134–1141.

Wagner, J. (2014, Oct.). *Visualisation of the von kàrmàn vortex sheet behind a circular cylinder in air flow.* Consulté sur `https://commons.wikimedia.org/wiki/File:Karmansche_Wirbelstr_kleine_Re.JPG`

Wang, J., Fu, S., Baarholm, R., Wu, J., & Larsen, C. M. (2015). Fatigue damage induced by vortex-induced vibrations in oscillatory flow. *Marine Structures*, *40*, 73–91.

Wang, L., Jiang, T., Dai, H., & Ni, Q. (2018). Three-dimensional vortex-induced vibrations of supported pipes conveying fluid based on wake oscillator models. *Journal of Sound and Vibration*, *422*, 590–612.

Willden, & Graham. (2001). Numerical prediction of viv on long flexible circular cylinders. *Journal of Fluids and Structures*, *15*(3-4), 659–669.

Willden, & Graham. (2004). Multi-modal vortex-induced vibrations of a vertical riser pipe subject to a uniform current profile. *European Journal of Mechanics-B/Fluids*, *23*(1), 209–218.

Williamson, C. H. K. (1996, décembre). Three-dimensional wake transition. *Journal of Fluid Mechanics*, *328*, 345–407.

Xia, Y., Michelin, S., & Doaré, O. (2015). Fluid-solid-electric lock-in of energy-harvesting piezoelectric flags. *Physical review applied*, *3*(1), 014009.

Youtube. (2013). *Caribbean Spiny Lobster and a Bipinnate Sea Plume coral.* Consulté sur `https://youtu.be/1mgAyFgYfYw`

APPENDIX A BENDING TEST

In order to measure the bending stiffness EI, we conduct a 3-point bending test using an MTS Insight machine, with a length of $L = 12D$ mm between the two fixed points. A picture of the test is presented in Fig. A.1. The test specimen is a cylinder with a length of $\ell = 150$ mm and a diameter of $D = 5$ mm. Due to the high flexibility of the material, a load cell with a maximum capacity of 100 N and a sensitivity of 1.94 mV/V is used to measure the applied load. Three tests are performed, each at a different load speed: $5, 10$ and 20 mm/min. The tests are stopped once the deflection reaches 6 mm.

The deflection δ is :

$$\delta = \frac{FL^3}{48EI}, \tag{A.1}$$

with F being the applied force. It follows

$$EI = \frac{FL^3}{48\delta}. \tag{A.2}$$

Fig. A.2 plots the applied force against the deflection δ for the three tests. Only straight lines are observed, indicating that the deformation remained within the elastic domain. To quantify the relationship, we perform a linear regression on each dataset to determine the slopes of the lines, denoted as α:

$$\alpha = \frac{48EI}{L^3}, \tag{A.3}$$

and deduce the average bending stiffness computed from the average of the three slopes α_{avg} :

$$EI = \frac{L^3}{48}\alpha_{avg} \tag{A.4}$$

$$EI = 4.2 \text{ N mm}^2. \tag{A.5}$$

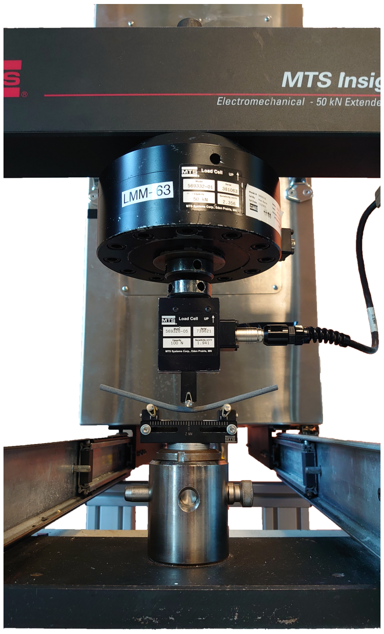

Figure A.1 3-points bending test on the printed cylinder

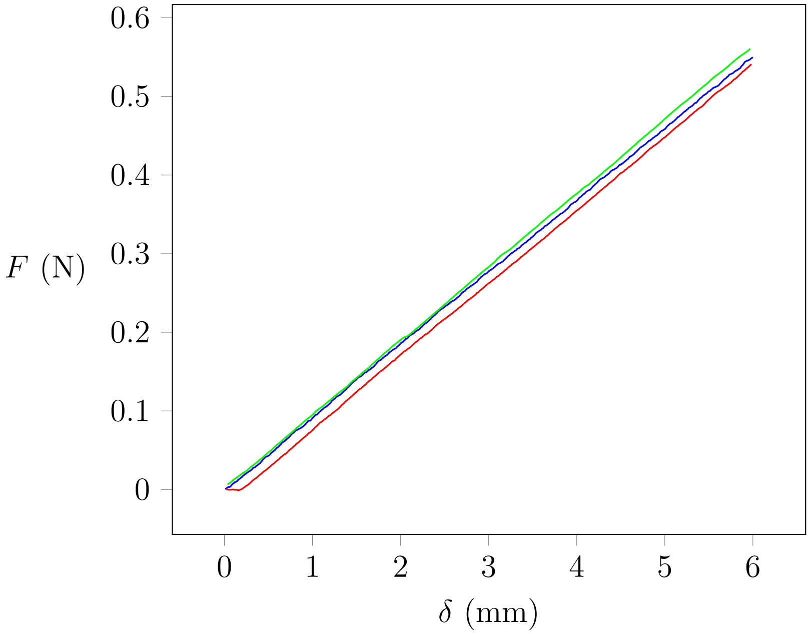

Figure A.2 3-points bending tests for loading speeds of 5 mm/min (—), 10 mm/min (—), 20 mm/min (—)

APPENDIX B LINEAR MODAL ANALYSIS

This section develops the classical equations of the linear modal analysis. Dissipative terms are neglected in this formulation since they are not essential for frequency analysis purposes. The analysis is performed on the initial configuration, where the triad $(\mathbf{e}_\mathrm{x}, \mathbf{e}_\mathrm{y}, \mathbf{e}_\mathrm{z})$ is the global frame. The studied geometries are the coral models with $N = 0, 1, 2, 3, 4, 8$ pairs of branches. The planar structure is defined in the yz-plane. We consider a frame element with 12 degrees of freedom (3 rotations and 3 translations at both nodes) encapsulated in the element displacements vector :

$$\mathbf{d}^e(t) = [u_x^{e,1}\theta_x^{e,1}u_y^{e,1}\theta_y^{e,1}u_z^{e,1}\theta_z^{e,1}u_x^{e,2}\theta_x^{e,2}u_y^{e,2}\theta_y^{e,2}u_z^{e,2}\theta_z^{e,2}]. \tag{B.1}$$

The modal decomposition assumes that the shape of the coral can be represented as a combination of eigenmodes or eigenfunctions at any instant in time. The assembled displacement vector of the structure $\mathbf{d}_s$ can be expressed as

$$\mathbf{d}_s(t) = \sum_i w_i(t)\Phi_i, \tag{B.2}$$

with $w_i(t)$ being the modal weights and Φ_i the eigenmodes. The system has a consistent mass matrix $\mathbf{M}_s$, no damping and a stiffness matrix $\mathbf{K}_s$. The free oscillations of the system are computed with no forcing term:

$$\mathbf{M}_s\ddot{\mathbf{d}}_s + \mathbf{K}_s\mathbf{d}_s = \mathbf{0}. \tag{B.3}$$

As the first node is the clamped one with Dirichlet boundary conditions, the six first degrees of freedom (dof) are removed from the system. For a mesh with N_n nodes the system is:

$$\mathbf{M}_{s,6(N_n-1)}\ddot{\mathbf{d}}_s + \mathbf{K}_{s,6(N_n-1)}\mathbf{d}_s = \mathbf{0}, \tag{B.4}$$

where the subscripts denote the size of the square matrix. Lets assume a harmonic solution form for the displacements, where $\mathbf{x} = \mathbf{x}^0 e^{i\omega t}$. We use the Matlab function `eig` to solve the eigenvalue problem. The goal is to find the eigenvalues (ω) and eigenvectors (Φ) satisfying the equation

$$\omega^2\mathbf{M}_s\Phi = \mathbf{K}_s\Phi. \tag{B.5}$$

The eigenvectors (Φ) represent the mode shapes, which describe the spatial distribution of displacements for each mode, and the eigenvalues (ω) are the modes angular frequencies.

The shape of the mode i visualized using a 3D plot, where each node is represented by adding its initial position to the displacements determined by the eigenvectors, scaled by time coefficients, over a quarter of the mode period :

$$\begin{bmatrix} u_1 \\ u_2 \\ u_3 \end{bmatrix} + \begin{bmatrix} \Phi_i(1) \\ \Phi_i(3) \\ \Phi_i(5) \end{bmatrix} \sin(\omega_i t), \quad t \in \left[0, \frac{2\pi}{4\omega_i}\right], \tag{B.6}$$

with Φ_i, ω_i being the shape vector and angular frequency of mode i. We use varying shades of gray in the visualization to create a sense of motion.

The scope of the modal analysis is limited to the lowest modes, since it is computed in the initial configuration. We expect these low frequency modes to be excited by the wake for low fluid velocities U, as the wake frequency $f_w^0 = S_T U/D$ is proportional to U, when the structural reconfiguration is minimal. However, higher frequencies are excited at high fluid velocities, when the structure bends under the flow with large displacements. In such cases, the linear modal analysis becomes less relevant.